AN ABSTRACT OF THE DISSERTATION OF

Akash Kannegulla for the degree of Doctor of Philosophy in Electrical and Computer Engineering presented on August 30, 2018.

Title: Quantum Dot Plasmon Coupling: Fundamental Study and Applications

Abstract approved:

_____

Li-Jing (Larry) Cheng

The dissertation focuses on the engineering of light-matter interaction using plasmonic nanoparticles and metamaterials to achieve enhanced luminescence and based on which to improve the performance of biosensing and light-emitting technologies. We designed and fabricated a spectrum of nanostructures to exhibit particular dispersion relations capable of controlling the spontaneous emission properties of quantum emitters, such as quantum dots and organic fluorophores. To realize the concept, we developed a metal-assisted focused-ion beam nanopatterning technology to fabricate the plasmonic nanostructures with high-definition. We demonstrated a silver open-ring nanoarrays (ORA) for broadband enhancement of QD emission that was further exploited to demonstrate ultrasensitive DNA sensing. The ORA design offers multiple resonance peaks to support both Purcell effect and excitation enhancement, resulting in a maximal enhancement in QD emission of greater than 100 times and significant improvement in the limit-of-detection of DNA sensing by four orders of magnitude. Another plasmonic nanostructure, aluminum dimple array, was developed to take

advantage of the inherent UV plasmonic property of aluminum for broadband enhancement of QD emission. The device may find major applications in optoelectronic devices. While the small-area plasmonic devices are suitable to enhance the fluorescence-based sensors on a chip, there exists a need for large-area enhancement for several applications. For this purpose, we developed multilayered hyperbolic metamaterials accompanied with an efficient light-extraction approach to achieve enhanced quantum dot emission over a large area. Lastly, we expanded the enhancement strategy using plasmonic nanoparticles to improve carbon dot-based microLEDs. The embedded plasmonic nanoparticles were utilized to enhance carbon dot emission while minimizing the UV excitation leak–age. This research provides a set of design rules for enhanced spontaneous emission and the demonstrated applications are expected to pave the way to advanced photonic, biosensing, and optoelectronic devices.

Quantum Dot Plasmon Coupling: Fundamental Study and Applications

by
Akash Kannegulla

A DISSERTATION

submitted to

Oregon State University

in partial fulfillment of
the requirements for the
degree of

Doctor of Philosophy

Presented August 30, 2018
Commencement June 2019

Doctor of Philosophy dissertation of Akash Kannegulla presented on August 30, 2018

APPROVED:

Major Professor, representing Electrical and Computer Engineering

Director of the School of Electrical Engineering and Computer Science

Dean of the Graduate School

I understand that my dissertation will become part of the permanent collection of Oregon State University libraries. My signature below authorizes release of my dissertation to any reader upon request.

Akash Kannegulla, Author

ACKNOWLEDGEMENTS

I would like to express my appreciation to my advisor Professor Li-Jing (Larry) Cheng for the guidance and advising through my graduate education. It was only because of his keen interest and careful supervision that gave my work this extent form. My appreciation also extends to Professor Alan X. Wang, Professor Chih-Hung Chang, Professor Matthew Johnston, Professor John Labram and Professor Jimmy Yang for serving as my committee members.

I also would like to thank all my current and former laboratory colleagues (Ye Liu, Bo Wu, Yi-Chieh Wang, Vishvas Chalishazar, and Amritha Ajithkumar), collaborators (Professor Oksana Ostroverkhova and Jonathan Van Schenck), Murgesh Padmanarayan, and Sivashanmugan Kundan for their academic support and friendship.

I want to specially acknowledge with gratitude, the support and love of my family. The completion of my Ph.D. study would not have been possible without them.

Finally, I want to thank for the financial support from National Science Foundation under Grant No. 1512816 and National Institutes of Health (no. 1R21DE027170-01).

TABLE OF CONTENTS

Page

1 Introduction..…… 1

1.1 Surface plasmon resonance ….……..3

1.2 Metal enhanced fluorescence...……..……6

1.3 Applications and methods of fluorescence enhancement.……..….....10

1.3.1 Protein sensing…….……10

1.3.2 DNA sensing.…….14

1.3.3 Hyperbolic metamaterials…….16

1.3.4 Display technology……..…….21

1.4 Thesis organization…….…….24

2 Metal assisted focused-ion beam nanopatterning…...……26

2.1 Introduction….……26

2.2 Methods……... ……...29

2.3 Results and discussions …….……...…..30

2.3.1 Dual line patterns..……..…….30

2.3.2 Templates for nanoimprint lithography……...…….33

2.3.3 Two-dimensional plasmonic arrays…….....…….38

2.3.4 QD enhancement on gold dimple arrays……..…….40

3.4 Summary…….....…..42

3 Plasmonic open-ring nanoarrays for broadband enhancement and DNA detection……...43

3.1 Introduction……...……..43

3.2 Materials and methods ……..….46

TABLE OF CONTENTS (Continued)

3.2.1 Fabrication of silver open-ring and dimple nanoarrays……46

3.2.2 Characterization of QD emission enhancement……47

3.2.3 Finite difference time-domain (FDTD) simulations…..……48

3.2.4 Fabrication of microfluidic cells……...……50

3.2.5 DNA detection assay……..……...……51

3.3 Results and discussions ……....52

3.4 Summary……...……..64

4 Aluminum ultraviolet-visible plasmonic arrays for broadband and wavelength selective enhancements of QD emission…….……..65

4.1 Introduction……65

4.2 Results and discussions .……66

4.3 Summary ……..……75

5 Hyperbolic metamaterials for QD enhancement: effect of unit cell thickness and large area outcoupling ……...76

5.1 Introduction……76

5.2 Theory……77

5.3 Results and discussion...……79

5.4 Summary……89

6 Carbon dot-plasmon coupling for microLED display enhancement and control of UV excitation leakage……...90

6.1 Introduction……90

6.2 Experimental section..……91

6.2.1 Synthesis of carbon dots(CDs)……..……...……91

TABLE OF CONTENTS (Continued)

6.2.2 Synthesis of Ag nanoparticles..……..……...…….92

6.2.3 Fabrication of microLED…....……..……...…….93

6.3 Results and discussion...…….93

6.4 Summary…….98

7 Conclusions……..…...……99

References ……...101

LIST OF FIGURES

Figure Page

Figure 1.1. Schematics of (a) propagating surface plasmon resonance and (b) localized surface plasmon resonance[56].……..……..5

Figure 1.2. (a) Route 1: Emission enhancement relies on the interaction between QD emission and surface plasmon resonance (SPR) around the same wavelength. (b) Route 2: Excitation enhancement results from the extra near-field excitation of QDs by the surface plasmons created by far-field illumination……...7

Figure 1.3. (a) Schematic showing the process of plasmonic patch-enhanced fluoroimmunoassay implemented in a glass bottom 96-well plate, demonstrating the wide applicability of the plasmonic patch. (b) Fluorescence intensity maps of immunoassays corresponding to different concentrations of KIM1 with unenhanced assays and with plasmonic patch substrate. (c) Plot showing fluorescence intensities corresponding to different concentrations of KIM1. The limit-of-detection is enhanced by 300 times over plasmonic patch compared to unenhanced assay…….12

Figure 1.4. Disk-coupled dots-on-pillar antenna array (D2PA) plate and immunoassay. (a) Schematic (overview and cross-section) of D2PA plate without an immunoassay. D2PA has an array of dense three-dimensional (3D) resonant cavity nanoantennas (formed by the gold disks on top of periodic nonmetallic pillars and the gold backplane on the pillar foot) with dense plasmonic nanodots inside and couples the metallic components through nanogaps. (b) Schematic of the immunoassay on the D2PA, consisting of a self-assembled monolayer (SAM) of adhesion layer, Protein-A (as capture layer) and human-IgG prelabeled with IRDye-800cw (as prelabeled biomarker). (c) Fluorescence intensity vs IgG concentration on D2PA (squares) and glass plate reference (circles)……...13

Figure 1.5. Working principle of MB-SPR sensor[73] .……...…….15

Figure 1.6. Isofrequency surfaces of (a)dielectric materials and (b-c)hyperbolic metamaterials..17

Figure 1.7. Schematic of (a) multilayer and (b) nanowire based hyperbolic metamaterials indicating parallel and perpendicular permittivities and the unit cell (dashed), respectively[75].18

Figure 1.8. (a) Schematic of multilayered HMM with embedded QDs. (b) Cross-sectional SEM image. (c) Top view SEM image of bulls-eye grating. (d) Scattering intensity spectra of HMM with and without photonic crystal grating……..20

Figure 1.9. Schematic of QD LED with transparent substrate, ITO anode (Orange), hole transport layer (green), QD layer (Red), electron transport layer (yellow), and metal cathode……...22

Figure 1.10. Several schemes of QD LED enhancement using plasmonic arrays and nanoparticles embedded in different layers of LEDs[77-81]……...23

LIST OF FIGURES (Continued)

Figure 2.1. (a) Schematic of conventional focused-ion beam (FIB) patterning process: (1) deposition of working metal over substrate and (2) direct ion beam milling resulting in formation of blunt edges. (b) Schematic of metal assisted focused-ion beam (MAFIB) patterning process: (1) deposition of working metal and sacrificial Al layer over a substrate, (2) ion beam milling, and (3) removal of the sacrificial metal yielding sharp pattern edges……27

Figure 2.2. SEM images of dual line patterns fabricated by conventional FIB and MAFIB milling processes with 100 nm line width and various center-to-center inter-line distances (a) 400 nm, (b) 200 nm, and (c) 100 nm. Red and green circles indicate the difference in surface roughness created by FIB and MAFIB processes. Inset depicts the cross-sectional structure. (d) Cross-sectional SEM images of etched lines with an inter-line distance of 400 nm and each line width of 100 nm. Arrows indicate the blunt and sharp edges created by conventional FIB and MAFIB processes, respectively. Scale bars indicate 500 nm for all images……..32

Figure 2.3. (a) Template fabrication process. (b) Top view SEM image of a Si template (Inset: cross-sectional image). (c) SEM image of wedge array transferred on UV curable polymer. Scale bar: 500 nm…….35

Figure 2.4. (a) SEM images of silicon groove templates before Al removal with various groove angles—27°, 36°, 42°, and 52°. (b) V-groove array silicon templates with two different periods (400 and 500 nm). Scale bar: 500 nm……..37

Figure 2.5. (a) Schematic of an open-ring nanostructure array with a 500 nm period, 100 nm depth, and 200 nm thickness. SEM images of the device fabricated by using conventional FIB process (b), and MAFIB process (c). Scale bar: 500 nm……..39

Figure 2.6. Measured nonpolarized absorption spectra of the open-ring nanostructure array device fabricated by using conventional FIB and MAFIB processes……40

Figure 2.7. SEM images of Au dimple arrays fabricated using (a) FIB and (b) MAFIB. (c) FDTD simulation of electric field intensity with sharp and blunt edges. (d) Photoluminescence spectra of QDs over dimple arrays made using FIB and MAFIB, Au and glass……41

Figure 3.1. Schematic of metal-assisted focused-ion beam nanopatterning: (i) deposition of working metal on substrate, (ii) deposition of sacrificial metal, (iii) ion beam milling, and (iv) removal of sacrificial metal. (v) spin-coating of QD (dispersed in PVP) solution to form a thin layer on the nanostructure……..47

Figure 3.2. Schematic of FDTD simulation model with perfectly matched layer (PML) boundary conditions and an array of nanostructures with a dipole emitter placed 10-nm above the Ag surface in one of the unit cells at the center…….49

Figure 3.3. Microfluidic flow cell (1.2 μL volume) preparation flow: (i) fabricate ORA metal-assisted focused ion beam milling on a 200-nm thick silver coated silicon substrate using, (ii) create a flow channel defined by spacer layers using polyimide/PET/polyimide thin film (inset), (iii) connect inlet and outlet polyimide micropipes, (iv) fill the air-gaps with UV curable polymer so as to avoid leakage or bubble formation, and (v) encapsulate the structure with a cover glass followed by curing the polymer with 365- nm UV light exposure for 10 minutes. The resulting chip will then be connected to solutions and a syringe pump through microtubings for the test…..50

Figure 3.4. Schematics and SEM images of the (a) engraved Ag open-ring nanoarray (ORA) and (b) Ag dimple nanoarray (scale bars: 200 nm). The structures were spin-coated with a 30-nm-thick poly- (vinylpyrrolidone) (PVP) layer embedded with CdSe/ZnS QDs to evaluate fluorescence enhancement. The combined QD photoluminescence (PL) spectra and absorption spectra of (c) the ORA with a 340 nm period, 100 nm depth, and 100 nm width and (d) the dimple nanoarray with two different periods (280 and 350 nm) and 100 nm depth…….53

Figure 3.5. PL spectra of red QDs (610 nm emission) and green QDs (540 nm emission) on (a) a 340 nm period ORA substrate, (b) a 350 nm period dimple nanoarray, and (c) a 280 nm period dimple nanoarray substrate. All QDs were excited by a 380 nm continuous-wave light source. Enhancement factor (EF) is defined by the ratio of the peak PL intensity on the nanostructures (ORAs or dimple nanoarrays) to that on the glass. (d) Fluorescence images of the enhanced QD emission on the ORAs and dimple nanoarrays in the square areas. Outside the squares are plane Ag surfaces. (e) Enhancement factors of the red QDs on ORA and plane Ag substrates as functions of excitation wavelength. (f) The combined emission and absorption spectra of red QDs, and absorption spectra of ORAs. The level of QD absorption spectrum is exaggerated. (g) Diagram represents the interaction between the UV-excited QDs and surface plasmons at the emission wavelength λem that results in emission enhancement (indicated by route 1). ORAs do not absorb UV light efficiently. (h) Diagram represents the QD−surface plasmon interactions under a visible-light excitation. Apart from the route 1 emission enhancement, the visible-light also creates surface plasmons on ORAs that enhance the excitation of QDs at the excitation wavelength λex (indicated by route 2)……..55

Figure 3.6. Position-dependent enhancement factors of red (610 nm) and green (540 nm) dipole emitters over (a) ORAs (340 nm period), (b) dimple arrays with 350 nm period, and (c) dimple arrays with a 280 nm period. ORAs yield strong enhancements for both red and green emitter while the dimple arrays show wavelength-selective enhancement. (d−f) Electric field profiles are obtained with the dipole emitter placed at the center and oriented perpendicularly to the substrate. Both red and green emitters induce high-intensity hot-spots over a large area of the ORA, whereas the dimple arrays display the hot-spots induced only by specific emission wavelengths……..58

Figure 3.7. (a) Schematic of molecular beacons (MBs) anchored on ORAs and plane silver surfaces. Background intensities IB1 and IB2 denote the quenched fluorescence on plane silver and ORA surfaces before hybridization. ID1 and ID2 represent the fluorescence signals of the hybridized MBs on plane silver and ORA surfaces, respectively. (b) The absorption spectrum of

LIST OF FIGURES (Continued)

an ORA in an aqueous environment (1.33 refractive index) that overlaps the emission and absorption spectra (measured) of the fluorophore. (c) Schematics of the quenching and enhancement mechanisms resulting from the fluorophore−plasmon interaction. Route 1 represents enhanced emission, and route 2 the enhanced excitation……60

Figure 3.8. Fluorescence intensities on the (a) ORA and (b) plane Ag surface in the presence of target and nontarget DNA. Three devices were evaluated for the detection assays. The shaded areas indicate the initial background fluorescence intensity IB at quenching status. The limit of detection (LOD) is about 300 fM for ORA and 6 nM for plane Ag, respectively. (c) Signal-to-noise ratio (SNR) acquired from the ORA and plane Ag substrates with reference to IB. The inset microscopic image shows the Ag ORA sensors integrated into a 1.2 μL-sized microfluidic chamber. (d) Fluorescence images of the device at various concentrations of complementary target DNA. The dimension of the ORA is 150 μm × 150 μm……63

Figure. 4.1. SEM image and schematic of an Al dimple array with a 550-nm period and 240-nm hole diameter fabricated using focused-ion beam milling and spin coated with a QD-embedded PVP thin film (scale bar: 500 nm). (b) Schematics of QD enhancement routes contributed by different QD-surface plasmon coupling pathways. Route 1: Emission enhancement relies on the interaction between QD emission and surface plasmon resonance (SPR) around the same wavelength. Route 2: Excitation enhancement results from the extra near-field excitation of QDs by the surface plasmons created by far-field illumination. Both enhancement routes are realized by the same excitation wavelength □ex=390 nm. The enhancement route is determined by the choice of SPR wavelength of the substrate. (c) Measured emission and absorption spectra of green and red QDs with the emission peak wavelengths of □em=540nm and 610 nm, respectively. (d) Absorption spectra of the 30-nm thick PVP-coated Al dimple arrays with 350-nm, 450-nm, and 550-nm periods each of which yields a major absorption peak at 390 nm, 520 nm, and 610 nm, respectively……68

Figure. 4.2. Measured photoluminescence (PL) spectra of green and red QDs spin-coated on (a) the UV plasmonic dimple array with a 350-nm period and (b) the visible plasmonic dimple arrays with 450-nm and 550-nm periods. All samples were excited by a 390-nm light source……72

Figure. 4.3. Calculated position-dependent enhancement factors (EFs) of a single UV-excited red (540-nm emission) or green (610-nm emission) QD (dipole emitter) on a unit cell of (a) a UV plasmonic dimple array with the 350-nm period and (b) visible plasmonic dimple arrays with 450-nm and 550-nm periods. The dipole emitter is placed 10 nm above the metal surface and is positioned with a step size of 20 nm. (c) Cross-sectional electric field profiles of the 350-nm period UV plasmonic dimple array under far-field excitation of 390-nm light. (d) Cross-sectional electric field profiles of the 450-nm period (left) and 550-nm period (right) visible plasmonic dimple arrays induced in the near field by a dipole emitter with 540-nm or 610-nm emission wavelength placed at 10 nm above the edge of the hole on an Al dimple array……74

LIST OF FIGURES (Continued)

Figure 5.1. The LDOS (normalized by vacuum) available to a quantum emitter located on the top of HMM with (a) 4, (b) 8, and (c) 16 bi-layers. The number of HMM modes increase with the bi-layers leading to LDOS enhancement……78

Figure 5.2. (a) Schematic of Ag/ITO based multilayered HMM spin coated with CdSe/ZnS QDs with emission wavelength peak at 540 nm. (b) Cross-sectional SEM image of 4 bi-layers HMM with filling factor of 0.25 and total thickness of 320 nm. (c) permittivity along x-axis for three different filling factors of HMM. (d) Simulated and (e) measured transmission spectra of visible light through the HMM……...80

Figure 5.3. (a) Parallel and perpendicular permittivity of 0.25 filling factor HMM pointing epsilon-near-zero (ENZ) point. (b) Cross-sectional SEM images of 320 nm thick HMMs formed by various unit cell thickness- 80 nm (4 BLs), 40 nm (8 BLs), and 20 nm (16 BLs). (c) Analytical and (d) measured transmission spectra of all three HMMs (Inset: bird eye images of HMMs). (e) Iso-frequency curves of HMMs……....82

Figure 5.4. (a) Schematic of the self-assembly of polystyrene nanoparticle monolayer. (b) Top view and (c) cross-sectional SEM images of the resulting nanoparticle monolayer. Photoluminescence spectra of 540 nm emission quantum dots spin-coated over HMMs with (d) 4 BLs, (e) 8 BLs, and (f) 16 BLs with outcoupling via a monolayer of polystyrene microbeads of 200, 500 and 750 nm in diameter……...84

Figure 5.5. (a) Cross-sectional electric field profiles of plane HMM and HMM with 200, 500, 750 and 1000 nm polystyrene microbead assembly along with (b) contour far-field intensity profiles showing a very strong intensity of HMM with 750 nm PS microbead diameter. (c) Out-coupling factor with respect to PS microbead assembly……86

Figure 5.6. Simulated (shaded) and measured (dotted) scattering intensity plots of quantum dots spin-coated over a (a) glass, (b) HMM, HMM with self-assembled polystyrene monolayer of (c) 200 nm, (d) 500 nm, and (c) 750 nm in diameter……88

Figure 6.1. (a) Schematics of microLED chip with and without nanoparticles indicating the presence of leakage and an eventual emission enhancement after adding nanoparticles. The GaN-based LED is encapsulated with polymer layer followed by formation of silicon based polymer well for drop casting of the emissive layer. (b) Measured normalized absorbance spectra of 30 nm silver nanoparticles dispersed in DI water and 300 mg/mL PVP solution leading to a redshift. The blue color faded region indicates the excitation range and the yellow color faded spectra indicates the emission of CDs……94

Figure 6.2. (a) Transmission and enhancement factors of CD emissive layer while increasing the Ag nanoparticle concentration. A maximum enhancement of 3.68 times is observed minimizing leakage by ~25%. The concentration at which the leakage becomes zero is found to have 2-fold

emission enhancement. (b) Spectra indicating the transmission in UV regime and photoluminescence of CD (inset) at Ag concentrations increasing from 0 to 3.125 nM…….96

Figure 6.3. (a) Bird-eye image of GaN-based UV LED chip with 9 LEDs of dimensions 1 mm X 1 mm. (b) Enhanced microLED with zero UV leakage, made over the center UV LED. Microscopic view of LEDs (c) with and (d) without emissive layer. This comparison shows the efficiency of UV leakage minimization with Ag nanoparticles……...97

Figure 6.4. CIE chromaticity diagram of the excitation and emission light showing the suitability of CD based microLED for CMYK based display technology……...98

LIST OF TABLES

Table Page

1.1 Summary of common QD enhancement techniques……..2

1.2 Overview of metal enhance fluorescence based protein sensors[62]……..10

1.3 Overview of QD LED enhancement……23

CHAPTER 1. INTRODUCTION

Colloidal semiconductor quantum dots (QDs), often referred to artificial atoms, have attracted much attention over the past decades, primarily because of their optical properties [1-11]. The narrowband emission and broadband absorption, similar to those of atoms, with an emission wavelength that can be tuned with slight changes in size and composition along with decent photostability make QDs attractive for a broad range of optoelectronic as well as biomedical applications. QDs find their key applications in solar cells[12 - 22], display devices[23 - 32], biosensing technologies[33,34], bioimaging[35-44], lasers[45-47], and as photocatalysts[48]. On the other hand, organic fluorophores are well known for their applications in labeled biosensing techniques such as DNA sensing, protein sensing, and bioimaging.

In the past, various organic dyes and QDs were utilized for biosensing and imaging technologies. However, due to the weak emission of these fluorescent crystals, the sensitivity of biosensors becomes limited leading to a strong necessity of spontaneous emission enhancement. As a result, the control over spontaneous emission becomes important for many applications in biosensing technologies, solar cells, QD light emitting diodes (LEDs), QD based micro LEDs, and efficient single-photon sources. Spontaneous emission can be controlled by modifying the excitation rate, radiative decay rate, local density of photonic states (LDOS), and electric-field strength at the emitter’s location using optical cavities. However, each technique of spontaneous

emission enhancement has its weaknesses. Table 1.1 summarizes the technique, application, and respective disadvantages.

Table 1.1 Summary of common QD enhancement techniques

Technique	Applications	Disadvantages
Metal films	(a) Biosensing	(a) Weak enhancement (b) Low sensitivity (c) No selectivity
Plasmonic nanoparticles	(a) Biosensing (b) Solar cells (c) Light emitting diodes	(a) Weak enhancement (b) Lack of broadband enhancement (c) Low coupling strength
Plasmonic gratings	(a) Biosensing (b) Light emitting diodes (c) Lasers (d) Structural colors	(a) Poor precision in nanofabrication (b) Lack of broadband enhancement
Photonic crystals	(a) Biosensing	(a) Weak enhancement
Hyperbolic metamaterials	(a) Waveguides (b) Biosensing	(a) Lack of efficient outcoupling (b) Large unit cell thicknesses

	(c) Lack of large area outcoupling

As listed in Table 1.1, in contrast to nanoparticles and photonic crystals, plasmonic gratings and hyperbolic metamaterials have the scope of stronger enhancement due to their strong electric field strength and an infinite number of LDOS. However, they lack the capability of broadband enhancement, deviated enhancement factors due to low precision in nanofabrication, and lack of efficient outcoupling in hyperbolic metamaterials.

In this chapter, QD spontaneous emission enhancement techniques will be reviewed. Among them, surface plasmon resonance (SPR) based techniques, the reported applications, and challenges will be discussed in more details. Then a new nanofabrication technique, plasmonic gratings, DNA sensing, hyperbolic metamaterials, and microLED display applications will be discussed in further chapters.

1.1 Surface Plasmon Resonance

When an electromagnetic wave is incident over a metal substrate, under certain conditions, the electrons on the surface of the metal starts oscillating. These collective oscillations of the conduction electrons on the metallic surface are referred to be as surface plasmons and surface plasmon resonance (SPR) occurs when the momentum of excited light matches with the momentum of surface plasmon waves[49]. The

intensity and the wavelength of resonance depend on the material properties, metal nanostructure dimensions, incident light, and the refractive index of the surrounding media. There are two types of SPRs: (1) propagating surface plasmon polaritons (SPPs)[50-54] and localized surface plasmon resonance (LSPR)[55] as shown in Figure 1.1. Propagating SPR requires to have momentum matching condition, which is possible by tuning the dimensions of nanostructures or by light incidence at different angles, for resonance excitation. The resonance occurs when the momentum of the incident light matches with the momentum of SPPs. The dispersion relation of SPPs is

$$k_{spp} = k_0 \sqrt{\frac{\varepsilon_d \varepsilon_m}{\varepsilon_d + \varepsilon_m}},$$

Where $k_0 = \omega/c$ is the momentum of incident light, ε_d is the permittivity of the surrounding media and ε_m is the permittivity of the metal. The oscillating nature of the SPPs and the associated fields are shown in Figure 1.1(a).

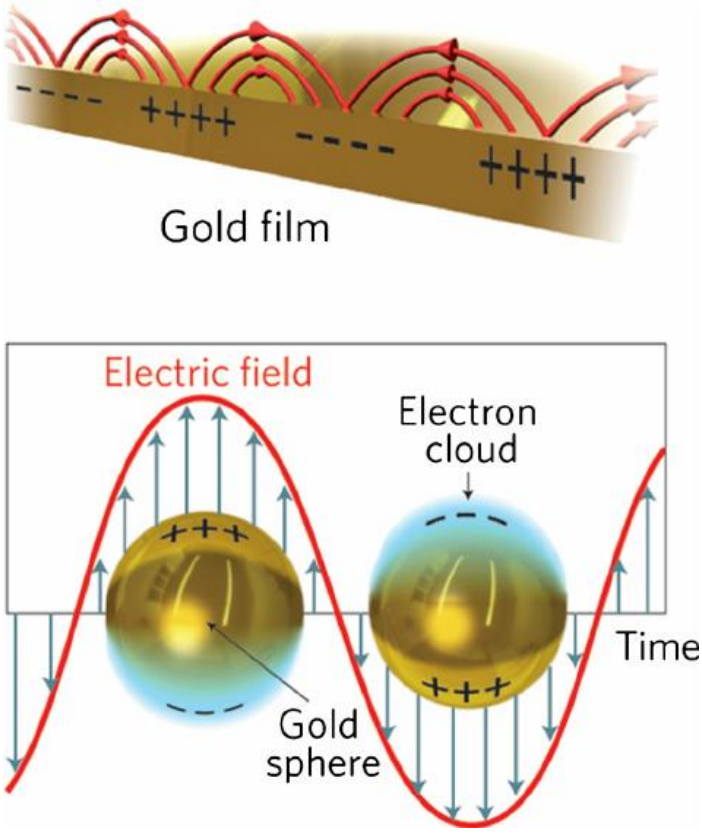

Figure 1.1. Schematics of (a) propagating surface plasmon resonance and (b) localized surface plasmon resonance[56].

On the other hand, when surface plasmons are confined on either periodic nanostructures, colloidal metal nanoparticles or other nanosystems, LSPR is observed. These modes are highly localized electromagnetic fields outside the particles.

Both propagating SPR and LSPR are sensitive to local refractive index changes which may shift the resonant wavelength and modify the intensity of electric fields also termed as ‘hot-spots.’ The hot-spot intensity of metal nanostructures can influence the optical processes such as fluorescence, absorption of the incident light, and Raman scattering. By utilizing propagating SPR and LSPR, several plasmonic substrates have

been designed over the past decades for application such as refractive index based biosensing[57], metal-enhanced fluorescence (MEF)[58], fluorophore-labeled biosensing[59], surface-enhanced Raman scattering[60], and biomolecular interaction[61]. MEF is the major technique utilized for several biosensing and optoelectronic applications.

1.2 Metal-Enhanced Fluorescence

Fluorescent crystals such as QDs or molecules such as fluorophores are easily affected by their surrounding media. When QDs are located nearby conductive metallic nanoparticles, nanostructures or any other nanosystems, they lose their property of free-space conditions in ways that increase or decrease the incident electric field, which also modify their respective decay rates. As shown in Figure 1.2, QDs once excited with incident electromagnetic energy, E_{ex}, undergo two major types of decays namely radiative and non-radiative, with their respective decay rates, Γ_r and Γ_{nr}. These effects can be understood in terms of changes in local density of photonic states (LDOS), where a large mode density provides more radiative decay pathways and larger radiative decay rates, otherwise called as Purcell effect (further details in subsequent chapters). The modification of radiative decay rate is termed as spontaneous emission rate at which a QD emits photons, has a very low effect on the solvent and the temperature, and hence it is highly dependent on its oscillator strength. An attempt to increase this decay rate via a plasmonic environment leads to several biomedical and

optoelectronic applications, by engineering distance dependent emission enhancement, increase of quantum yields, and techniques involving broadband enhancement.

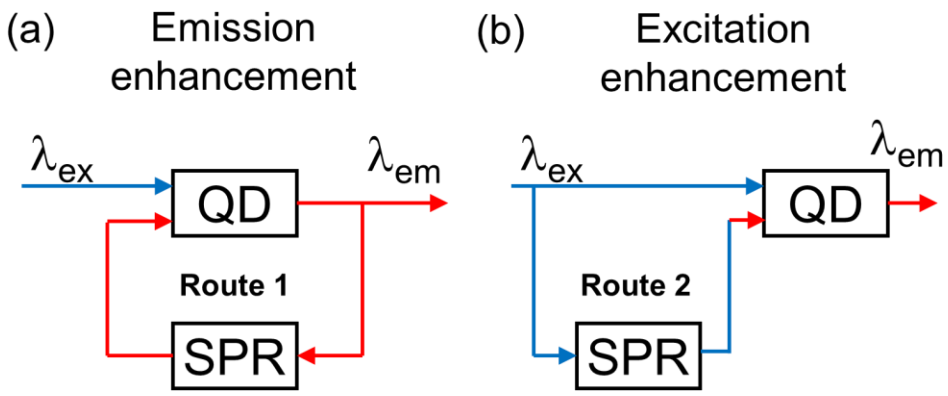

Figure 1.2. (a) Route 1: Emission enhancement relies on the interaction between QD emission and surface plasmon resonance (SPR) around the same wavelength. (b) Route 2: Excitation enhancement results from the extra near-field excitation of QDs by the surface plasmons created by far-field illumination.

The second mechanism of enhancement occurs through excitation enhancement over the QD in which additional excitation energy supports extra decay rate (Γ_{add}) for enhanced emission. The excitation enhancement results from the extra near-field excitation of QDs by the surface plasmons created by far-field illumination as shown in the schematic of Figure 1.2(b).

Both the routes of QD enhancement lead to an increase in quantum yield (Q) and reduce the fluorescence lifetime (τ):

$$Q_0 = \frac{\Gamma_r}{\Gamma_r + \Gamma_{nr}}$$

$$Q_f = \frac{\Gamma_{add} + \Gamma_r}{\Gamma_r + \Gamma_{add} + \Gamma_{nr}}$$

$$\tau_0 = \frac{1}{\Gamma_r + \Gamma_{nr}}$$

$$\tau_f = \frac{1}{\Gamma_r + \Gamma_{add} + \Gamma_{nr}}$$

Another major factor for fluorescence enhancement is the distance between QD and the conducting material, which may increase the emission based on the mechanisms discussed above, but also may reduce the emission called as fluorescence quenching. QD quenching occurs through two key mechanisms: (1) electron transfer into the metal, and (2) Forster resonance energy transfer (FRET). When a QD is located close to a metal nanostructure or a nanoparticle, upon excitation, the electron will go from valence band to conduction band and recombine into the metal substrate because of shorter distance leading to QD quenching.

On the other hand, quenching through FRET is another major phenomenon for understanding biological systems and thin film device development. FRET is highly dependent on the distance between QD and resonator and as a result, when applied to optical microscopy, it is utilized in measuring nanometer-scale distances and the changes in distances, both in vitro and in vivo. Its sensitivity to distance allows investigation of molecular level interactions.

To understand the mechanism of FRET, consider a QD and a plasmonic resonator situated closer to each other with distance less than 5 nm, otherwise called as Forster distance. When the QD is in an excited electronic state, it may transfer its excitation energy to nearby acceptor resonator in a non-radiative fashion through long-range dipole-dipole interactions. According to the theory, an excited QD is treated as an oscillating dipole that can undergo an energy exchange with a second dipole having a similar resonance frequency. If a nanostructure is designed to have a peak of resonance spectra overlap the emission of QD, at a distance less than Forster distance, QD quenching occurs due to FRET via dipole-dipole interactions. Unlike radiative interactions, FRET can yield a significant amount of structural information concerning the emitter-resonator pair.

The strong distance-dependence of the FRET efficiency has been widely used in realizing the structure and dynamics of nucleic acids, DNA sensing, and visualization of intermolecular association and in the development of binding assays. Thus, the distance becomes an important factor in QD enhancement, where, shorter distances lead to quenching, and longer distances will have no Purcell effect or excitation enhancement. So, a QD-plasmonic system needs to be designed in a way, to have an optimal QD-metal distance for achieving a highest possible enhancement. This mechanism plays a key role in DNA sensing application as discussed in the subsequent chapters.

The engineering of QD quenching and majorly QD enhancement is found to have applications in varied fields of biosensing, optoelectronics and display technology. In

this chapter, some of the applications are discussed in more detail through some literature to understand the need of QD enhancement techniques.

1.3 Applications and Methods of Fluorescence Enhancement

1.3.1 Protein sensing

Protein sensing is vital in biological study and medical diagnosis such as cancer detection. Over the past decade, several researchers have presented the utilization of metal-enhanced fluorescence into biosensing technologies such as fluorescence microarray scanners, fluorescence microscopes, or microtiter plate readers as well as the development of compact devices which utilizes this amplification scheme. Metal nanostructures combined with immunoassays offers a highly sensitive detection with very low detection times as listed in Table 1.2.

Table 1.2 Overview of metal-enhanced fluorescence based protein sensors[62]

Analyte	Plasmon mode	Limit of detection	Detection time	Ref.
a-mouse IgG	LSPR	20 fM	20 min	[63]
Streptavidin	SPP	50 pM	10 min	[64]
Human IgG	SPP	6.7 fM	60 min	[65]
Human IgG	LSP	0.57 pM	60 min	[66]
Human IgG	LSP	0.3 fM	60 min	[67]

KIM 1	LSP	9.1 fM	NA	[68]

The protein sensing is mostly done using sandwich fluoroimmunoassay method, which involves following major steps: (i) capture of target antigen by an immobilized antibody; (ii) binding of the biotinylated detection antibody to the captured antigen; and (iii) binding of the fluorescently labeled protein. Some of the recent advances in detection of streptavidin and human IgG using plasmonic structures could reach limit-of-detection as low as 9.1 fM and 0.3 fM, respectively (see Table 1.2).

Plasmonic patch-enhanced fluoroimmunoassays by Luan et al. [68] could reach streptavidin detection limits as low as 9.1 fM. The addition of plasmonic patch after the last step (i.e., binding of the fluorescently labeled streptavidin) resulted in a large enhancement of the fluorescent intensity and significantly improved the limit-of-detection (three times of standard deviation at zero target concentration). Briefly, the plasmonic patch is made by dispersing gold nanorods into a polymer followed by curing it. The detection method is shown in Figure 1.3.

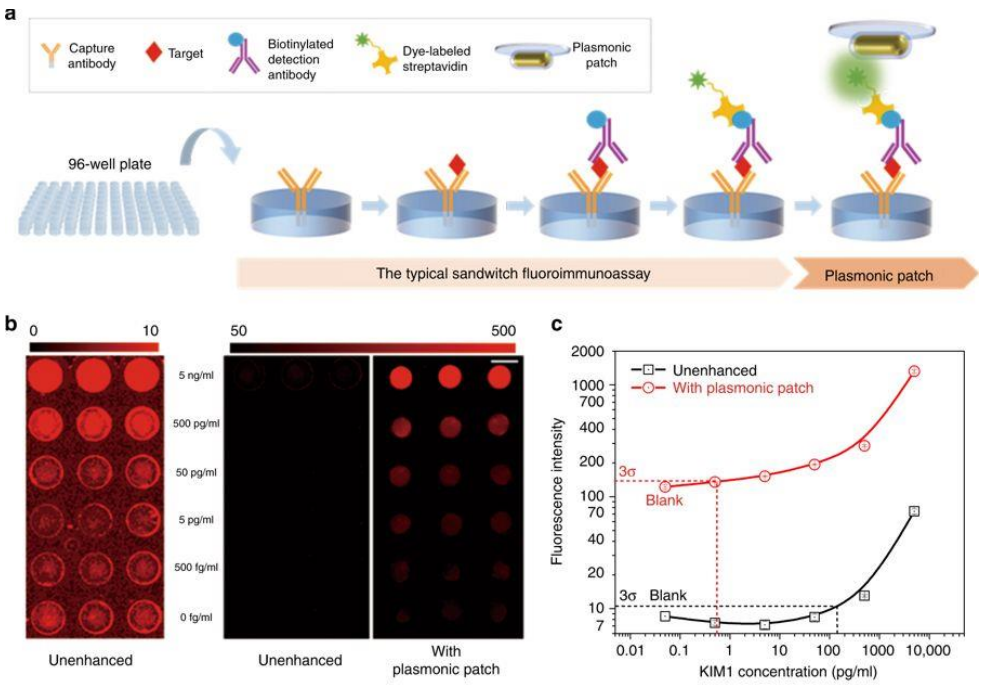

Figure 1.3. (a) Schematic showing the process of plasmonic patch-enhanced fluoroimmunoassay implemented in a glass bottom 96-well plate, demonstrating the wide applicability of the plasmonic patch. (b) Fluorescence intensity maps of immunoassays corresponding to different concentrations of KIM1 with unenhanced assays and with plasmonic patch substrate. (c) Plot showing fluorescence intensities corresponding to different concentrations of KIM1. The limit-of-detection is enhanced by 300 times over plasmonic patch compared to unenhanced assay.[68]

Another example of protein detection using plasmonic arrays is detection of human IgG using disk-coupled dots-on-pillar antenna array (D2PA)[67] as shown in Figure 1.4.

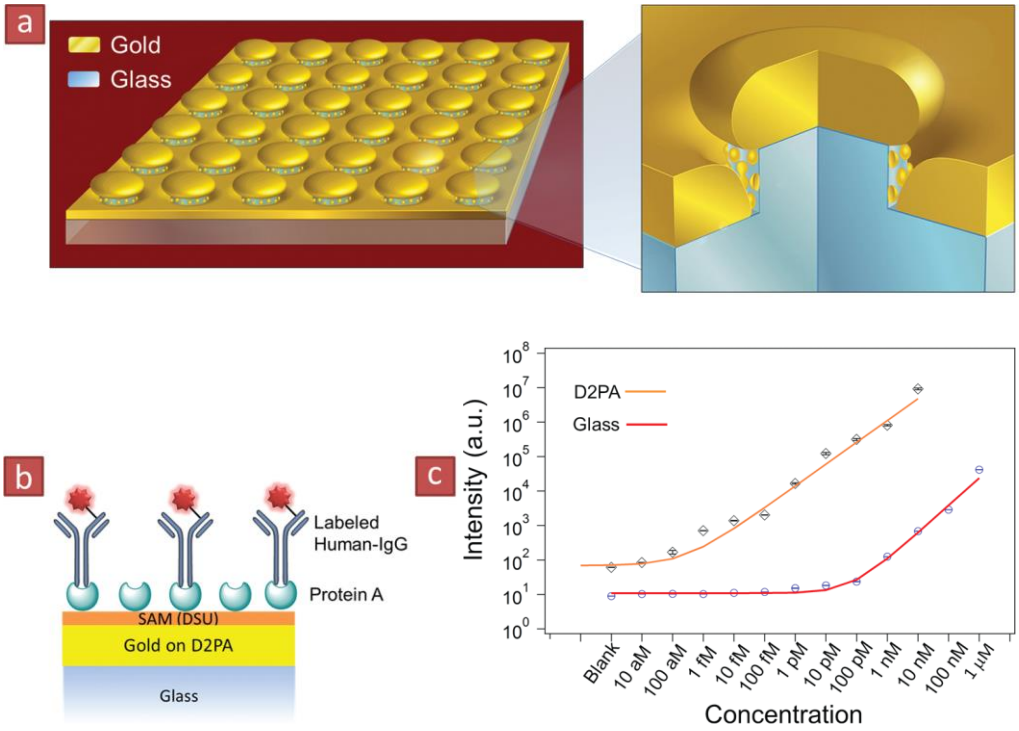

Figure 1.4. Disk-coupled dots-on-pillar antenna array (D2PA) plate and immunoassay. (a) Schematic (overview and cross-section) of D2PA plate without an immunoassay. D2PA has an array of dense three-dimensional (3D) resonant cavity nanoantennas (formed by the gold disks on top of periodic nonmetallic pillars and the gold backplane on the pillar foot) with dense plasmonic nanodots inside and couples the metallic components through nanogaps. (b) Schematic of the immunoassay on the D2PA, consisting of a self-assembled monolayer (SAM) of the adhesion layer, Protein-A (as capture layer) and human-IgG prelabeled with IRDye-800cw (as a prelabeled biomarker). (c) Fluorescence intensity vs. IgG concentration on D2PA (squares) and glass plate reference (circles).

The D2PA nanostructures were fabricated using an approach that combines nanoimprint with self-aligned self-assembly. The pillars were patterned first on the silica wafer by nanoimprint and reactive ion etching. Then, a thin gold layer was evaporated onto the wafer, which simultaneously deposited the gold nanodisk on the pillar top, the gold backplane, and gold nanodots on the pillar sidewall. During the deposition, due to the elevated temperature; and together with the nonwetting property of gold on the silica surface, the gold self-assembles into the nanodots with a small gap in between and self-aligned precisely next to the gold nanodisk. The target detection is similar to the previously discussed example, the sandwich assay detection method. Self-assembled layers over the gold capture protein A followed by capturing human IgG prelabeled with IRDye-800cw. An extraordinary QD enhancement of 7400 times occurs due to the fluorophore present at an optimal distance of 10 nm from the metal nanostructures leading to a limit-of-detection of 0.3 fM.

1.3.2 DNA sensing

DNA sensing is essential for genetic screening[69], medical diagnosis[70], forensic analysis[71], and single-nucleotide polymorphism profiling[72]. Among several approaches for detection of oligonucleotides in a solution, the use of DNA hairpins as molecular beacons (MBs) has proven to be a useful method. MBs are single-stranded DNA hairpin structures with a sequence complementary to the target as well as a double-stranded stem region equipped with a fluorophore and a quencher causing the fluorescence to be quenched in close proximity by FRET. Upon hybridization with

target DNA, the stem opens, and fluorophore emits light. MBs are known to have extraordinary stability and high selectivity.

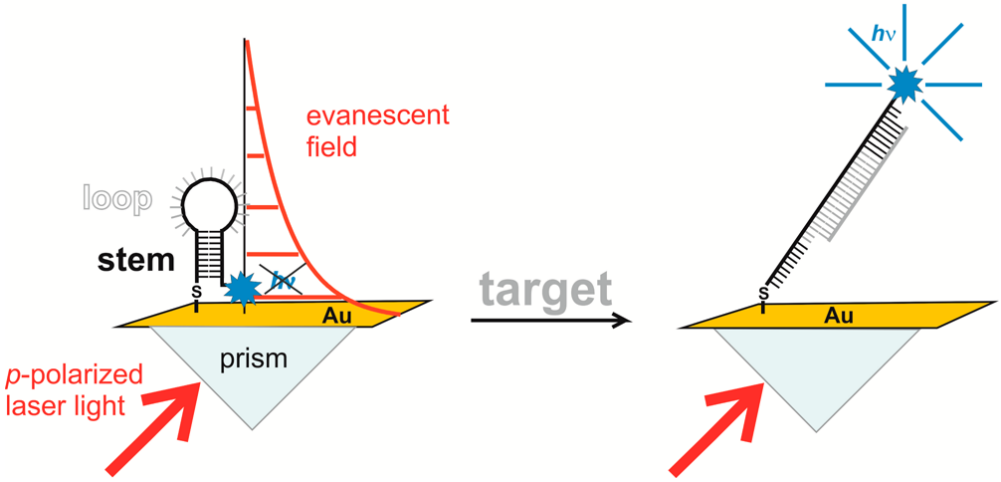

Figure 1.5. Working principle of MB-SPR sensor[73].

The MB-based DNA sensing using SPR of gold substrate takes place in following major steps: (i) the thiol-terminated MB will be self-assembled onto the metal substrate; and (ii) as the target DNA hybridizes with the MB, the hairpin structure opens and the fluorophore attached to the MB emits with enhanced fluorescence due to the Purcell effect as shown in Figure 1.5. The limit-of-detection achieved using this method is 500 pM. However, due to the weak resonance and coupling strength of fluorophore and the gold substrate, the quenching and the enhancement at initial and final stages are vividly weak. This allows a scope of improvement in limit-of-detection using plasmonic nanostructures.

1.3.3 Hyperbolic metamaterials

In nature, materials such as metals or dielectrics are isotropic along all the directions with their permittivity being negative or positive, respectively. In vacuum, their linear dispersion and isotropic behavior of propagating waves implies a spherical isofrequency surface given by the equation:

$$k_x^2 + k_y^2 + k_z^2 = \omega^2/c^2$$

Where, $\vec{k} = [k_x, k_y, k_z]$ is the wave vector, ω is the frequency of radiation and *c* is the velocity of light in free space. However, if a material is engineered to have positive permittivity in one direction and negative permittivity in other directions, such a material shows an anisotropic behavior leading to a hyperbolic isofrequency surface (Figure 1.6) given by equation:

$$\frac{k_x^2 + k_y^2}{\varepsilon_{zz}} + \frac{k_z^2}{\varepsilon_{xx}} = \omega^2/c^2$$

Where, $\vec{\varepsilon} = [\varepsilon_{xx}, \varepsilon_{yy}, \varepsilon_{zz}]$ is the permittivity along all three directions with in-plane isotropic components are $\varepsilon_{xx}=\varepsilon_{yy}=\varepsilon_{\parallel}$ and out of the plane component is $\varepsilon_{zz}=\varepsilon_{\perp}$. Such an artificially engineered metamaterial is termed as hyperbolic metamaterial[74].

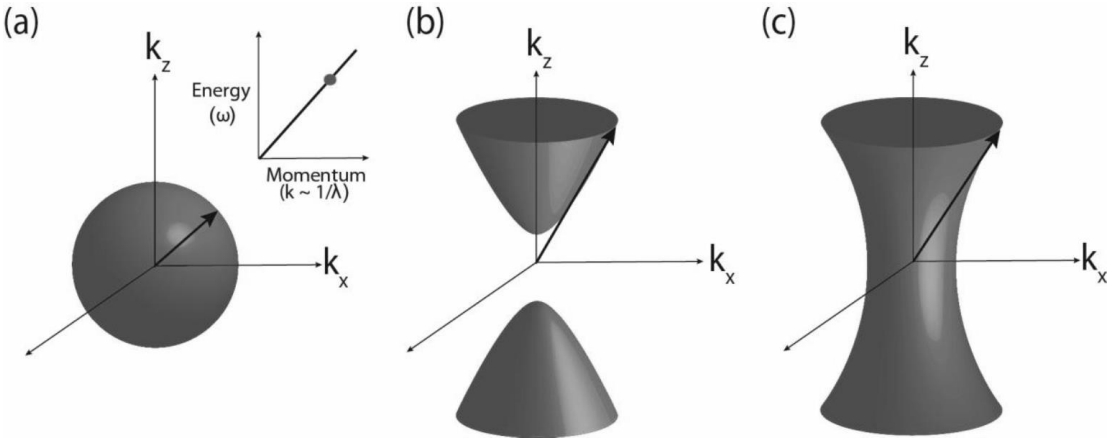

Figure 1.6. Isofrequency surfaces of (a) dielectric materials and (b-c) hyperbolic metamaterials.

The condition for anisotropy is $\varepsilon_{\parallel}.\varepsilon_{\perp} < 0$. The most important property of HMMs is related to behavior of waves with high-k waves. In hyperbolic media, the open form of isofrequency surface allows for propagating waves with infinitely large wavevectors. This unique property of high-k waves will be well utilized in Purcell effect of QDs or fluorophores.

HMMs are classified into two types: (i) Type I (Figure 1.6(b)), and (ii) Type II (Figure 1.6 (c)). Type I HMMs have one component of the dielectric tensor negative ($\varepsilon_{zz}<0$, $\varepsilon_{xx,}$ $\varepsilon_{yy}>0$) while Type II HMMs have two components negative ($\varepsilon_{zz}>0$, $\varepsilon_{xx,}$ $\varepsilon_{yy}<0$), respectively.

HMMs are usually made using two practical approaches, namely 1D and 2D HMMs. The fact that HMM acts as metal in some directions and dielectric in others leads to a requirement that both metals and dielectrics are utilized as building blocks. 1D HMMs

are otherwise called as multilayered HMMs. They are made by depositing alternate layers of metals and dielectric with metal filling factor, *f*. The high-k modes in HMMs are the result of the near-field coupling of the SPPs at each of the metal-dielectric interfaces in the structure. On other hand, 2D HMMs are made by embedding the metal nanowires in a dielectric medium as shown in the Figure 1.7.

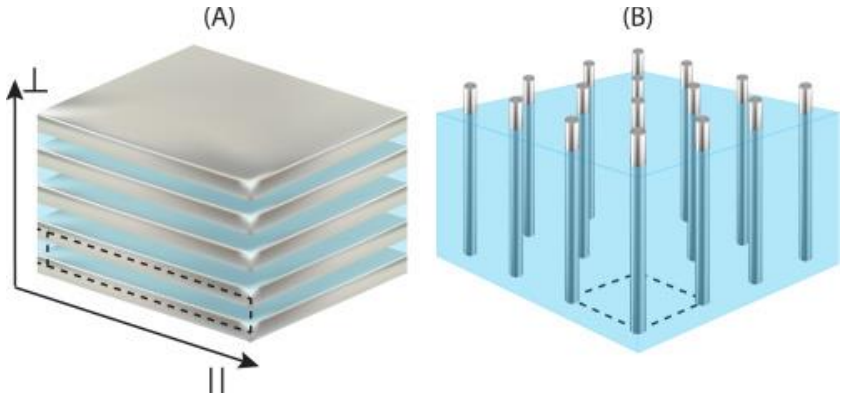

Figure 1.7. Schematic of (a) multilayer and (b) nanowire based hyperbolic metamaterials indicating parallel and perpendicular permittivities and the unit cell (dashed), respectively[75].

As discussed, in an ideal HMM, hyperbolic dispersion corresponds to an infinite local photonic density of states (LDOS). According to Fermi's golden rule, the spontaneous emission of quantum emitters is strongly influenced by density of available LDOS. When fluorescent dye or QDs are brought near HMM the interaction is dominated by the modes with highest density of states. As compared to the modes in vacuum, the hyperbolic high-k states dominate and the emitters preferentially couple to these modes.

This leads to decrease of lifetime and an increase of Purcell factor. However, all the enhanced waves are high-k waves and remain trapped inside the HMM. As a result, the far-field enhancement factor is not as high as plasmonic arrays. In the past, few researchers have demonstrated the outcoupling of these high-k waves through photonic crystal gratings.

One of the examples for outcoupling using photonic crystal grating is the use of Germanium-based Bullseye by Galfsky et al[76]. The multilayer HMM used in this research work is based on Ag/Al_2O_3 of unit cell thickness 32 nm with a metal filling ratio of 0.375 comprising 7 bi-layers as shown in Figure 1.8. The QDs are embedded inside the HMM to achieve a highest possible Purcell factor.

As shown in Figure 1.8(d), the non-patterned area over the HMM shows the scattering intensity of lower magnitude along with poor directionality. On the other hand, the HMM patterned with Ge based bullseye grating outcouples the light with a drastically increased directionality. The photonic crystal provides an additional momentum required for the evanescent wave on the surface of the HMM to propagate into the free space.

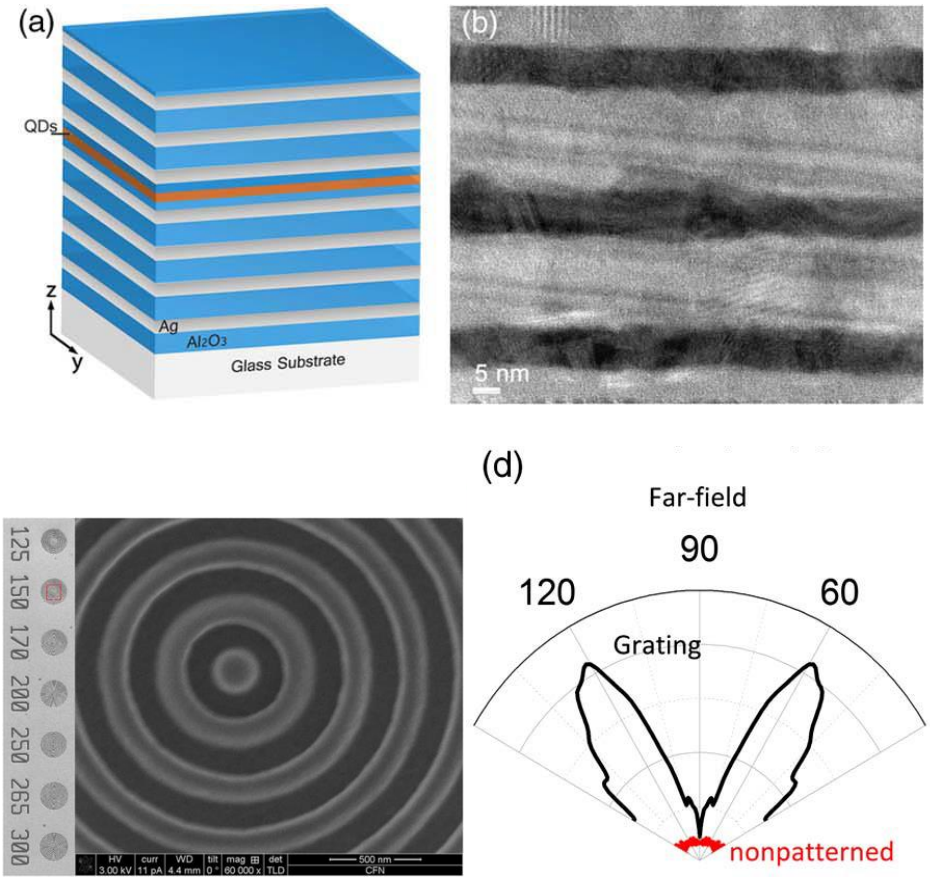

Figure 1.8. (a) Schematic of multilayered HMM with embedded QDs. (b) Cross-sectional SEM image. (c) Top view SEM image of bulls-eye grating. (d) Scattering intensity spectra of HMM with and without photonic crystal grating.

Although some attempts have been made in the past to outcouple the light, the enhancement factors achieved were much less than the ones with plasmonic arrays. Moreover, there is a much needed outcoupling mechanism over a large area on HMM, which may lead to several applications in biosensing, display and other optoelectronic devices.

1.3.4 Display technology

QD light emitting diodes (LEDs) have been well studied in the past few years. They are found to have great potential as devices for next-generation large area and flexible displays by replacing organic LEDs mainly due to their narrow emission spectra leading to a larger color gamut and longer device lifetimes. In addition, QD LEDs are processed at low temperatures and are compatible with light-weight, flexible, organic substrates. Although they have some major advantages over organic LEDs, they have a low electroluminescence efficiency (EL) because of structural and electrical limitations.

To enhance the EL of QD LEDs, one of the major approaches is by utilizing SPR based nanoparticles and nanostructures. Figure 1.9 shows the schematic of a typical QD LED. Briefly, the voltage applied to the two electrodes allows the electrons and holes to pass through the electron (ETL) and hole transport layers (HTL) followed by their recombination in the QD layer. As the electrons and holes recombine in the QD layer the energy is emitted in form of light through one of the transparent electrodes (typically ITO).

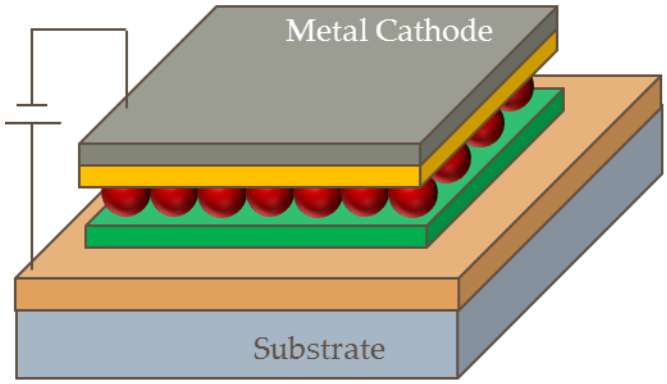

Figure 1.9. Schematic of QD LED with transparent substrate, ITO anode (Orange), hole transport layer (HTL, green), QD layer (Red), electron transport layer (ETL, yellow), and metal cathode.

To enhance the EL, plasmonic nanoparticles are embedded in the QD/ electron transport/ hole transport layers, with the metal nanoparticles usually coated with some ligands to avoid any possible quenching. Figure 1.10 shows some of the existing methods used for EL enhancement. Another method presented in the past is to utilize gold nanostructure arrays embedded inside the QD layer, fabricated using electron beam lithography. All the mechanisms follow the Purcell effect for achieving the enhancement, and the enhancement factors of some of the research works are summarized in Table 1.3.

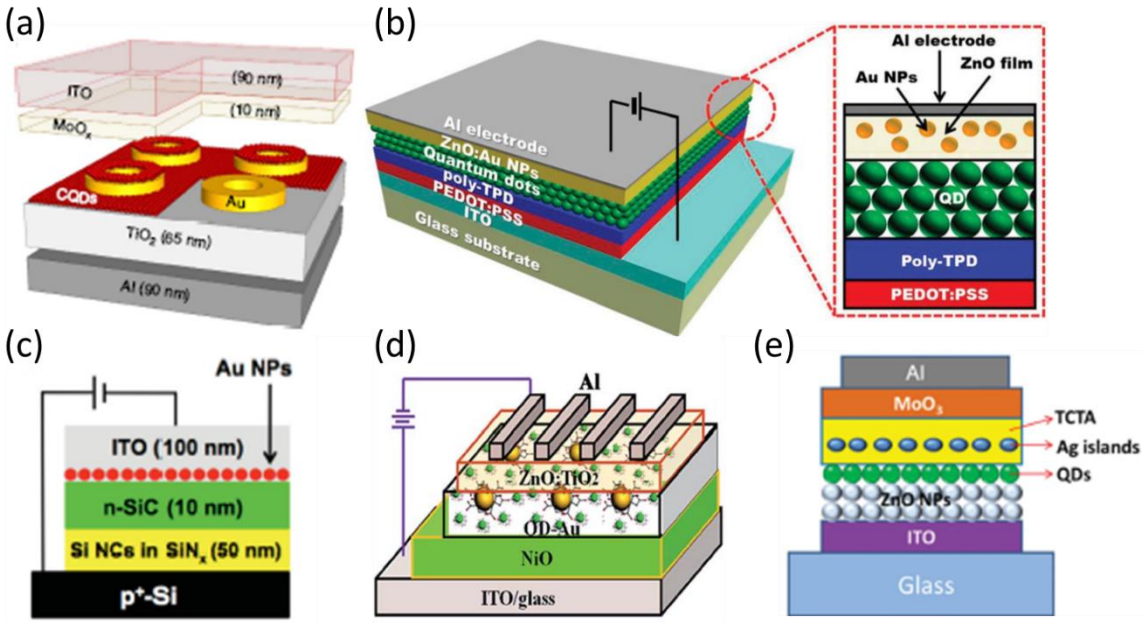

Figure 1.10. Several schemes of QD LED enhancement using plasmonic arrays and nanoparticles embedded in different layers of LEDs[77-81].

Table 1.3 Overview of QD LED enhancement

LED	Plasmon mode	EL enhancement factor	Ref.
Au NPs in ETL	LSPR	4.54	[78]
Au NPs in Si nanocrystal LEDs	LSPR	2	[79]
Ag NPs in Si QD LED	LSPR	4.5	[82]

Au NPs in QD layer	LSPR	3	[80]
Au NPs in HTL	LSPR	5	[83]
Ag NPs in HTL	LSPR	1.5	[81]
Au NPs in HTL	LSPR	2	[84]

To the best of our knowledge, QD enhancement is found to be a maximum of 5 times using most of the techniques. However, there exist other issues for QD display technology such as possible recombination of holes in ETL and vice versa leading to some fluorescence emission of the transport layers affecting the emission bandwidth. As a result, the research focus using QDs for display technology has eventually shifted towards micro LED in both academia and industry. The details of microLED display technology, and the methods of enhancement will be discussed in subsequent chapters.

1.4 Thesis Organization

In Chapter 2, a novel nanostructure fabrication technique called metal-assisted focused-ion beam nanopatterning is presented. The typical fabrication technique for the plasmonic structures is focused ion beam etching. However, due to the scattering of ions and the gaussian ion beam, the edges of the etched grooves lose their sharpness leading to a reduced electric field intensity. Since the electric field intensity is a key factor in QD enhancement, a fabrication technique is developed followed by design of

plasmonic structures for various applications. The impact of the fabrication technique over gold plasmonic dimple arrays for QD enhancement is also presented in this chapter.

In Chapter 3, a novel plasmonic nanostructure array called open-ring nanoarray is designed for demonstrating broadband enhancement and DNA sensing. The fabrication of the sensor and the experimental results are presented in this chapter. Broadband enhancement based plasmonic arrays can be potentially applied for biosensing applications.

In Chapter 4, UV plasmonic structure using Aluminum is designed for demonstrating broadband enhancement using excitation rate enhancement. Simulation and experimental results are discussed in detail about a major route of enhancement in UV plasmonics. The broadband enhancement in UV range finds potential applications in solar cells and microLED display technology.

In Chapter 5, Hyperbolic metamaterials are demonstrated to study the effect of unit cell thickness on QD enhancement. Further, a novel photonic crystal using polystyrene beads is demonstrated for large area outcoupling of high-k waves. Such a design will be well utilized for biosensing and microLED display technology.

In Chapter 6, the enhancement of carbon dot based microLED is demonstrated. Ag nanoparticles are utilized for enhancement and control of UV leakage through the emission layer. This technique will avoid the need for complex processes and additional filters required for controlling the UV excitation leakage.

A summary and conclusion will be presented in Chapter 7.

CHAPTER 2. METAL ASSISTED FOCUSED-ION BEAM NANOPATTERNING

As discussed in Chapter 1, QD enhancement using plasmonic arrays is highly dependent on electric field intensity, in other words, hot-spot intensity. The hot-spot intensity is highly dependent on fabrication technique. Focused-ion beam etching is the typical method of nanopatterning in the plasmonic community, however, facing several issues such as re-deposition during etching, gaussian ion beam, and ion scattering causing high-level defects in the nanostructures. As a result, metal-assisted focused-ion beam nanopatterning is developed and presented in this chapter.

2.1 Introduction

Nanopatterning with high precision and flexibility is highly important and challenging for the fabrication of nanophotonic devices. Focused-ion beam (FIB) has been widely used to define the device structure by direct milling of working materials without additional masks. In another way, the device can be duplicated using nanoimprint lithography with the template fabricated by FIB or other nanolithography processes. FIB fabrication technique is advantageous in its maskless process and decent spatial resolution. In addition, the milling process allows the fabrication of tapered structures which can hardly achieve by using other fabrication methods such as electron beam lithography and dry etching. However, ion beam exposure tends to induce damage on substrate morphology, material re-deposition, and surface roughness that deteriorate

the fidelity of pattern transfer resulting in optical loss and degradation of device performance. Take surface plasmonic devices for instance. The blunt-edged device structures due to low-definition pattern transfer can reduce the electric field hotspot intensity and alter the spectral response. We have recently observed that the efficiency of surface plasmon enhanced quantum dot emission in a FIB-fabricated device was deteriorated by ion beam induced surface roughness and structure deformation[85].

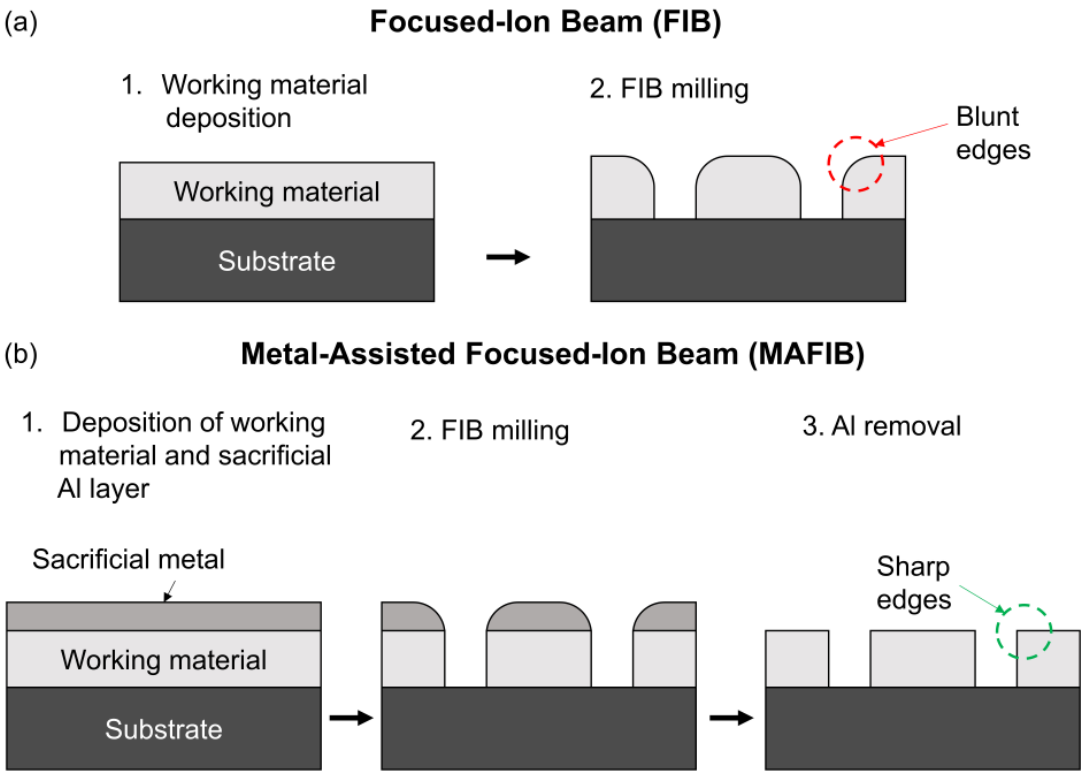

Figure 2.1. (a) Schematic of conventional focused-ion beam (FIB) patterning process: (1) deposition of working metal over the substrate and (2) direct ion beam milling resulting in formation of blunt edges. (b) Schematic of metal assisted focused-ion beam (MAFIB) patterning process: (1) deposition of working metal and sacrificial Al

layer over a substrate, (2) ion beam milling, and (3) removal of the sacrificial metal yielding

sharp pattern edges.

Metal nanostructure-based photonic devices can be fabricated via direct FIB milling of metal thin films. The conventional FIB milling process tends to yield unwanted rough surfaces and blunt milling edges as illustrated in figure 2.1(a). To overcome the issues, we present a metal-assisted focused-ion beam (MAFIB) etching process which utilizes an aluminum protective layer on the working material to achieve high fidelity nanostructure patterning in figure 2.1(b). The protective Al layer prevents the working material from exposing to low energy peripheral ion beam tails, reduces lateral milling of the substrate and thus avoids deformation of pattern edges and surface morphology. The protective aluminum layer significantly reduces the ion-beam induced damage and has advantages over other methods that use silicon oxide or aluminum oxide thin films as the protective layer[86,87] in many aspects: (1) the aluminum layer prevents the working material from exposing to the nonuniform low-energy ion beam tails leading to well-defined sidewalls; (2) the conductive aluminum surface alleviates charging effect upon FIB process and promotes pattern resolution; (3) the aluminum layer can be selectively removed by using KOH solution at room temperature leaving intact the protected working materials, such as silver, gold, silicon, and other dielectric materials for nanophotonic applications and nanoimprint template fabrication. The wet chemical etching processes for aluminum oxide removal using phosphoric acid-based etchants

and silicon oxide removal using buffer hydrofluoric acid are compatible to silicon substrates [86]; however, both etchants tend to corrode silver working material and are expected to damage silver nanopatterns. In this paper, we demonstrate the use of the MAFIB technique for high-fidelity, high-consistency patterning of sophisticated nanophotonic devices and V-shaped groove nanostructures on silver and silicon with controllable groove angles which can serve as plasmonic waveguides [88] or the templates for nanoimprint lithography.

2.2 Methods

To demonstrate direct patterning of silver nanostructures using MAFIB process, a sample with a 50 nm thick sacrificial Al layer and a 400 nm thick Ag thin film were deposited on a silicon substrate through a 10 nm thick titanium adhesive layer as illustrated in figure 2.1(b). FIB milling was carried out using FEI Quanta 3D FEG. Gallium ion beam doses and currents were adjusted to achieve required milling depth. A particular line patterning process was performed using an ion beam current of 300 pA and a dose of 1000 nC cm−1 at a magnification of 3100× to create a 100 nm wide and 200 nm deep V-shaped groove. The process is accomplished by removing the sacrificial Al layer in a 0.9M KOH solution at room temperature (∼10 nm s−1). The KOH etchant was chosen as it does not attack silicon or glass substrates and the working metals, such as silver and gold, at room temperature. Similar processes were applied to fabricate silicon nanoimprint templates and nanophotonic devices with silver

open-ring nanostructure array. Process details for the specific applications are discussed in section 2.3.

2.3 Results and Discussions

2.3.1 Dual Line Patterns

To evaluate the precision of nanopatterning, dual line patterns with 100 nm line width and various inter-line distances as indicated in the schematics in figure 2.2 were fabricated using both conventional and MAFIB processes. As shown in the scanning electron microscopic (SEM) images in figure 2.2, a drastic improvement in surface smoothness is observed in between and around the milling lines fabricated by MAFIB process in comparison to those by FIB process as indicated by red (FIB) and green (MAFIB) circles. In the dual line pattern with 200 nm inter-line distance, conventional FIB process fails to produce a continuous, uniform structure between the milling lines, whereas MAFIB process gives consistently sharp structures. As the inter-line distance reduces to 100 nm, the structure in between the milling lines was almost eroded away under conventional FIB process, while the pattern formed by MAFIB preserves the residual structure between the etched lines although it becomes too narrow to stand straight as depicted in the inset of figure 2.2(c). As the ions strike the material surface, secondary ions scattering is likely to cause the blunt structure edges as well as re-deposition of the etched metal. In this scenario, the working metal acts as a barrier for secondary ions and minimizes their damage to the interface of working and sacrificial metal. The redeposited material does not reach the surface of the working material, and

instead only a small amount of it piles up and forms a small bump over the edge which can be resolved by the SEM images. Furthermore, because the ion beam passes through several apertures before being incident to the working material, the ion beam profile becomes non-uniform from which the extended ion beam tails contribute to the surface damage. The MAFIB process overcomes all the issues and is proved to yield high-precision nanopatterning with consistently fine edges on the milling structures which can also be observed in the cross-sectional SEM images in figure 2.2(d).

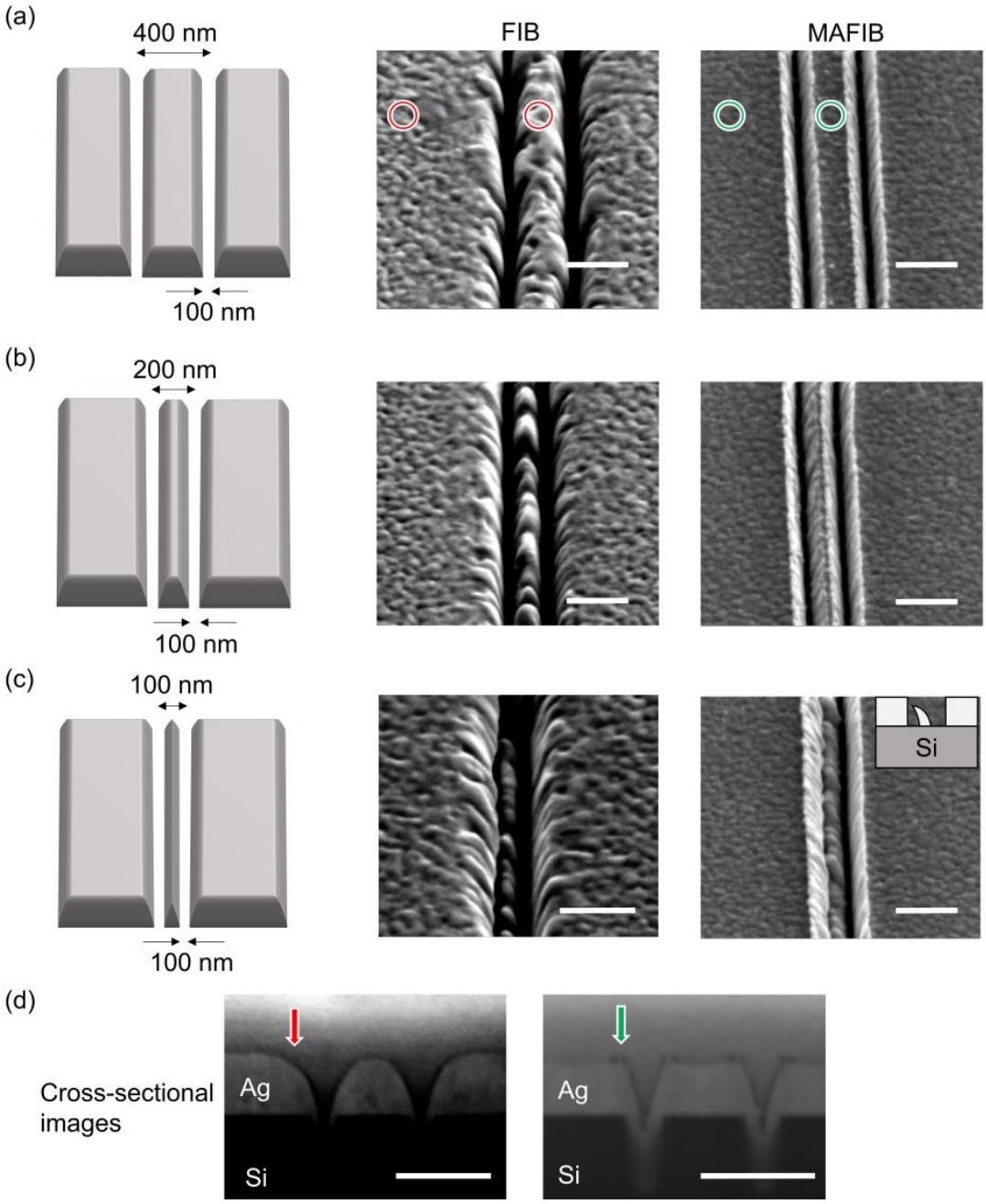

Figure 2.2. SEM images of dual line patterns fabricated by conventional FIB and MAFIB milling processes with 100 nm line width and various center-to-center inter-line distances (a) 400 nm, (b) 200 nm, and (c) 100 nm. Red and green circles indicate

the difference in surface roughness created by FIB and MAFIB processes. Inset depicts the cross-sectional structure. (d) Cross-sectional SEM images of etched lines with an inter-line distance of 400 nm and each line width of 100 nm. Arrows indicate the blunt and sharp edges created by conventional FIB and MAFIB processes, respectively. Scale bars indicate 500 nm for all images.

2.3.2 Templates for Nanoimprint Lithography

The capability of high-fidelity patterning makes MAFIB a competent technique for high-precision fabrication of nanoimprint templates. Precision aside, the technique enables direct formation of V-shaped grooves which has potential to be utilized for grooves or wedges-based surface plasmon devices to implement plasmon waveguides, fluorescence enhancement, biosensing and THz technology[89 - 94]. Here we demonstrate the use of the MAFIB process to fabricate silicon nanoimprint templates for transferring wedge grating patterns with controllable angles as in the schematic shown in figure 2.3(a). A 55 nm thick aluminum was deposited over a silicon wafer to serve as the sacrificial layer without additional adhesion layer. FIB milling at 300 pA with a dose of 900 nC cm^{-1} followed by aluminum removal was performed to obtain v-shaped groove structures on silicon. The silicon template was treated with perfloruosilane by evaporation to promote mold release. Polyurethane-based UV curable polymer (300 cps), was then coated over the silicon template and contacted to a polyethylene terephthalate (PET) sheet substrate. After exposure under 365 nm, 175$mWcm^{-2}$ UV light for 3 min, the PET sheet along with the imprinted polymer

structure was demolded from the template along the groove orientation which is essential to achieve high-quality pattern transfer. Figure 2.3(b) is the top-view SEM image of the groove array in a silicon template. The cross-sectional SEM image in the inset shows that the groove structures were well defined to reveal fine edges. The wedge grating structures were successfully transferred to the UV curable polymer on a PET substrate as shown in figure 2.3(c). The wedges were not as pointed as those of the grooves on the silicon template which may be attributed to the incomplete filling of the viscous UV curable polymer at the template cavities.

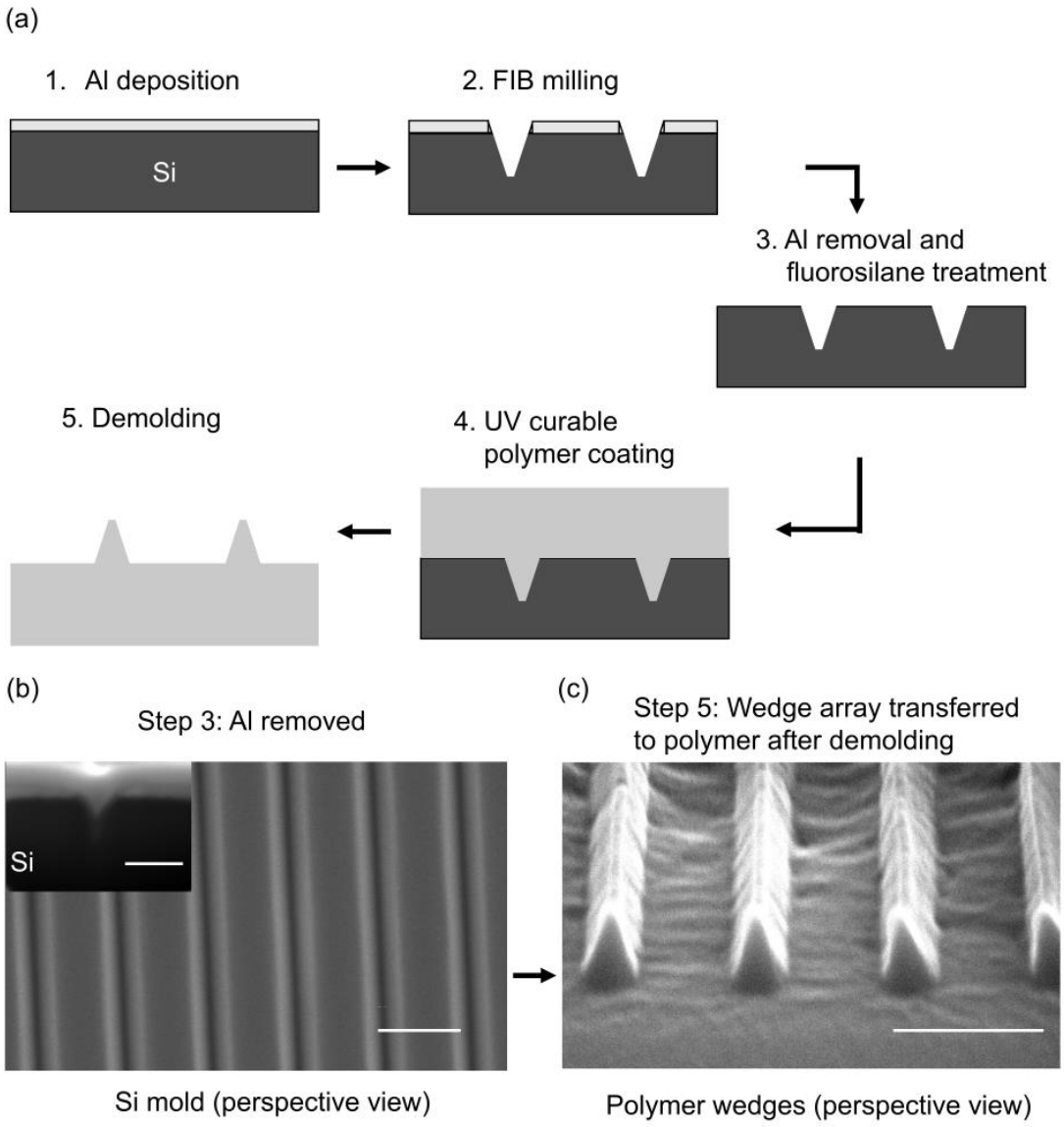

Figure 2.3. (a) Template fabrication process. (b) Top view SEM image of a Si template (Inset: cross-sectional image). (c) SEM image of wedge array transferred on UV curable polymer. Scale bar: 500 nm.

V-shaped grooves are typically fabricated on crystalline substrates, e.g., silicon wafers, through lithography pattering of an etching mask followed by anisotropic etching. The

resulting groove angle restricted by the crystal structure of the silicon wafer. Moreover, the pattern layout needs to be designed properly according to the crystal orientation. MAFIB allows direct formation of the V-shaped grooves with controllable groove angles, by unlimited layout design, and on various substrate materials.

Figure 2.4(a) shows multiple v-shaped grooves of various groove angles fabricated on a silicon substrate. Under the protection of the aluminum layer, the silicon groove structure with fine edges and valleys were easily achieved through FIB milling. The groove angle and depth were adjusted by controlling the combination of beam current and dose. The increase of beam current broadens the milling spot size whereas the rise of ion dose increases milling depth. The flexibility cannot be realized by using conventional anisotropic etching or dry etching processes. Figure 2.4(b) shows two silicon groove arrays with 400 and 500 nm array periods. The sharp edges on the groove arrays make the structures suitable for the fabrication of nanophotonic devices such as plasmonic waveguides.

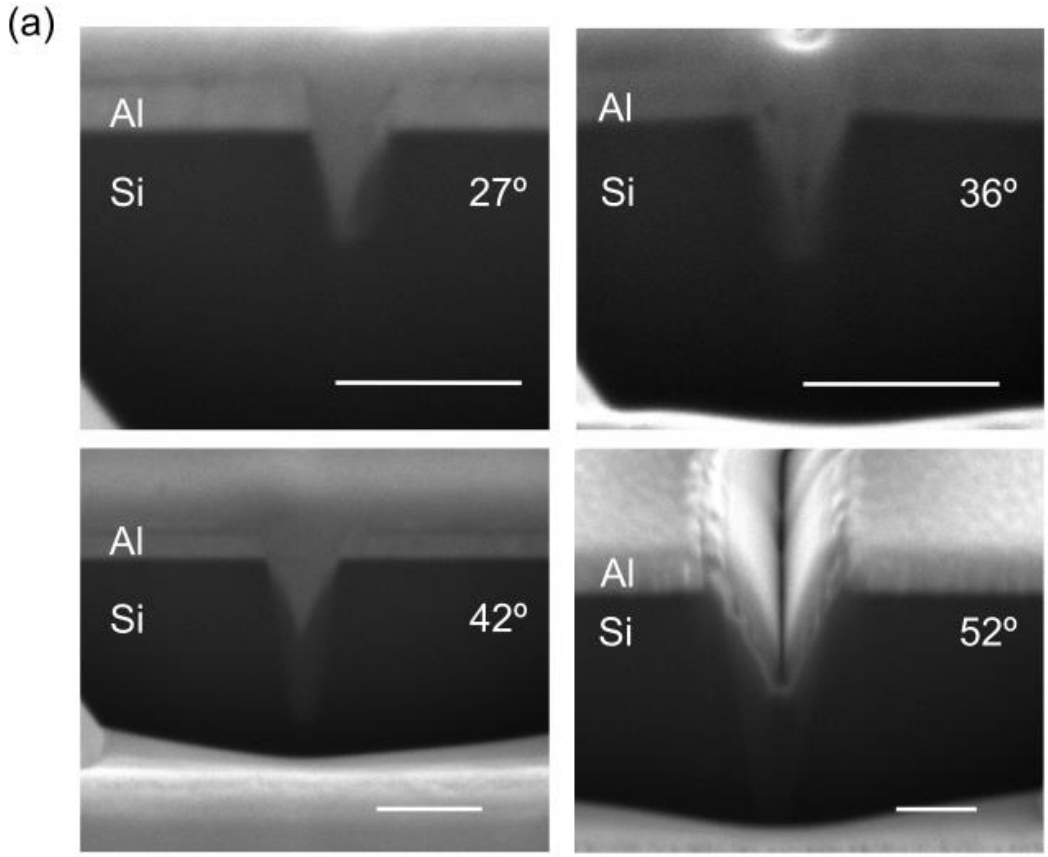

(b) Si molds with two different V-groove array dimensions

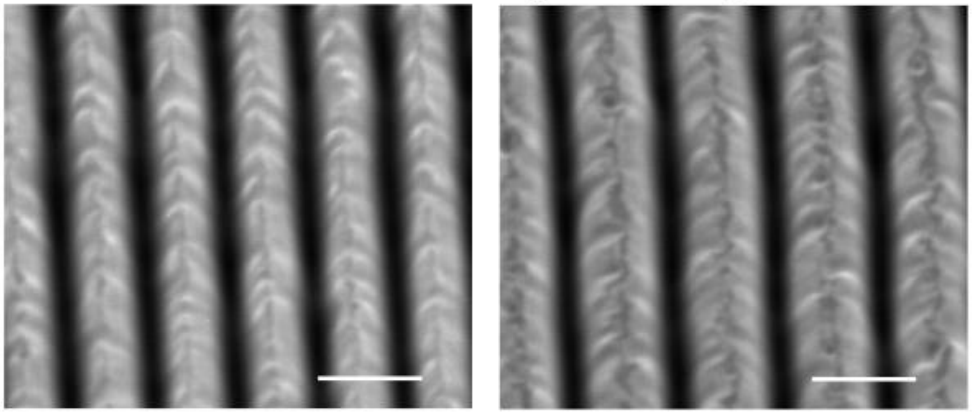

Figure 2.4. (a) SEM images of silicon groove templates before Al removal with various groove angles—27°, 36°, 42°, and 52°. (b) V-groove array silicon templates with two different periods (400 and 500 nm). Scale bar: 500 nm.

2.3.3 Two-Dimensional Plasmonic Arrays

The MAFIB process allows high-fidelity patterning of complex nanostructures, such as the silver open-ring nanostructure array illustrated in figure 2.5(a). The silver nanostructure array was designed to achieve maximum absorption of broadband non-polarized visible light. Each unit cell has a 100 nm wide open-ring structure engraved 100 nm deep into a 200 nm thick silver thin film. The nanoscale curvature and closely packed feature in each ring structure can be hardly realized by using the conventional FIB method. The SEM image of the resulting structure in figure 2.5(b) shows that the details of the open-ring patterns were not present due to the deformation of the structure during the milling process. On the other hand, the open-ring structures with well-defined boundaries were obtained with high reproducibility through the MAFIB technique as shown in figure 2.5(c). The FIB milling process was carried out using a current of 300 pA and a dose of 600 nC cm^{-1}. The silver thin film was protected by a 55 nm thick aluminum sacrificial layer during the milling process. The improvement in surface smoothness and fine edges is clearly observed.

The absorption spectra of the open-ring nanostructure array devices fabricated by conventional FIB and MAFIB were measured to evaluate the effect of process on their optical property. It is observed that the device made by MAFIB process exhibits higher

absorption over the entire visible range with a maximum increase of 30% at 450 nm wavelength as shown in figure 2.6. The additional protective layer results in precise structure formation with sharp pattern edges and drastically minimizes surface roughness. These two features are critical to the performance of surface plasmon resonance based devices as they can distort the Q-factor and absorbance of optical spectra. The absorption property can be utilized to implement surface plasmon-enhanced fluorescence that will find applications in biosensing and fluorescence imaging.

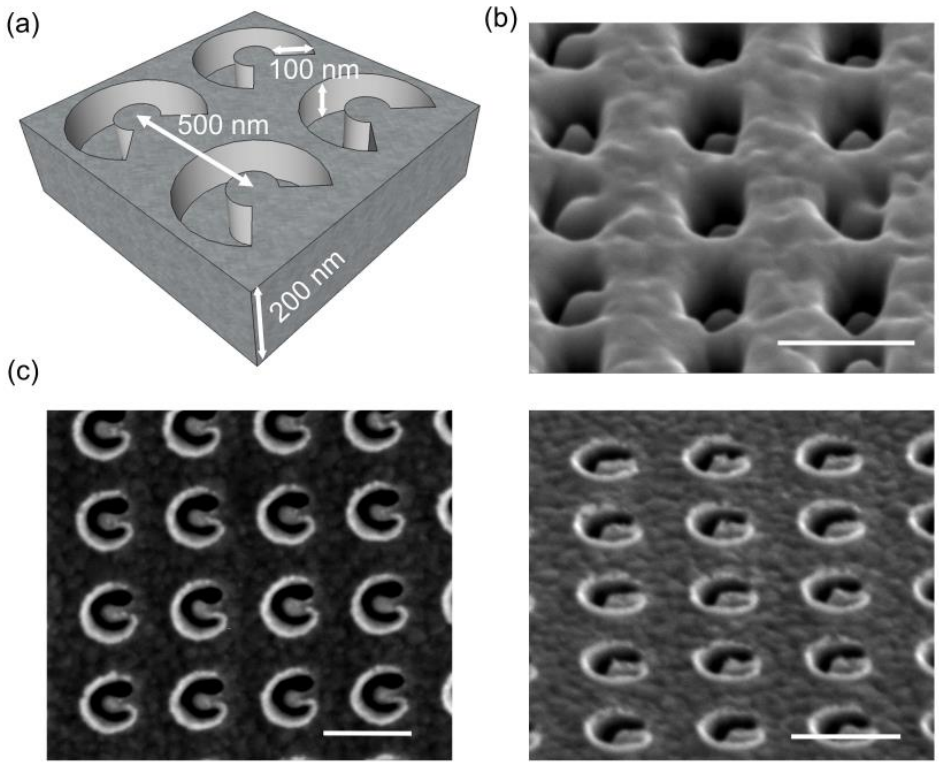

Figure 2.5. (a) Schematic of an open-ring nanostructure array with a 500 nm period, 100 nm depth, and 200 nm thickness. SEM images of the device fabricated by using conventional FIB process (b), and MAFIB process (c). Scale bar: 500 nm.

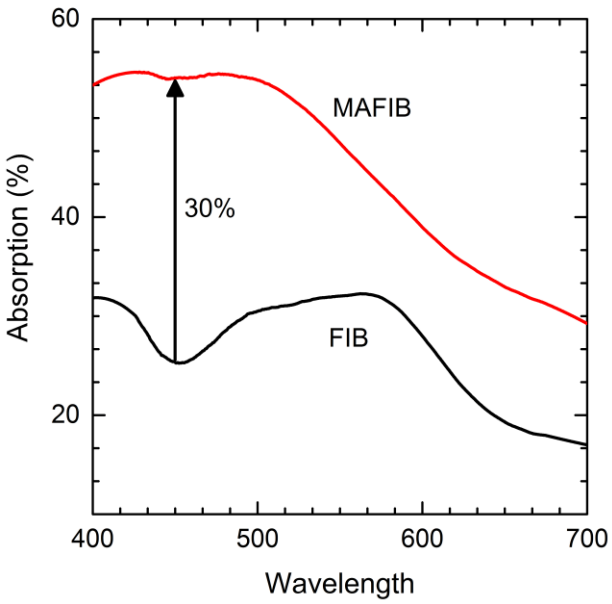

Figure 2.6. Measured nonpolarized absorption spectra of the open-ring nanostructure array device fabricated by using conventional FIB and MAFIB processes.

2.3.4 QD Enhancement on Gold Dimple Arrays

Dimple arrays are partially etched holes into a 200 nm thick Au film. As shown in Figure 2.7, Au film of 500 nm period (distance between two dimples) is made with 200 nm dimple diameter, etched using MAFIB technique. The SEM images show the difference in sharpness of edges and the simulated electric field profile shows the increase in field intensity is more than twice that of the one made using FIB. The

simulation is done using FDTD method and more details about this will be discussed in Chapter 3. CdSe/ZnS QDs dispersed in polymer is spin-coated over the substrate and carried out for photoluminescence measurement. The enhancement factor of QDs which is the ratio over the plasmonic substrate and glass is measured using spectrofluorometer. The EF achieved over dimple array made use MAFIB is found to be ~40 times, while the one with FIB is found to be ~19 times. This ratio of enhancement by improving the fabrication technique agrees well with the simulation.

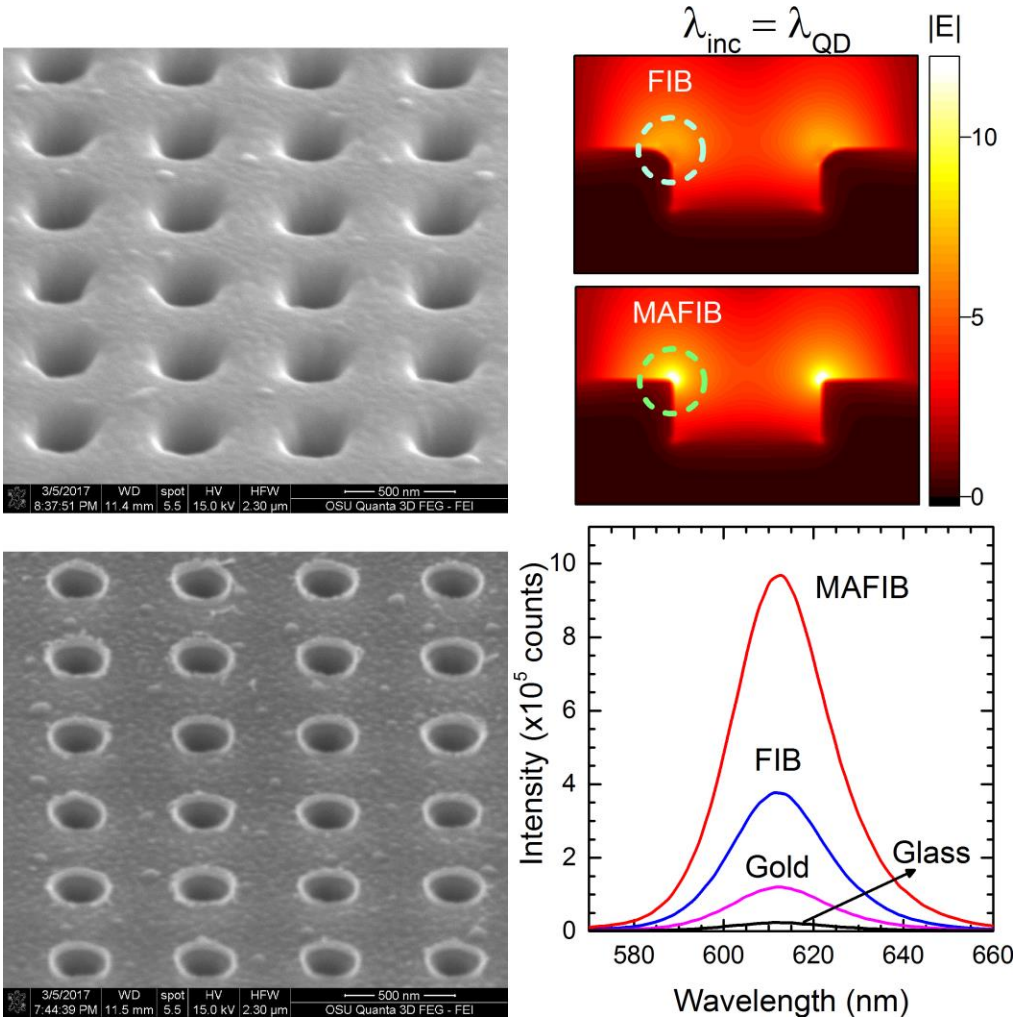

Figure 2.7. SEM images of Au dimple arrays fabricated using (a) FIB and (b) MAFIB. (c) FDTD simulation of electric field intensity with sharp and blunt edges. (d) Photoluminescence spectra of QDs over dimple arrays made using FIB and MAFIB, Au and glass.

2.4 Summary

In conclusion, we demonstrated a MAFIB process to achieve high-fidelity, high-reproducibility nanostructure patterning. The technique takes advantage of the additional aluminum layer to protect working materials from ion-induced damage, re-deposition of material and, therefore, results in high-precise nanopatterning and smooth surfaces after aluminum removal. Aside from the drastic improvement in the patterning of nanostructures, the MAFIB process is compatible with various substrate materials. This technique is expected to benefit the fabrication of nanoimprint templates and the development of nanophotonic devices. In the end, we demonstrate the effect of fabrication technique on QD enhancement using Au dimple arrays. A 40-fold enhancement is found on MAFIB based dimple array, and a 19-fold enhancement is observed on FIB based dimple array.

CHAPTER 3. PLASMONIC OPEN-RING NANOARRAYS FOR BROADBAND FLUORESCENCE ENHACEMENT AND ULTRASENSITIVE DNA DETECTION

In this chapter, a short overview of mechanisms is discussed followed by the design of novel open-ring nanostructures for broadband fluorescence enhancement and ultrasensitive DNA sensing.

3.1 Introduction

Fluorescence-based detection is the most widely adopted analytical technique in biotechnology and medical diagnostics due to its low detection limit and high reliability. A variety of techniques have been developed to enhance fluorescence responses based on plasmonic structures aiming to further improve the sensitivity and the limit of fluorescence detection. The improvement can be achieved by incorporating fluorescence enhancement induced by the surface plasmonic resonance on metal nanostructures[95,96], the fluorescence quenching using metal nanoparticles[97-99], and the combination of both[100,101] to increase the signal-to-noise ratio for the detection. These techniques take advantage of the interactions between the surface plasmons on the metal surface and quantum emitters, such as quantum dots (QDs) and organic fluorophores. The fluorescence enhancement becomes stronger with the decrease of the separation distance between the quantum emitter and the metal surface until the nonradiative energy transfer to the metal nanostructure begins to dominate at

short distances, leading to fluorescence quenching[102]. A maximum fluorescence enhancement occurs at a separation distance of about 5−10 nm. The enhanced fluorescence can be attributed to the increased excitation rate or the enhanced radiative decay rate (emission rate) of the quantum emitter[103-106] which are associated with the spectral overlap between the surface plasmon resonance and the absorption or emission spectrum of the quantum emitters. In a system where the surface plasmon resonance of the metal nanostructure overlaps the absorption of the quantum emitter, the emitter tends to obtain an enhanced excitation rate. In this case, the metal nanostructure primarily absorbs the incident excitation and produces surface plasmon polaritons. The quantum emitter can be further excited through Förster resonance energy transfer (FRET) by the intense local field created by surface plasmons. The excitation rate increases with the decrease of the metal−emitter distance. On the other hand, the overlap between the surface plasmon resonance and the emitter's emission spectrum can either enhance or quench the fluorescence depending on the separation distance. If the emitter is within a few nanometers of the plasmon, the emission will be quenched through FRET by exciting higher order modes in the plasmon which do not radiate to the far-field[107]. At a distance outside the FRET regime, the plasmon-induced strong local field raises the number of photon modes accessible for the quantum emitter to emit, i.e., the local density of optical states (LDOS), and, therefore, increases the radiative emission rate of the quantum emitter compared to that in the free space. Such emission enhancement is known as the Purcell effect. Metal nanostructures, such as periodic metal hole nanoarrays or dimple nanoarrays, have been employed to

produce surface plasmon resonance for fluorescence enhancement by controlling their periodicity and dimension[108,109]. The resonance peaks of these structures tend to be narrow and are arranged to enhance the quantum emitter of a selective wavelength. The plasmonic nanostructures with multiple resonance peaks allow a broad spectral overlap with the emission wavelengths of different quantum emitters to result in a multiwavelength emission enhancement. In the case of organic fluorophores which have a considerable overlap of absorption and emission spectra in the visible range, the broadband surface plasmon resonance permits the concurrence of both enhanced excitation and emission leading to a strong fluorescence enhancement.

In this paper, we demonstrate an open-ring nanoarray (ORA) engraved on a silver surface to support multiple surface plasmon resonance peaks covering almost the entire visible spectral range to achieve strong, broadband fluorescence enhancement for ultrasensitive DNA sensing. It is worthwhile to emphasize that a complementary open-ring array typically refers to a structure with an array of the open-ring structure cut through the metal thin film. Differently, the ORA presented here is the structure partially etched onto a silver thin film which exhibits no light transmission through the structure and no coupling between both sides of metal interfaces. The absorption spectrum is contributed by the surface plasmon resonances on the top side of the metal surface exposed to incident light. The ORA structure was found to be advantageous in at least three aspects. First, it produces multiple resonance modes in the visible spectral range that allow broadband and strong enhancement of fluorescence through enhanced emission and enhanced excitation rate. Second, the engraved open-ring structure has a

longer perimeter than circular holes or dimples; the lengthy sharp edges may increase the density of electric-field hot-spots that further enhance fluorescence intensity. Third, the resonance spectrum of the ORA provides efficient energy transfer between emitter and surface plasmons that promotes the quenching efficiency of the fluorophores in close proximity to the metal surface[110]. The improved fluorescence quenching reduces the background fluorescence signals and amplifies the signal-to-noise ratio for biosensing. To clarify the emission and excitation enhancement properties of ORA, we experimentally and theoretically investigate the enhancement of multicolor QDs on ORA with the same period and analyzed enhancement of QDs on the ORA under variable excitation wavelengths. Silver dimple nanoarrays with different periods were characterized for comparison. On the basis of the studies, we demonstrate ultrasensitive DNA detection using ORA-enabled molecular beacons.

3.2 Materials and Methods

3.2.1 Fabrication of Silver Open-Ring Nanoarrays and Dimple Nanoarrays

Silver open-ring nanoarrays (ORAs) and dimple arrays were fabricated using a metal-assisted focused-ion beam (MAFIB) nanopatterning[111] technique to achieve high-definition metal nanostructures as detailed in the previous chapter and Figure 3.1. In brief, a 200-nm-thick silver layer was deposited on a silicon substrate with a 5-nm-thick titanium adhesive layer using physical vapor deposition. A 50-nm-thick aluminum layer was deposited to serve as a sacrificial metal. FIB milling was

performed using an electron microscope (Dual-beam SEM, FEI) to engrave 100-nm-deep nanostructures into the silver layer through the Al sacrificial layer. The Al layer was then removed in 0.9 M KOH solution.

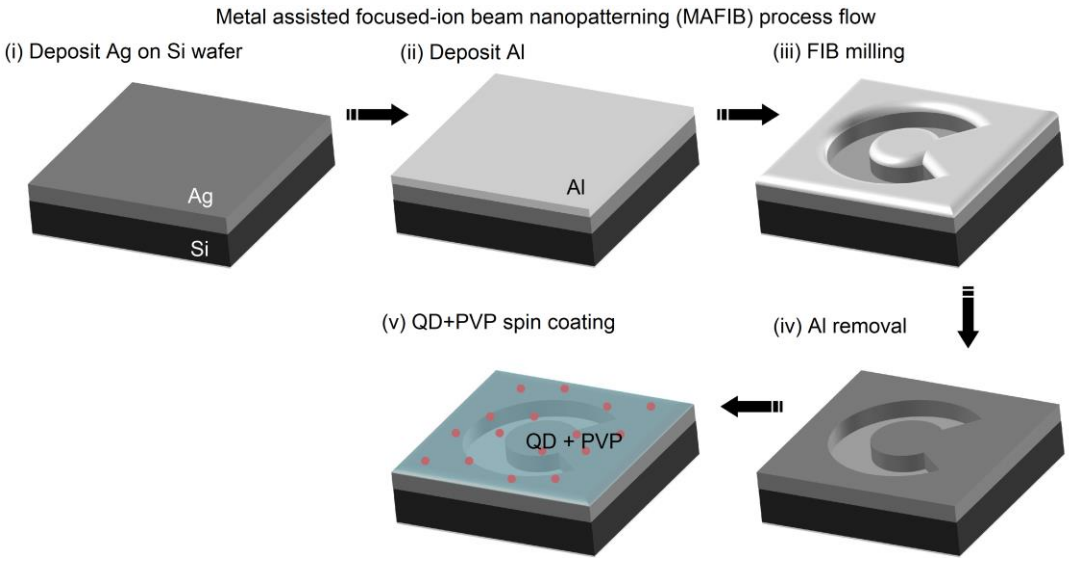

Figure 3.1. Schematic of metal-assisted focused-ion beam nanopatterning: (i) deposition of working metal on substrate, (ii) deposition of sacrificial metal, (iii) ion beam milling, and (iv) removal of sacrificial metal. (v) spin-coating of QD (dispersed in PVP) solution to form a thin layer on the nanostructure.

3.2.2 Characterization of QD Emission Enhancement

To evaluate the enhancement of QD emission on the nanostructured substrates, we spin-coated a QD/polymer solution on the nanostructured substrates and glass substrates to form a 30-nm-thick layer after drying. The QD/polymer mixture was prepared by dispersing colloidal CdSe/ZnS QDs (Ocean Nanotech) in 0.9 mg/mL

methanolic poly(vinylpyrrolidone) (PVP-10) solution. QDs with 610 and 540 nm emission peaks were chosen for tests. Both QDs have an intrinsic quantum efficiency of 65%. Photoluminescence (PL) spectra measurements were carried out on an inverted microscope (Olympus IX73) integrated with a fluorospectrometer (Horiba Fluoromax-4). The PL excitation was a continuous-wave light source with a power density measured to be about 70 mW/cm2 after the 60× microscope objective (N.A. = 0.9) that was low enough to prevent saturation of the QD PL. The fluorescent images were captured by a color CCD camera (Lumenera Infinity3-3UR) on the inverted microscope.

3.2.3 Finite-Difference Time-Domain (FDTD) Simulations

Theoretical enhancement factors of the quantum emitters, the electric-field profiles on ORAs and dimple nanoarrays, and their far-field emission profiles were calculated using a commercial solver FDTD Solutions (Lumerical, Vancouver, Canada). The simulation setup and schematics are discussed in Figure 3.2.

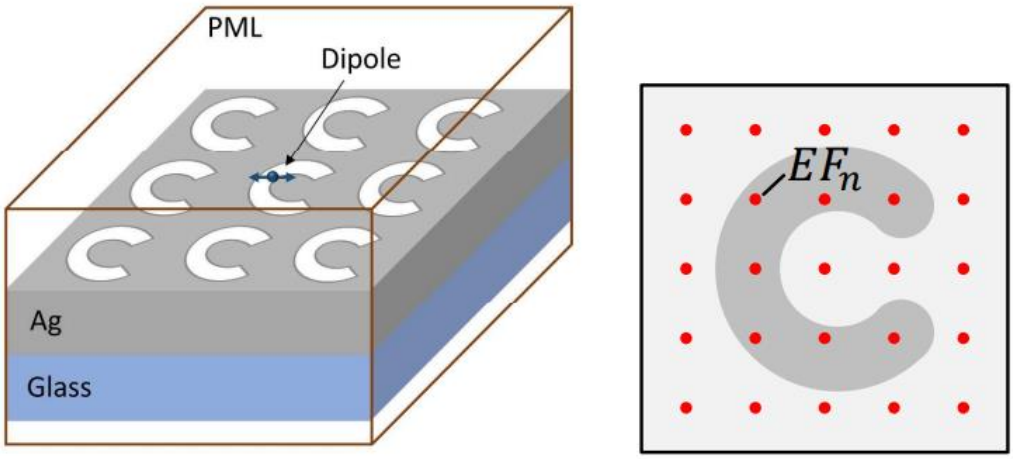

Figure 3.2. Schematic of FDTD simulation model with perfectly matched layer (PML) boundary conditions and an array of nanostructures with a dipole emitter placed 10-nm above the Ag surface in one of the unit cells at the center. The Ag and glass layers are 200 nm and 1000 nm thick, respectively. The ORA has a 340 nm period, 100 nm depth and 100 nm width and the dimple nanoarray with two different periods (280 nm and 350 nm) and 100 nm depth. An optional plane-wave light source is placed 1000 nm above the Ag surface. The simulation can be performed without the external light source if the wavelength of the light source does not interact with the nanostructure which would occur for a UV excitation. The enhancement factor of each point EF_n in a unit cell is calculated by averaging the EF of different polarizations, i.e.,

$$EF_n = \frac{1}{3}\left(EF_{nx} + EF_{ny} + EF_{nz}\right)$$

The total average enhancement factor is calculated by averaging all the EFn at different positions in the unit cell, i.e., $\langle EF \rangle = \frac{1}{n}\sum_{All\ n} EF_n$.

3.2.4 Fabrication of Microfluidic Flow Cells

The ORA substrate was integrated with a 1.2 μL-sized microfluidic flow cell to perform the DNA sensing assay. The microfluidic channel was built between the ORA substrate and a glass slide separated by a 370 μm-thick spacer formed by a polyimide double-sided adhesive film cut into a microchannel pattern. Polyimide microtubings (140 μm outer diameter) were connected to both ends of the channel and sealed with polyurethane-based UV curable polymer. The schematics are presented in Figure 3.3.

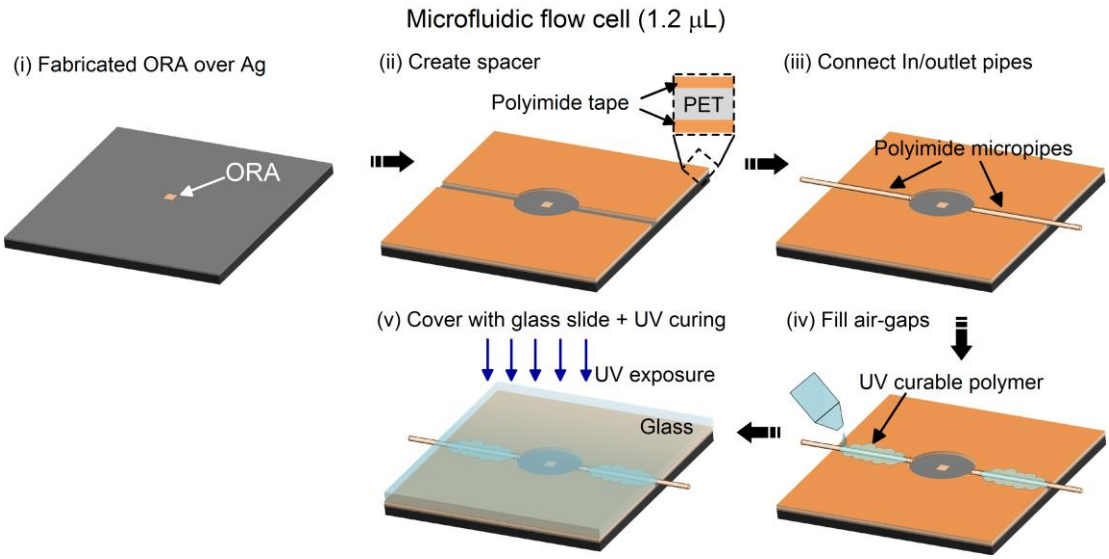

Figure 3.3. Microfluidic flow cell (1.2 μL volume) preparation flow: (i) fabricate ORA metal-assisted focused ion beam milling on a 200-nm thick silver coated silicon substrate using, (ii) create a flow channel defined by spacer layers using polyimide/PET/polyimide thin film (inset), (iii) connect inlet and outlet polyimide micropipes, (iv) fill the air-gaps with UV curable polymer so as to avoid leakage or

bubble formation, and (v) encapsulate the structure with a cover glass followed by curing the polymer with 365- nm UV light exposure for 10 minutes. The resulting chip will then be connected to solutions and a syringe pump through microtubings for the test.

3.2.5 DNA Detection Assay

The DNA molecular beacon (MB) probe was a 32-base oligonucleotide with a disulfide linker-modified 5′ terminus and fluorescent fluorescein (5-FAM)- labeled 3′ terminus. Target and nontarget single-stranded DNA (ssDNA) molecules were used to analyze the sensitivity and selectivity of the sensor. All the DNA oligonucleotides were purchased from LGC Biosearch Technologies (Novato, CA). The sequences of the oligonucleotides are as follows: MB probe: 5′-SS-C6-GCGCGTCAACATCAGTCTGATAAGCTACGCGC- FAM-3′; target DNA: 5′-TAGCTTATCAGACTGATGTTGA-3′; nontarget DNA: 5′-TTAATGCTAATCGTGATAGGGGT-3′.

Immobilization of DNA MB probes on the silver ORA substrate started with the reduction of the disulfide linker on the MB probes using tris(2-carboxyethyl)phosphine hydrochloride (TCEP) (Sigma-Aldrich). The freshly prepared silver ORA substrates were exposed for 45 min to a solution mixture containing 1 M monopotassium phosphate, 0.01 mM 6- mercapto-1-hexanol, and 2 μM MB probes. The flow chamber was then rinsed thoroughly with 1X PBS buffer. The MB modified substrates were further annealed at 65 °C to allow the MB to form a hairpin configuration. DNA

detection was performed by passing analyte samples of various target DNA concentrations ranging from 100 fM to 1 μM, each with 40 min hybridization. A hybridization time of at least 20 min was tested to yield a comparable result. This process was repeated using nontarget DNA to verify the sensing selectivity. DNA sensing was performed using an LED excitation light source (X-Cite 120 LED) coupled to the inverted microscope. To minimize he photobleaching effect, the exposure time was limited to 10 s. The fluorescence detection signals were analyzed with a monochromatic sCMOS camera (Hamamatsu Flash 4.0 LT). The fluorescent images were captured with a color CCD camera (Lumenera Infinity3-3UR).

3.3 Results and Discussion

Figure 3.4(a) and 1(b) shows the scanning electron microscopic (SEM) images of a Ag ORA with 340 nm period, 100 nm depth, and 100 nm width and, for comparison, a Ag dimple nanoarray with 280 nm period and 100 nm depth. The absorption spectra in Figure 3.4(c) show that the ORA supports multiple resonant peaks covering the emission spectra of both green and red QDs at 540 and 610 nm wavelengths, respectively. On the contrary, the dimple nanoarrays provide a single resonant mode determined by the periodicity of the structure. Figure 3.4(d) shows that the dimple nanoarrays of 280 nm period and 350 nm period create narrowband resonance peaks that selectively match one of the red and green QD emissions.

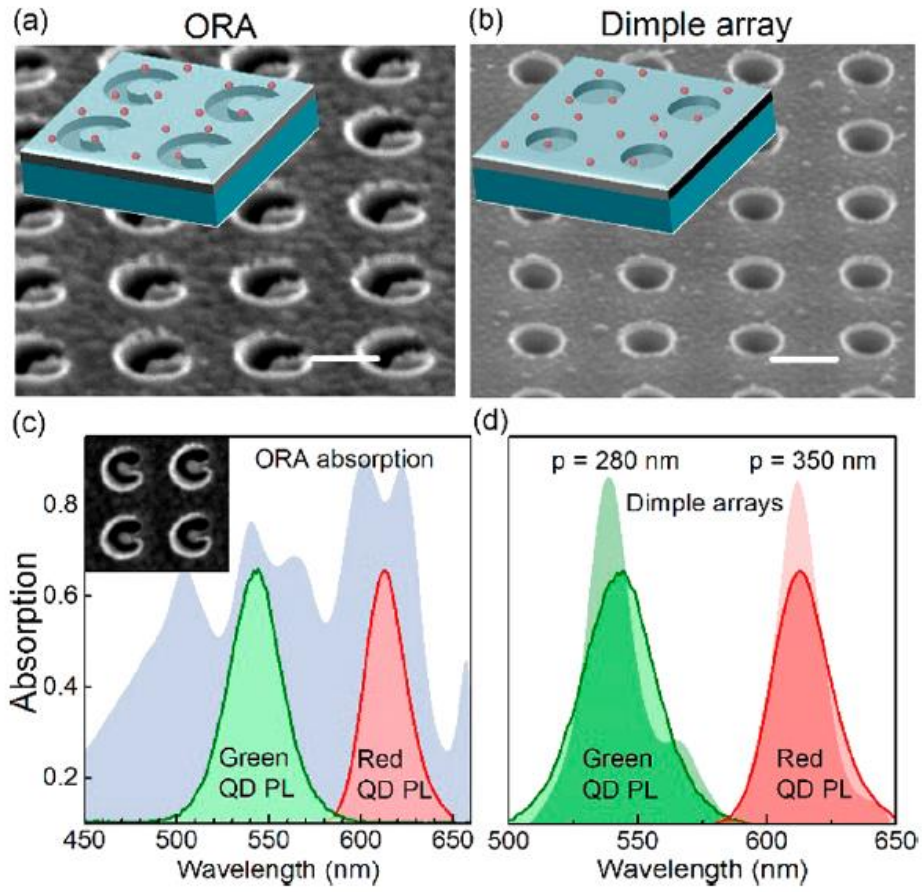

Figure 3.4. Schematics and SEM images of the (a) engraved Ag open-ring nanoarray (ORA) and (b) Ag dimple nanoarray (scale bars: 200 nm). The structures were spin-coated with a 30-nm-thick poly- (vinylpyrrolidone) (PVP) layer embedded with CdSe/ZnS QDs to evaluate fluorescence enhancement. The combined QD photoluminescence (PL) spectra and absorption spectra of (c) the ORA with a 340 nm period, 100 nm depth, and 100 nm width and (d) the dimple nanoarray with two different periods (280 and 350 nm) and 100 nm depth.

The PL measurements summarized in Figure 3.5 compare the enhancement of red QDs (610 nm emission) and green QDs (540 nm emission) on ORAs and dimple nanoarrays. We quantified the PL enhancement by using an enhancement factor (EF) defined as the ratio of the QD emission peak on the metal nanostructures to that on the glass substrate. All the QD PL characterizations were acquired under continuous wave excitations at a 380 nm wavelength and a 70 mW/cm2 power density. Figure 3.5(a) shows that the red and green QDs on the same 340 nm period ORA exhibit strong EFs of ∼40 and ∼30, respectively. However, the 350 nm period dimple nanoarray selectively enhances red QDs yielding an EF ∼ 35 but has an insignificant effect on green QDs with a small EF ∼ 1.4 (Figure 3.5(b)). The same wavelength-selective enhancement was observed on the 280 nm period dimple array in which a large EF ∼ 30 was observed for green QDs and a weak EF ∼ 3 for red QDs as shown in Figure 3.5(c). The corresponding fluorescence images summarized in Figure 3.5(d) demonstrate the broadband enhancement on ORAs and wavelength-selective enhancement on dimple arrays. The UV excitation was not absorbed by ORAs efficiently, leaving the enhancements primarily contributed to enhanced emission due to the spectral overlap between QD emission and substrate absorption. The emission enhancement can be illustrated by the route 1 interaction in the diagram in Figure 3.5(f) and 3.5(g). It is worth noting that the QD PL intensities on the non-resonant Ag dimple arrays show a reduced fluorescence intensity compared with that on the plane Ag surfaces. The result can be attributed to the large-angle scattering of QD emission from the metal nanostructure.

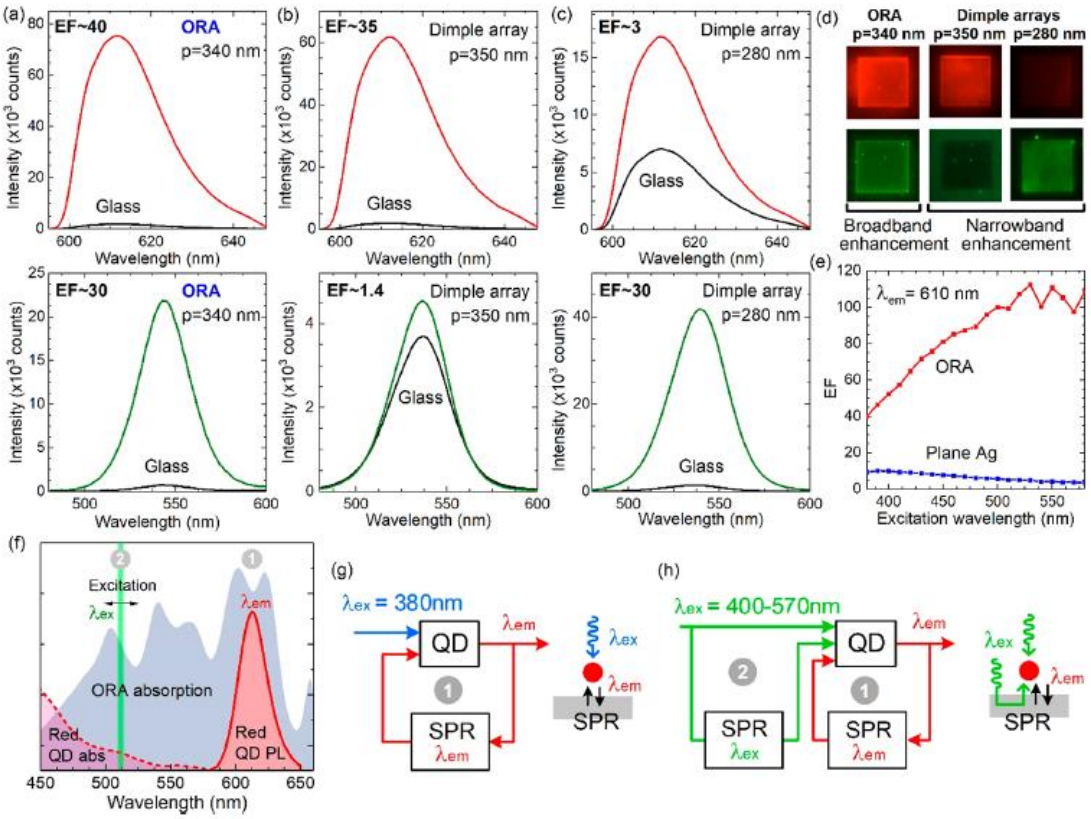

Figure 3.5. PL spectra of red QDs (610 nm emission) and green QDs (540 nm emission) on (a) a 340 nm period ORA substrate, (b) a 350 nm period dimple nanoarray, and (c) a 280 nm period dimple nanoarray substrate. All QDs were excited by a 380 nm continuous-wave light source. Enhancement factor (EF) is defined by the ratio of the peak PL intensity on the nanostructures (ORAs or dimple nanoarrays) to that on the glass. (d) Fluorescence images of the enhanced QD emission on the ORAs and dimple nanoarrays in the square areas. Outside the squares are plane Ag surfaces. (e) Enhancement factors of the red QDs on ORA and plane Ag substrates as functions of excitation wavelength. (f) The combined emission and absorption spectra of red QDs, and absorption spectra of ORAs. The level of QD absorption spectrum is

exaggerated. (g) Diagram represents the interaction between the UV-excited QDs and surface plasmons at the emission wavelength λ_{em} that results in emission enhancement (indicated by route 1). ORAs do not absorb UV light efficiently. (h) Diagram represents the QD−surface plasmon interactions under a visible-light excitation. Apart from the route 1 emission enhancement, the visible-light also creates surface plasmons on ORAs that enhance the excitation of QDs at the excitation wavelength λ_{ex} (indicated by route 2).

Figure 3.5(e) shows that the EF of red QDs on ORAs rises with the increased excitation wavelength and even exceeds 110 while that on plane Ag decreases slightly. It is known that no matter what substrate the QDs are placed on for enhancement, the intensity of QD emission decreases with the increase of excitation wavelength due to the reduced absorption of QDs at longer wavelengths. However, the EF of the QDs on ORA, which considers the ratio of the emission intensity on the plasmonic substrate to that on the glass, can vary with excitation wavelength due to the enhancement of QD excitation. As illustrated by the diagram in Figure 3.5(h), apart from the emission enhancement contributed by the route 1 QD−plasmon interaction at the emission wavelength, the visible-light excitation is absorbed by the ORA through surface plasmons that creates strong local fields and enhances the excitation of QDs. The plane silver substrate shows a different trend of wavelength-dependent EF because of the poor and slightly decreased absorption as wavelength increases in the visible range.

Figure 3.6(a−c) summarizes the position-dependent EF of a single dipole emitter (540 or 610 nm emission wavelengths) placed at 10 nm above the metal surface across the unit cell of an ORA and a dimple nanoarray. The EF value at each position was calculated by averaging the results of three dipole emitters polarized along x, y, and z directions. We obtain ⟨EF⟩ by averaging the EFs over the entire unit cell. To explicate the relationship between EF and the surface plasmon resonance on the nanostructures, we resolve the representative electric-field profiles on the ORA and dimple nanoarray induced by a vertically oriented dipole emitter positioned at the center of the unit cell as shown in Figure 3.6(d−f). Overall, the EF profiles indicate that the edges of the nanostructures contribute most to the enhancement due to the electric field hot-spots around the sharp geometries. The ORA exhibits different distributions of strong EF on the structure for green and red QDs but supports comparably large EFs for both emission wavelengths. The EF profiles match the corresponding distributions of electric-field hot-spots induced by the dipole emitters, indicating that the multi-resonance modes on ORAs enable coupling of multicolor QDs and thus support the broadband enhancement. On the contrary, the dimple nanoarray shows a narrowband enhancement. We can only observe the strong electric-field hot-spots and large EF for a specific QD emission wavelength. Despite the qualitative agreement between the simulation and experimental results, all the simulated ⟨EF⟩ are smaller than the measured values. The difference may be attributed to the presence of mutual enhancement among QDs associated with a plasmonic Dicke effect which results from

dipole−dipole interactions assisted by surface plasmons[112,113]. We will conduct further studies to verify the effect.

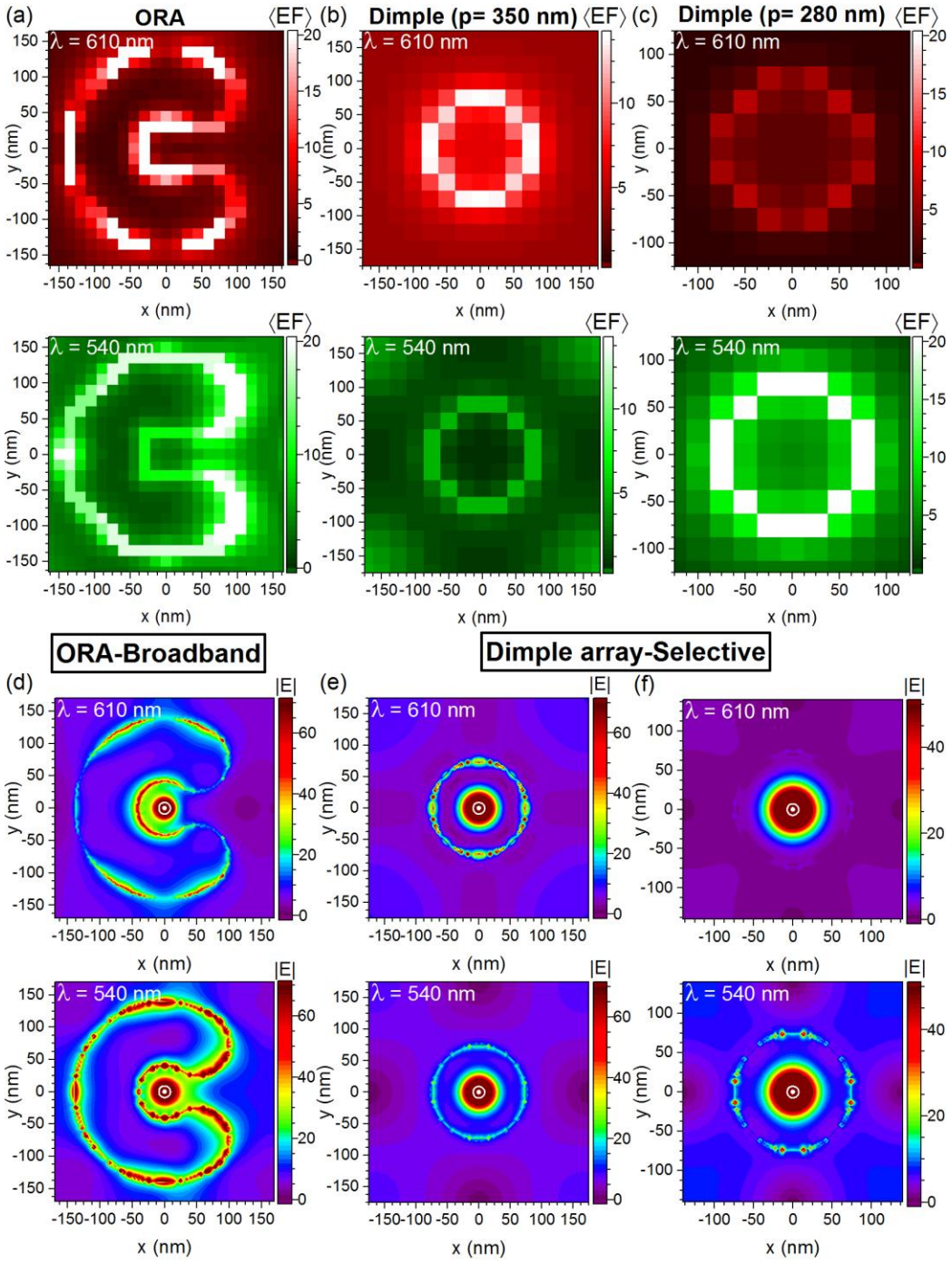

Figure 3.6. Position-dependent enhancement factors of red (610 nm) and green (540 nm) dipole emitters over (a) ORAs (340 nm period), (b) dimple arrays with 350 nm period, and (c) dimple arrays with a 280 nm period. ORAs yield strong enhancements for both red and green emitter while the dimple arrays show wavelength-selective enhancement. (d−f) Electric field profiles are obtained with the dipole emitter placed at the center and oriented perpendicularly to the substrate. Both red and green emitters induce high-intensity hot-spots over a large area of the ORA, whereas the dimple arrays display the hot-spots induced only by specific emission wavelengths.

ORA can be utilized to amplify the fluorescence signal from immobilized molecular beacon (MB) probes as depicted in Figure 3.7(a). The organic fluorophores carried by the MB probes have largely overlapped absorption and emission spectra that lie within the broad resonance spectrum of ORAs in the visible range (Figure 3.7(b)). This property allows both the Purcell effect and the enhanced excitation rate to occur for fluorescence enhancement as illustrated in the route 1 and route 2 interactions in Figure 3.7(c). Also, the strong spectral overlap between fluorophore emission and ORA absorption promotes quenching of the fluorophores in very close proximity to the ORA surface through an efficient FRET process. The strong fluorescence enhancement and quenching will benefit the performance of the MB-based biosensor.

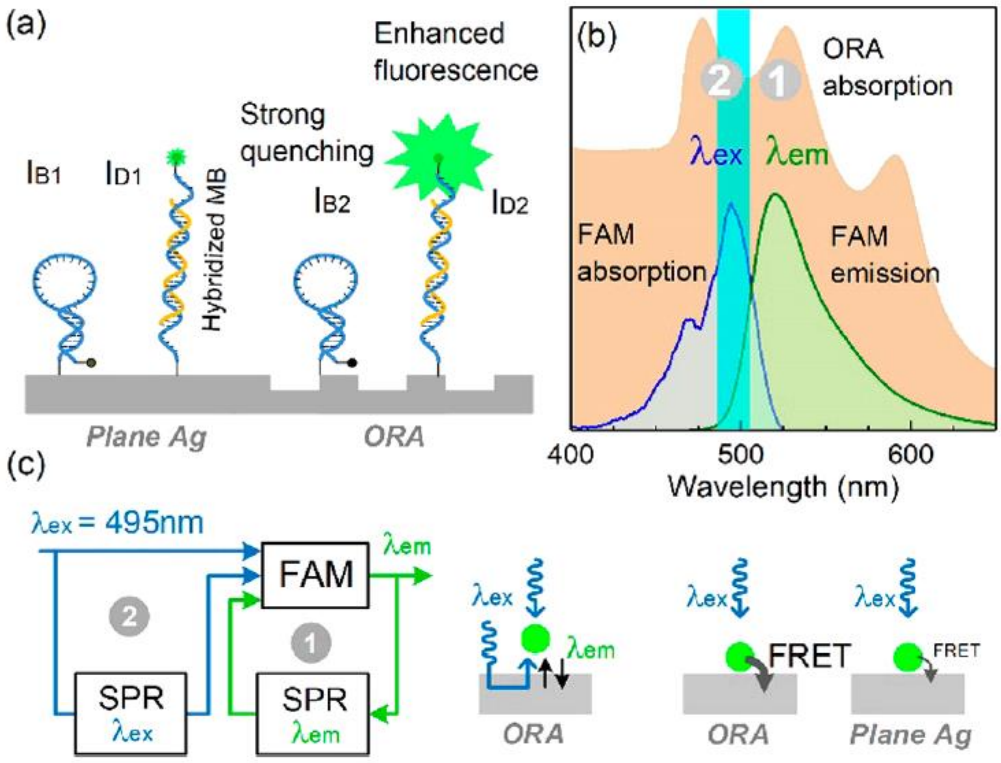

Figure 3.7. (a) Schematic of molecular beacons (MBs) anchored on ORAs and plane silver surfaces. Background intensities I_{B1} and I_{B2} denote the quenched fluorescence on plane silver and ORA surfaces before hybridization. I_{D1} and I_{D2} represent the fluorescence signals of the hybridized MBs on plane silver and ORA surfaces, respectively. (b) The absorption spectrum of an ORA in an aqueous environment (1.33 refractive index) that overlaps the emission and absorption spectra (measured) of the fluorophore. (c) Schematics of the quenching and enhancement mechanisms resulting from the fluorophore−plasmon interaction. Route 1 represents enhanced emission, and route 2 the enhanced excitation.

Combining the ORA plasmonic nanostructures with MB probes, we demonstrate the ultrasensitive detection of DNA without an additional labeling step. The ORA-enabled MBs were composed of 32 base-long synthetic oligonucleotides folded in a stem-loop shape tethered on the Ag ORA surface. The fluorophore, fluorescein amidite (FAM), on the other end of the MB probe was initially quenched by the Ag ORA surface when it coiled up to form a hairpin configuration and brought FAM within a few nanometers above the Ag surface. When the stem-loop opened upon hybridization with target DNA of complementary sequences, the FAM stayed 12−15 nm (estimated by the lengths of a 32 base-long probe and a cross-linker) from the ORA surface, a separation distance sufficient for enhancing fluorescence emission. The multi-resonance spectrum of ORA was designed to overlap both emission and absorption spectra of FAM in an aqueous environment for strong fluorescence enhancement. Figure 3.7(b) shows the resulting absorption spectrum of the Ag ORA substrate in water corresponding to the emission and absorption spectra of a FAM fluorophore. The EFs of FAM fluorophores on a Ag ORA substrate and a plane Ag substrate were measured to be ∼42 and ∼11.8, respectively, with reference to those on glass substrates.

Before the assay, we first annealed the conjugated MBs to form a hairpin configuration and immediately observed a strong fluorescence quenching in the absence of target DNA. The quenched fluorescence intensities on the plane Ag and ORAs were measured as the background signals (I_B), presented as shaded areas in Figure 3.8(a) and 3.8(b). For each substrate, we measured a series of replicates of background signals to obtain

background standard deviation (σ_B). The ORA substrate was found to exhibit a lower background signal compared with the plane Ag surface. The greater fluorescence quenching on the ORA is believed to originate from the efficient energy transfer between the fluorophore and surface plasmons through the FRET process explained previously. After hybridization, the detected fluorescence intensity (I_D) on the ORA increases significantly with the target DNA concentration while that on the plane Ag surface rises slightly. Strong fluorescence enhancements started to occur in the ORA region as the target DNA concentration exceeded 100 fM. The fluorescence intensities on three ORAs were measured to observe consistent results. We emphasize that all the fluorescence signals were measured within a 10-s exposure to avoid photobleaching. We calculated the limit of detection (LOD) defined as the concentration that yields a net fluorescence signal ($I_D - I_B$) equivalent to three times the background standard deviation ($3\sigma_B$)[114]. The ORA sensor achieved a LOD estimated to be ~300 fM, equivalently 360 zmol in a 1.2 μL microfluidic chamber volume, whereas the plane Ag sensor has the LOD of about 6 nM. The results indicate that ORAs enhance the LOD by more than 4 orders of magnitude as compared to the plane Ag. We verified the selectivity of the sensors by detecting the analytes with nontarget DNA. The fluorescence intensities for the nontarget detection were found to be insignificant compared with the LOD level, implying the high selectivity of detection. The signal-to-noise ratio (SNR) defined as the I_D/I_B ratio under each DNA concentration quantifies the change in fluorescence signal before and after hybridization. The signal change ratio acquired from the ORA sensors are much more distinguishable because it provides

a lower background signal due to the strong quenching at the initial status and the enhanced fluorescence signals upon the binding of target DNA. The results can be observed from the fluorescent images of the ORA sensors at various target DNA concentrations in Figure 3.8 (d).

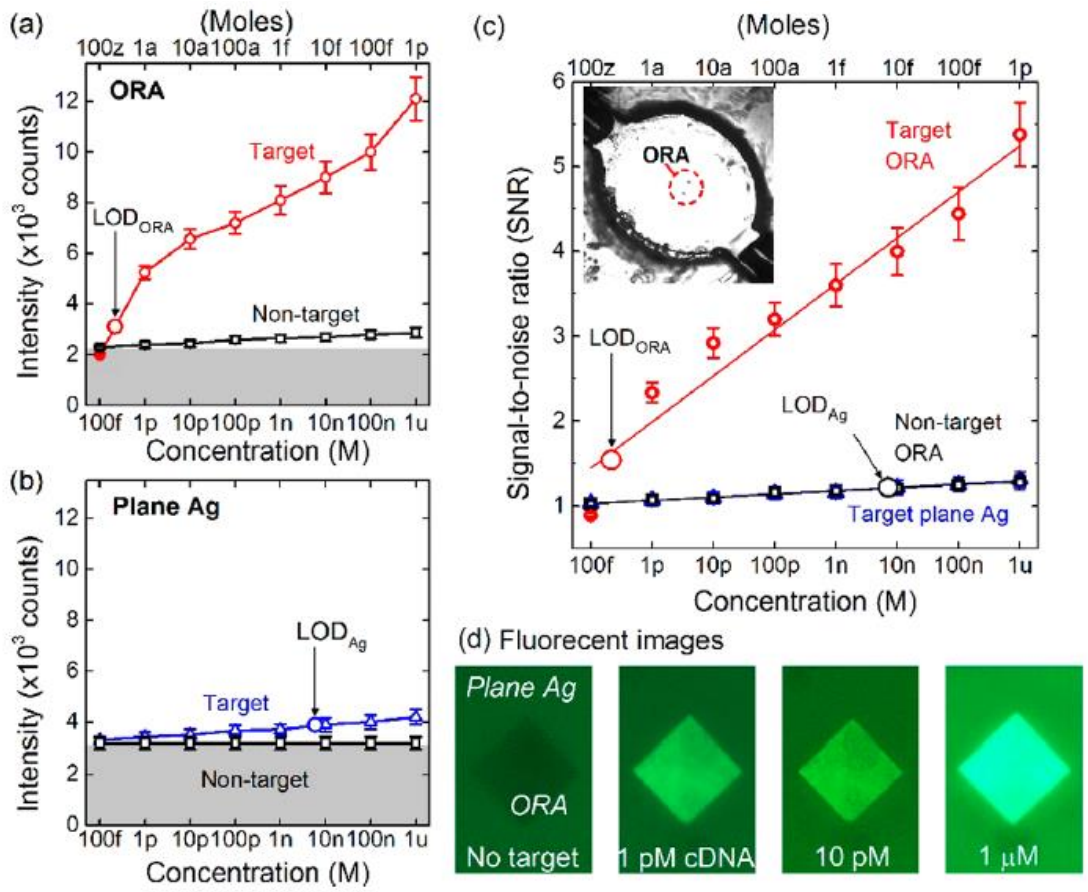

Figure 3.8. Fluorescence intensities on the (a) ORA and (b) plane Ag surface in the presence of target and nontarget DNA. Three devices were evaluated for the detection assays. The shaded areas indicate the initial background fluorescence intensity I_B at

quenching status. The limit of detection (LOD) is about 300 fM for ORA and 6 nM for plane Ag, respectively. (c) Signal-to-noise ratio (SNR) acquired from the ORA and plane Ag substrates with reference to IB. The inset microscopic image shows the Ag ORA sensors integrated into a 1.2 μL-sized microfluidic chamber. (d) Fluorescence images of the device at various concentrations of complementary target DNA. The dimension of the ORA is 150 μm × 150 μm.

3.4 Summary

We utilized multicolor QDs and variable excitation wavelengths accompanied by theoretical analysis to elucidate the fluorescence enhancement property of a Ag open-ring nanoarray (ORA) on which to demonstrate ultrasensitive DNA detection. The ORA offers multiple resonance peaks that cover the absorption and emission spectra of the fluorophores in the visible range to support both emission and excitation enhancements. The spectral overlap also enhances quenching of the fluorophores in close proximity to ORA due to the improved efficiency of the FRET process. We observed amplified DNA detection signals using ORA-enabled MB probes that reduce the background signal level and intensify the fluorescence intensity in response to the binding of target DNA. The ORA sensor yields a detection limit of sub-picomolar concentration (~300 fM) or equivalent sub-attomoles, four orders of improvement in detection limit as compared with the approach using a plane Ag substrate. The sensitive and selective DNA detection method enabled by the signal enhancement approach will benefit applications in biological analysis and medical diagnostics.

CHAPTER 4. ALUMINUM ULTRAVIOLET-VISIBLE PLASMONIC ARRAYS FOR BROADBAND AND WAVELENGTH-SELECTIVE ENHANCEMENTS OF QUANTUM DOT EMISSION

In the previous chapters, QD enhancement of both broadband and wavelength-selective is presented using gold and silver arrays. In this chapter, both the enhancements are presented using Aluminum UV-visible plasmonic arrays which find several applications in solar cells, microLED displays, and other optoelectronic devices.

4.1 Introduction

The enhancement through two-dimensional plasmonic arrays is advantageous in providing greater enhancement factors and enabling integration with metal electrodes for multiple optoelectronic applications. Aluminum is a suitable alternative to noble metals for plasmonic applications[115-123]. It is an abundant, inexpensive material widely used as the metal electrodes in optoelectronic devices. More importantly, it has a negative real part of the relative permittivity at wavelengths spanning from the visible to the ultraviolet range even at the wavelength shorter than 200 nm where the imaginary part remains relatively low. Such an optical property makes aluminum superior to gold or silver in supporting strong surface plasmon resonances (SPRs) covering both visible and UV regions of the spectrum[124]. Taking advantage of the unique property of aluminum, we demonstrate the use of Al dimple arrays (Fig. 4.1) with their SPRs

tailored to be in the UV range for broadband enhancement of multicolor QD emission and in the visible light region for enhancement of wavelength-selective QD emission, all under 390-nm excitation. The Al dimple array is a periodic array of 100-nm deep Al holes closed at one end on a 200-nm thick Al thin film. Different from metal through-hole arrays, the Al dimple array presented here exhibits a major SPR mode throughout the UV and visible range; there is no observable gap mode or the modes resulting from the coupling between both sides of metal interfaces. The Al structure may be easily oxidized to form a 2–3 nm thick native aluminum oxide layer under atmospheric conditions[125] and results in a red shift in the SPR peak position[126]. However, the challenge does not significantly affect the plasmon enhanced spontaneous emission as a thin insulating layer of at least about 5 nm is required to prevent the unwanted emission quenching due to the direct contact of QDs with the metal surfaces[127]. We introduced QD to the Al dimple array surface by spin coating a 30-nm thick QD-embedded polymer layer that provides a short enough distance for most of the QDs to interact with surface plasmons while avoiding quenching.

4.2 Results and Discussion

Plasmon-enhanced QD emission can be carried out by different routes of couplings between QDs and surface plasmons. An excited QD interacts with the free electrons on a metal surface in the vicinity and creates additional energy relaxation channels through plasmon excitations that reduce the QD emission lifetime[128-134]. The phenomenon, referred to as the Purcell effect, originates from the increased number of photon modes

accessible for emission, i.e., the local density of states (LDOS), and results in enhanced spontaneous emission rate and radiative intensity. Plasmonic structures support the Purcell effect by providing strong local electric field enhancements in a sub-diffraction limit volume that strongly modifies the LDOS for QDs. The effect can be realized through the coupling of QD emission with the resonant modes of the optical environment, such as plasmonic cavities[135,136] and plasmonic surfaces. This enhancement pathway requires the spectral overlap between the QD emission wavelength and the SPR indicated as the Route-1 coupling in Fig. 4.1(b). In this case, the period, p, of the Al dimple array is designed to match its absorption resonance spectrum with the QD emission peaks in the visible range. For instance, as shown in Figs. 4.1(c) and 4.1(d), the dimple array with a 450-nm period produces an absorption peak at 540 nm and will be used to enhance QD with a 540-nm emission wavelength. The dimple array with a 550-nm period was designed to enhance 610-nm QD emission in the same way. The Route-1 coupling using the visible-light plasmonic Al dimple array leads to wavelength-selective emission enhancement.

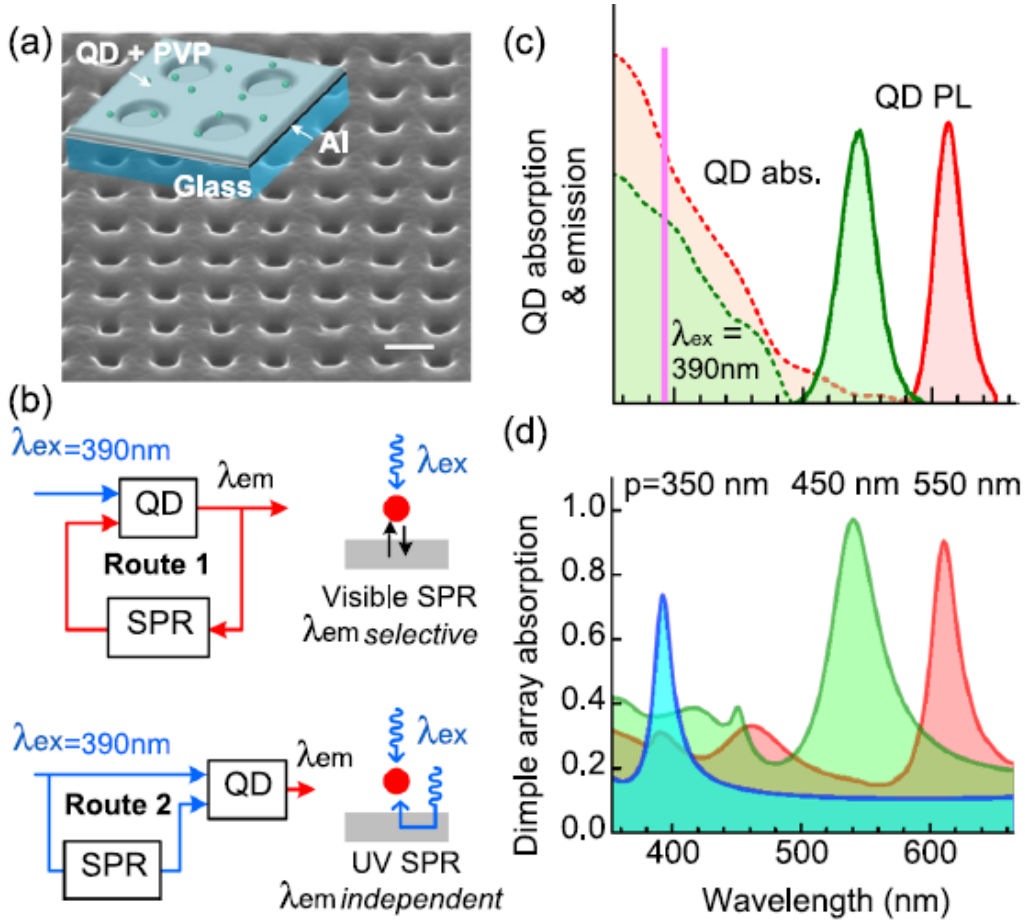

Figure. 4.1. SEM image and schematic of an Al dimple array with a 550-nm period and 240-nm hole diameter fabricated using focused-ion beam milling and spin coated with a QD-embedded PVP thin film (scale bar: 500 nm). (b) Schematics of QD enhancement routes contributed by different QD-surface plasmon coupling pathways. Route 1: Emission enhancement relies on the interaction between QD emission and surface plasmon resonance (SPR) around the same wavelength. Route 2: Excitation enhancement results from the extra near-field excitation of QDs by the surface plasmons created by far-field illumination. Both enhancement routes are realized by the same excitation wavelength λ_{ex}=390 nm. The enhancement route is determined by

the choice of SPR wavelength of the substrate. (c) Measured emission and absorption spectra of green and red QDs with the emission peak wavelengths λ_{em}=540nm and 610 nm, respectively. (d) Absorption spectra of the 30-nm thick PVP-coated Al dimple arrays with 350-nm, 450-nm, and 550-nm periods each of which yields a major absorption peak at 390 nm, 520 nm, and 610 nm, respectively.

QD emission can also be enhanced by additional nearfield excitation of UV surface plasmons. The SPR of the Al dimple array substrate designed to peak in the UV range where the absorption of QDs is noticeably strong can enhance multi-color QDs. As indicated by the Route-2 coupling in the schematic of Fig. 4.1(b), the 350-nm period Al dimple array efficiently absorbs far-field 390-nm UV illumination, creates UV surface plasmons and produces extra excitation of QDs in the near field. This approach relies on the generation of UV surface plasmons which cannot be achieved by using common noble metals, such as gold, with the SPR limited in the visible range. The UV-plasmonic Al dimple array is expected to provide broadband enhancement of QD emission independent of the emission wavelengths.

It is worth noting that both Route-1 and Route-2 couplings can take place simultaneously to enhance most organic fluorophores which exhibit a considerable overlap of absorption and emission spectra in the visible range. The plasmonic substrate designed to match its resonance peak with the fluorophore emission can also efficiently absorb the external illumination for fluorophore excitation. The surface plasmons created by the far-field absorption further supply an extra excitation of the fluorophores

in the near field. As a result, both pathways concurrently contribute to the enhanced fluorophore emission. Different from organic fluorophores, QDs have weak absorption near their emission range but have strong absorption in the UV regime as shown in Fig. 4.1(c). The plasmonic substrate with a single major SPR peak in the visible range does not take advantage of excitation enhancement, and the Route-1 wavelength-dependent coupling dominates the enhanced emission. With the Route-2 coupling, the absorption of far-field UV illumination efficiently supports additional strong near-field excitation of QDs.

The 100-nm deep Al dimple arrays of various periodicities were fabricated by focused-ion beam (FIB) milling of a 200-nm thick Al layer and a 5-nm thick titanium adhesive layer deposited by thermal evaporation on a glass substrate. Commercially available CdSe/ZnS QDs (Ocean Nanotech) were dispersed in 0.9 mg/ml methanolic polyvinylpyrrolidone (PVP-10) solution and spin-coated on the Al dimple arrays to form a 30-nm thick QD-embedded PVP thin film after drying. The polymer layer prevents the direct contact of most QDs to the metal surface that avoids any possible quenching of QD emission. Figure 4.1(a) shows the SEM image of a typical Al dimple array with the 550-nm period and 240-nm dimple diameter. A 90-nm dimple diameter was applied for the 350-nm period array.

The absorption and photoluminescence (PL) emission spectra of QDs in Figs. 4.1(c) and 2 were measured by using a spectrometer (HR4000, Ocean Optics) and a spectrofluorometer (Fluoromax-4, Horiba) coupled to an inverted microscope (IX73, Olympus), respectively. The PL excitation delivered from the spectrofluorometer was

a continuous-wave light source with a power density measured to be about 70 mW/ cm2 after a 60microscope objective that did not saturate the QD PL. The ratio of the QD PL peak on the dimple array to that on the glass substrate was calculated to quantify the enhancement factor (EF). The fluorescent images in the insets of Fig. 4.2 were captured by a color CCD camera (Lumenera Infinity3-3UR) on the inverted microscope. The PL spectra and fluorescence images in Fig. 4.2(a) show that the UV-plasmonic dimple array with the 350-nm period enhances both green and red QD emissions with the EFs of 22 and 15, respectively. The 350-nm period dimple array has a plasmon resonance peak at 390 nm [Fig. 4.1(d)] that efficiently absorbs 390-nm UV excitation to produce surface plasmons and promotes the excitation of both red and green QDs in the near field. The visible-light plasmonic dimple array of the 450-nm period selectively enhances green QDs with EF=15, while the 550-nm period dimple array exclusively enhances red QDs with an EF=16 as shown in Fig. 4.2(b).

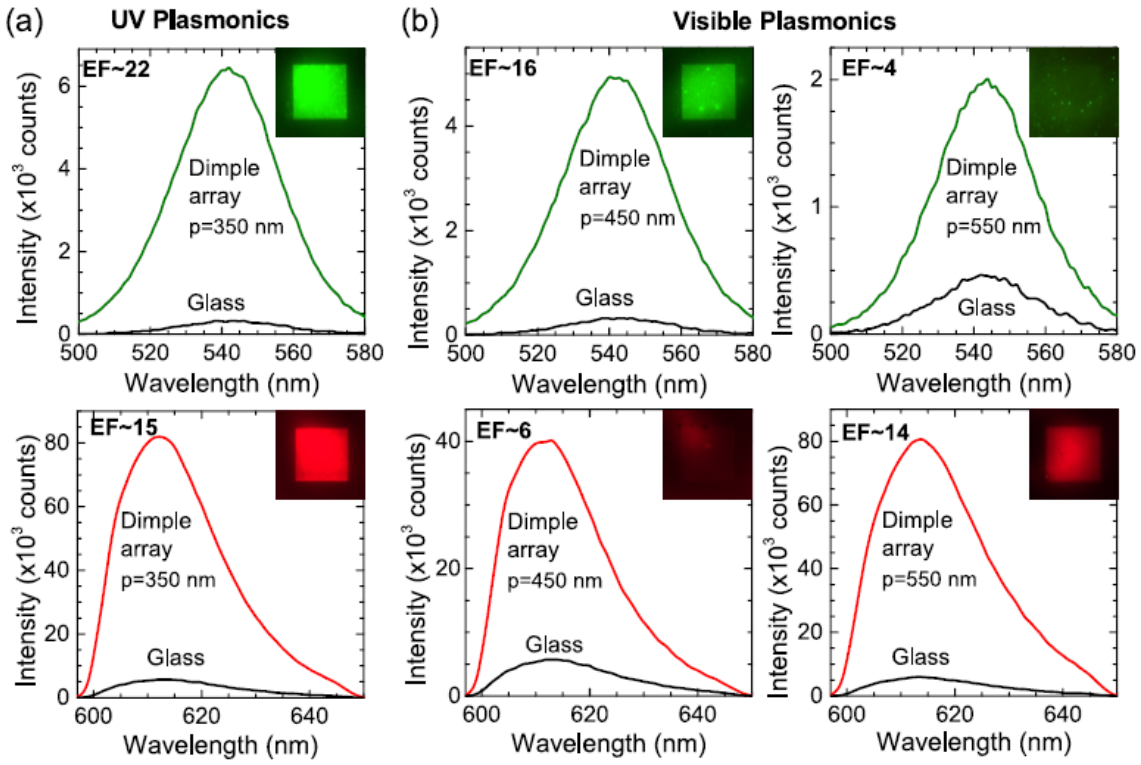

Figure. 4.2. Measured photoluminescence (PL) spectra of green and red QDs spin-coated on (a) the UV plasmonic dimple array with a 350-nm period and (b) the visible plasmonic dimple arrays with 450-nm and 550-nm periods. All samples were excited by a 390-nm light source.

The effect of the substrate SPR on broadband and wavelength-selective enhancement as verified by finite-difference time-domain (FDTD) simulations. In Fig. 4.3, we summarize the position-dependent EF of a single dipole emitter (540-nm and 610-nm emission wavelengths) across a unit cell of the dimple arrays of three different array periods illuminated by a 390-nm plane wave. The EF value at each position was calculated by averaging the results of three dipole emitters polarized along x, y, and z

directions. The $\langle EF \rangle$ averages the enhancement factor over the entire unit cell. The results imply that the edges of the dimple structure contribute the majority of the EF due to the presence of high-intensity electric field hot-spots. Overall, the UV-plasmonic dimple array gives a theoretical average enhancement factor of about 8 for both green and red dipole emitters as shown in Fig. 4.3(a). Figure 4.3(b) shows the position-dependent EFs of red and green QDs on two different visible-light plasmonic dimple arrays. The results qualitatively agree with the experimental observations. The red QDs on the 550-nm period dimple array were enhanced more than those on the 450-nm period counterpart; an opposite trend of enhancement was observed for green QDs. The UV plasmonic dimple array enhances multicolor QDs through the additional near-field excitation. The strong electric field profile in Fig. 4.3(c) indicates that the 350- nm period dimple array efficiently absorbs 390-nm UV excitation light and converts the energy into UV surface plasmons for extra excitation of QDs on the surface. Such a process referred to as the Route-2 coupling enhances the QDs independent of their emission wavelengths. Differently, the dimple arrays with the 450-nm period and 550-nm period have distinct resonant modes that absorb the QD emission of the selective wavelength instead of the UV illumination.

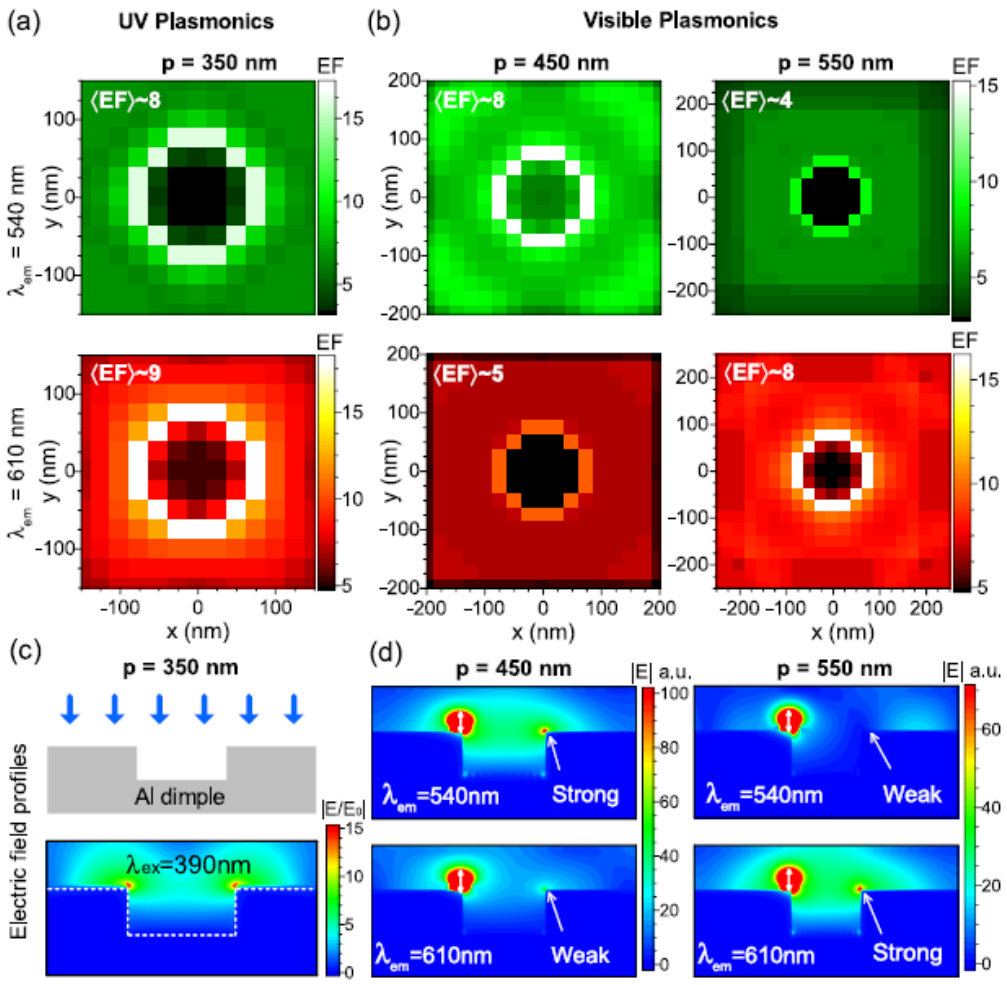

Figure. 3. Calculated position-dependent enhancement factors (EFs) of a single UV-excited red (540-nm emission) or green (610-nm emission) QD (dipole emitter) on a unit cell of (a) a UV plasmonic dimple array with the 350-nm period and (b) visible plasmonic dimple arrays with 450-nm and 550-nm periods. The dipole emitter is placed 10 nm above the metal surface and is positioned with a step size of 20 nm. (c) Cross-sectional electric field profiles of the 350-nm period UV plasmonic dimple array under far-field excitation of 390-nm light. (d) Cross-sectional electric field profiles of the 450-nm period (left) and 550-nm period (right) visible plasmonic

dimple arrays induced in the near field by a dipole emitter (indicated by the double-headed arrows) with 540-nm or 610-nm emission wavelength placed at 10 nm above the edge of the hole on an Al dimple array.

The surface plasmon excited by the QD emission in the near field at a specific wavelength can be observed through the electric field profiles in Fig. 4.3(d). The enhancement is fulfilled by the interaction between QD and surface plasmons via the Route-1 coupling. The calculated EFs, which consider the effect of a single QD, are lower than the experimental results that involve an ensemble of multiple QDs. The discrepancy may be attributed to the presence of mutual enhancement among QDs associated with a plasmonic Dicke effect resulting from the dipole-dipole interactions assisted by surface plasmons[137,138].

4.3 Summary

The wavelength-selective and broadband enhancement of QD emission using Al dimple arrays that have the plasmon resonance tailorable from the UV to the visible range is presented. The enhancement effects are contributed by two different coupling routes created by the interaction between QD emission and surface plasmon resonance and extra near-field excitation of QDs by the surface plasmons induced by the absorption of far-field illumination. The Al plasmonic design will be suitable for photovoltaic applications in improving ultraviolet light harvesting. It is also beneficial for QD-based biosensing that takes advantage of excess UV excitation from surface plasmons to boost the fluorescence signals from multicolor QD probes.

CHAPTER 5. HYPERBOLIC METAMATERIALS FOR QUANTUM DOT ENHANCEMENT: EFFECT OF UNIT CELL THICKNESS AND LARGE AREA OUTCOUPLING

5.1 Introduction

Quantum dot (QD) enhancement using multilayer hyperbolic metamaterials (HMMs) consisting of alternating subwavelength layers of metal and a dielectric have been studied extensively in recent years[139-141]. The periodic multilayer HMMs creates anisotropy in permittivity and leads to unique optical properties compared with their counterparts in nature. In the hyperbolic region, an infinite number of optical modes with large wave vectors enabled by coupled surface plasmon polaritons (SPPs) provide large local density of photonic states for spontaneous emission rate enhancement of QDs, in other words, an enhanced Purcell factor[142-151]. The tunability of elliptic and hyperbolic regimes by changing the metal filling ratio and unit cell thickness leads to several applications in fluorescence enhancement.

Ideally, HMMs have infinite density of photonic states which leads to a large Purcell factor of QDs. However, in multilayer HMMs, the presence of anomalous optical modes is highly dependent on unit cell thickness[152]. Unit cell thickness is a critical factor for achieving the expected hyperbolic regime, number of optical modes, and Purcell factor. In the past, few research groups have presented a deviation of HMM properties because of lack of unit cell thickness control[153], but no experimental

attempt was made to demonstrate this effect. An HMM with thick unit cell thickness hinders the performance of fluorescence enhancement and leads to enhancement factors lower than the ones achieved through surface plasmonic arrays, metal nanoparticles and photonic crystals.

In addition, a large emission enhancement of QDs are high-k waves and needs to have additional mechanisms incorporated to outcouple the light from HMM. In the past, subwavelength gratings[154], photonic crystals[155], and photonic hypercrystals[156] were fabricated to assist light out-coupling. However, all the mechanisms involve complex fabrication techniques, lack of large area enhancement and lower enhancement in relative to QDs on glass substrate.

In this research work, we study the effect of unit cell thickness of Ag/ITO based multilayer HMM over enhancement factor of QDs and we employ a new technique to outcouple the light over a large area using polystyrene microbeads. We achieved a maximum of 40-fold enhancement of QDs over a large area which is larger than previously reported enhancement factors via plasmonic arrays[157,158] and other photonic crystals.

5.2 Theory

As discussed, the enhanced photonic density of states has a consequence on the spontaneous emission lifetime of QDs in the near-field of the HMM, based on Fermi's golden rule[159]. In HMMs, due to the presence of a large number of modes, there exists an increase in the decay rate of QDs causing an enhancement in spontaneous

emission, in other words, called as Purcell effect. The number of modes available for QDs to recombine and emit a photon is highly dependent on the unit cell thickness of the HMM. Using transfer matrix method[160]:

$$\rho(\lambda, d, \vec{k}) = \frac{3}{2}\frac{1}{k_1^3}\frac{1}{|\vec{\mu}|^2}\frac{k_x}{k_z}e^{i2k_z d}\left\{\frac{1}{2}\mu_{\parallel}^2[(1+r^{(s)})k_1^2 - (1-r^{(p)})k_z^2] + \mu_{\perp}^2[(1+r^{(p)})k_{\parallel}^2\right\}$$

where $r^{(s)}$ and $r^{(p)}$ are the reflection coefficients for s- and p-polarized light, k_1 is the magnitude of the wavevector in the dipole medium, $k_1 = \sqrt{\varepsilon}(\omega/c)$, we calculated the local density of photonic states (LDOS) for Ag/ITO based HMM with total thickness of 320 nm, filling factor of 0.25, and unit cell thicknesses of 20, 40, and 80 nm as shown in the Figure 5.1(a-c).

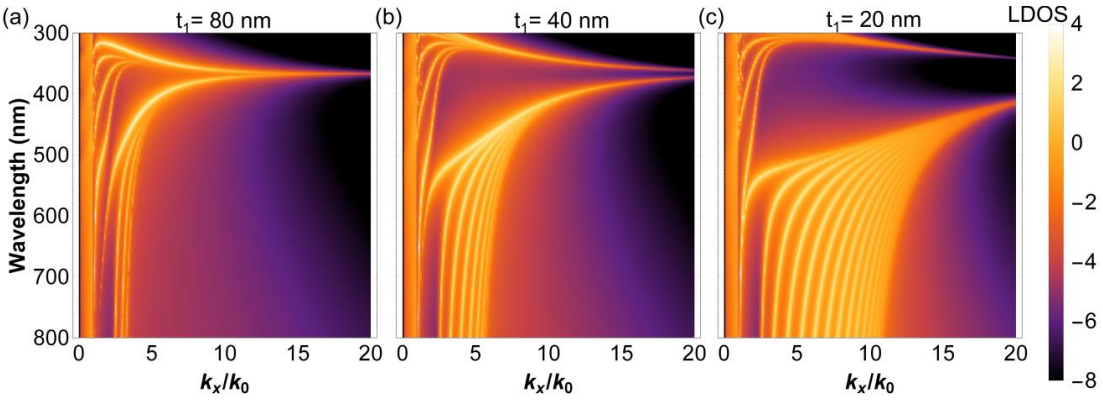

Figure 5.1. The LDOS (normalized by vacuum) available to a quantum emitter located on the top of HMM with (a) 80 nm, (b) 40 nm, and (c) 20 nm unit cell thickness. The number of HMM modes increase with the bi-layers leading to LDOS enhancement.

We observe the series of bright vertical bands as high-k modes that arise from the coupled surface plasmons between the metal layers. As we decrease the unit cell thickness from 80 nm to 20 nm, we find an increase in number of HMM modes leading to an increase in Purcell factor according to following equation:

$$\beta = (1 - \eta) + \eta\, Re\left[\int_0^{\infty} \rho(\lambda, d, \vec{k})\, dk_{||}\right],$$

where η is the intrinsic quantum yield. The increase in Purcell factor is shown in the Figure 5.2(e).

5.2 Results and Discussions

Figure 5.2(a) illustrates the schematic configuration of Ag-ITO based multi-layered hyperbolic metamaterials (HMMs) coated with CdSe/ZnS quantum dots (QDs) on the top. The multilayer consists of alternating pairs of Ag and ITO layers. The HMMs were created by sputtering over the glass substrate, and a 10 nm thick ITO spacer is deposited on top of HMM before spin coating QDs, so as to avoid any possible quenching via charge transfer. As indicated by scanning electron microscopy (SEM) image in Figure 5.2(b), the HMM consists of four pairs of 80 nm unit cell with a metal filling fraction (ff) of 0.25, the unit cell thickness of 80 nm, and the total thickness of 320 nm.

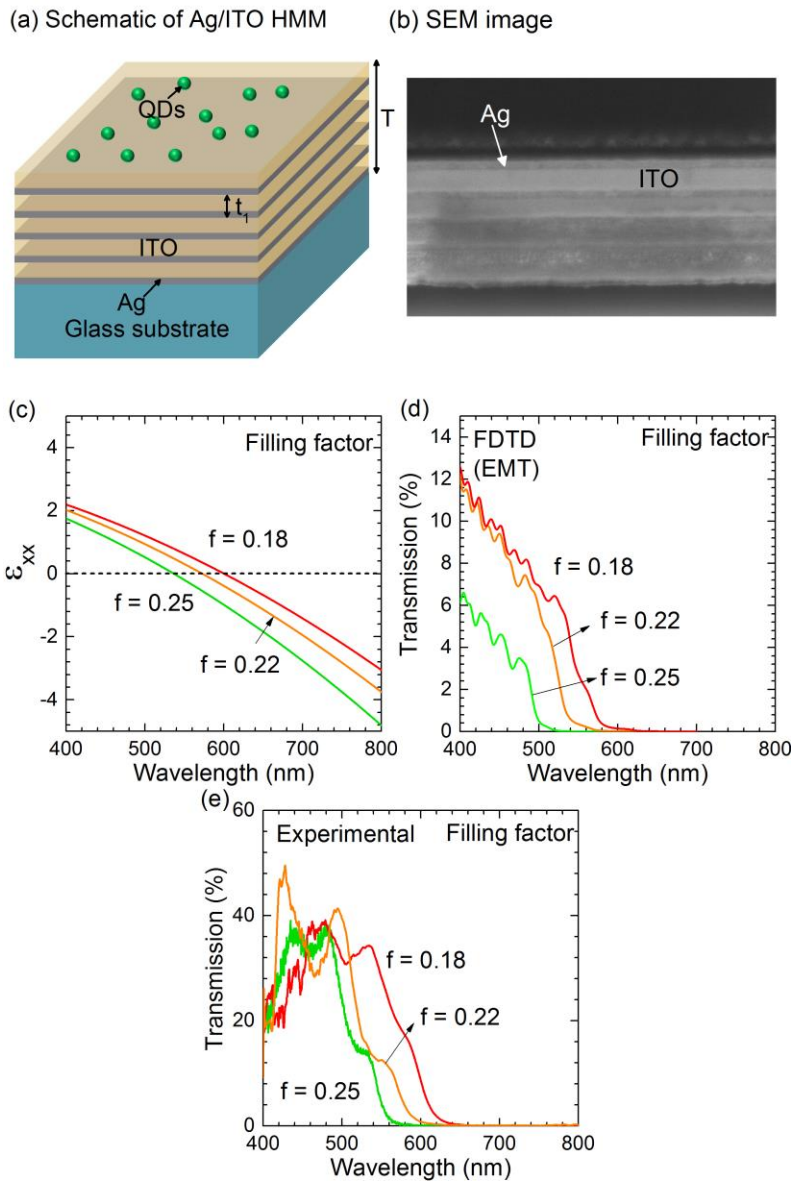

Figure 5.2. (a) Schematic of Ag/ITO based hyperbolic metamaterial (HMM), (b) SEM image of HMM with 80 nm unit cells, (c) permittivity along x-axis with change in filling fractions of 0.18, 0.22, and 0.25 respectively, (d) simulated and (e) measured transmission spectra of 80 nm HMMs with three different filling factors.

The epsilon-near-zero (ENZ) point, which determines the transition from elliptic to hyperbolic dispersion, is tunable by varying metal filling fraction as shown in Figure 5.2(c). Lower filling fraction results in redshift in the ENZ wavelength and is identified by measuring the transmission spectra of the HMMs. Figure 5.2(d) shows the transmission spectra calculated using the finite-difference time domain (FDTD) analysis and effective medium theory (EMT). The transmission becomes zero in the hyperbolic region; the falling points indicate the ENZ wavelength. We observed a redshift of ENZ wavelength when the metal filling fraction was reduced from 0.25 to 0.18 as shown in Figure 5.2(e) which agree with theoretical results.

As discussed previously, the large LDOS in HMMs can induce dramatic Purcell enhancement especially when the emission wavelength of QDs matches ENZ wavelength. An ideal HMM consists of an infinite number of modes for emission enhancement, however, in multilayer based HMMs the unit cell thickness has to be minimized to reach the ideal condition for Purcell enhancement. In this work, we study the effect of unit cell thickness on the emission of 520 nm QDs on HMM with filling fraction of 0.25 that has ENZ wavelength at 520 nm as shown in Figure 5.3(a). The cross-sectional SEM images in Figure 5.3(b) show the 320 nm thick HMMs formed by 80 nm, 40 nm, and 20 nm unit cell thicknesses. The simulated and measured transmission spectra of three different HMMs in Figure 5.3(c) and 5.3(d) indicate that the ENZ wavelength approaches the result estimated using EMT as the unit cell thickness decreases.

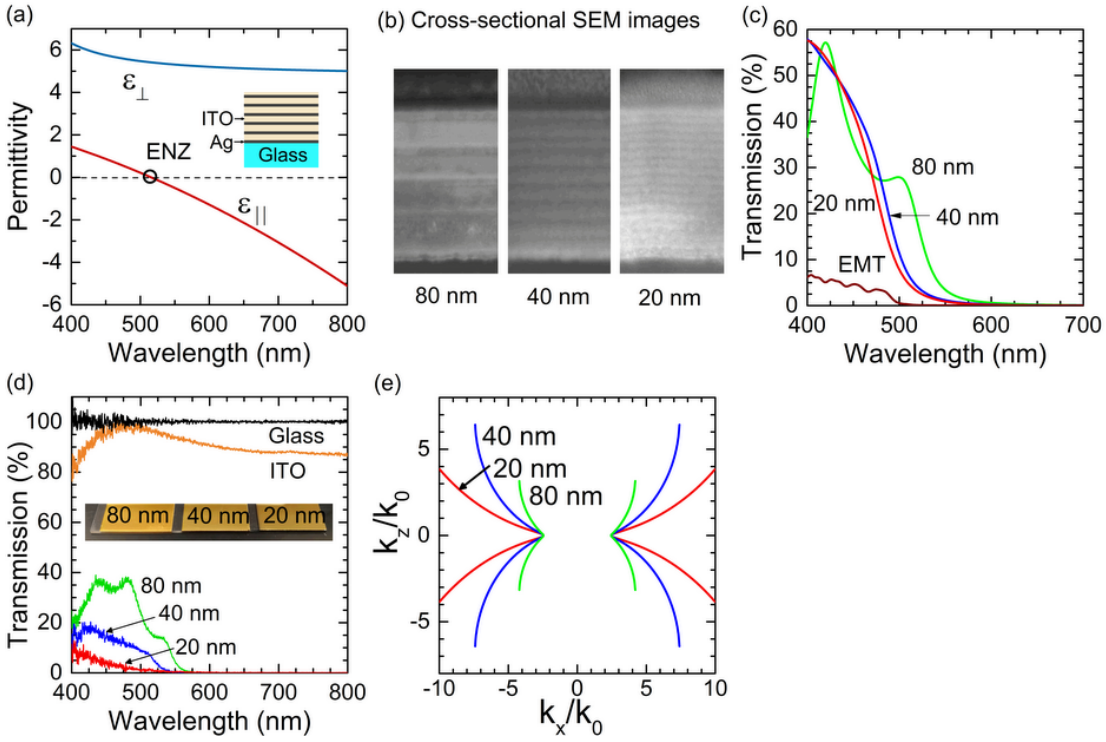

Figure 5.3. (a) Parallel and perpendicular permittivity of 0.25 fill factor pointing epsilon-near-zero (ENZ) point. (b) Cross-sectional SEM images of 320 nm thick HMMs formed by various unit cell thickness—80 nm, 40 nm, and 20 nm which correspond to 4, 8 and 16 bilayers. (c) Simulated and (d) measured transmission spectra of all three HMMs (Inset: bird eye images of HMMs). (e) Iso-frequency curves of HMMs. (f) Purcell factor spectra of HMMs.

The transformation of HMM from finite to infinite local density of photonic states is realized by the iso-frequency curves of the respective HMMs as shown in Figure 5.3(e), using Bloch theorem[161].

The iso-frequency curves of the multilayered HMMs in Figure 5.3(e) show that the Ag/ITO multilayered structure exhibits hyperbolic dispersion as the unit cell thickness decreases. Because of the larger LDOS supported by hyperbolic dispersion, the Purcell factor of the dipole emitters will be enhanced accordingly for the HMM with a reduced unit cell thickness as shown in Figure 5.3(f).

Despite the enhanced Purcell factor, the enhanced light emission is mostly high-k waves within HMM which requires additional approach for light extraction. Here we utilize self-assembled polystyrene (PS) nanoparticle monolayer on top of the HMM fabricated by a Langmuir process as depicted in Figure 5.4(a) to outcouple the enhanced QD emission to the free space. Figure 5.4(b-c) shows the cross-sectional and top view of SEM images with HMMs covered by a monolayer of 500 nm PS monolayer. The photoluminescence (PL) measurements show that without light extraction only 1.8-fold enhancement was observed for the QDs on the HMM with 20 nm unit cell (16 bilayers) compared with those on a glass substrate as shown in Figure 5.4(f). Three different PS nanoparticles (200 nm, 500 nm, and 750 nm) were self-assembled on these HMMs for light outcoupling. Figures 5.4(d-f) show that the PL enhancement of QDs and the enhancement factor increase from 12.6-fold for 80 nm unit cell (4 bilayers) to 40-fold for 20 nm unit cell (16 bilayers). The outcoupling factor is determined by the ratio of emission intensity in the presence and absence of PS nanoparticle monolayer. The monolayer composed of 750 nm PS nanoparticles was found to have a larger outcoupling factor of 22 times in comparison with 500 nm and 200 nm particles that provide 13 times and 7 times of outcoupling factors, respectively.

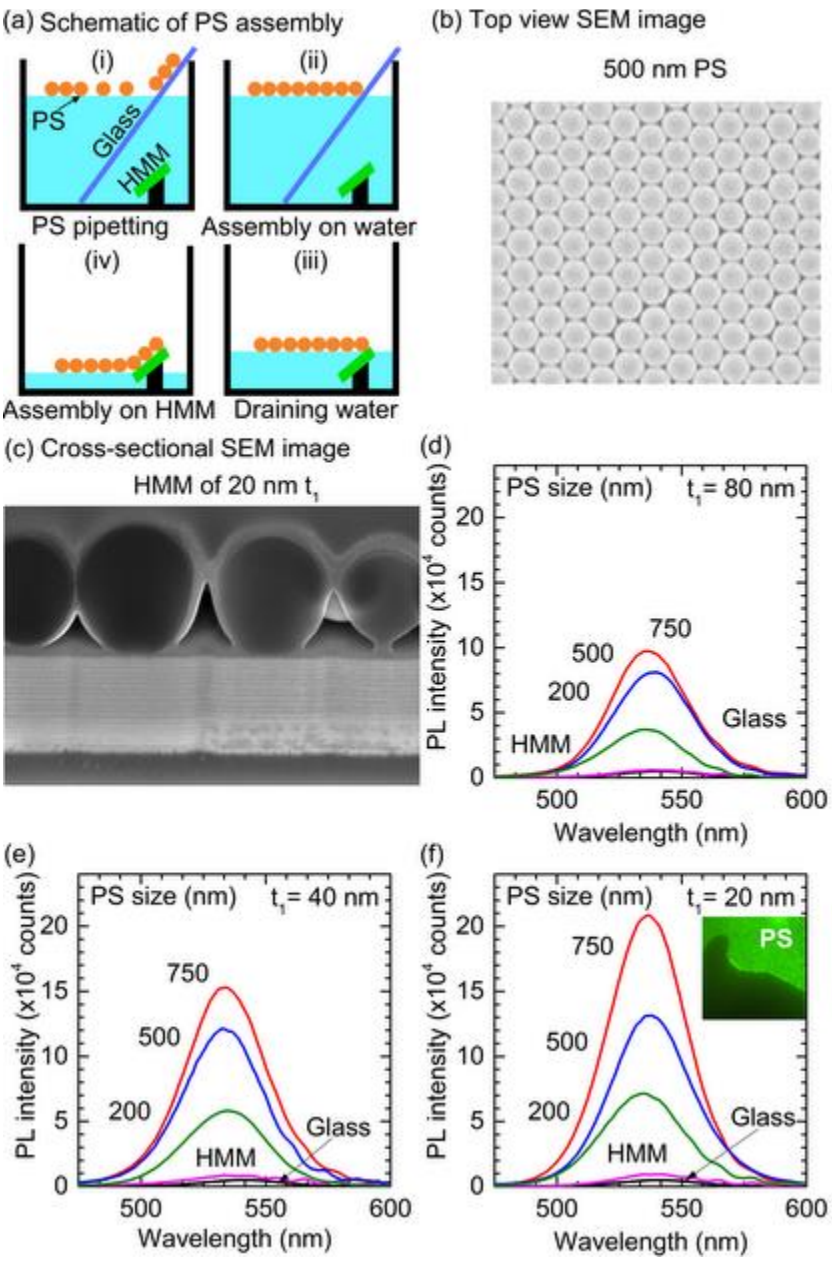

Figure 5.4. (a) Schematic of the self-assembly of polystyrene nanoparticle monolayer. (b) Top view and (c) cross-sectional SEM images of the resulting nanoparticle monolayer. Photoluminescence spectra of 540 nm emission quantum dots spin-coated over HMMs with the unit cell thickness of (d) 80 nm, (e) 40 nm, and (f) 20 nm with

outcoupling via a monolayer of polystyrene nanoparticle of 200, 500 and 750 nm in diameter.

The outcoupling factor is related to the size and refractive index of PS nanoparticles but is independent to the HMMs. No change in enhancement factor was observed for QDs on a glass substrate with and without PS nanoparticle monolayer, which agree with the simulated results.

To further visualize and understand the out-coupling mechanism, we realize the electric field profiles of this system as shown in Figure 5.5. Using FDTD, a dipole with an orientation parallel to HMM surface is located under the PS microbeads and electric field intensity distribution at x-z plane (y=0) is observed. Figure 5.5(a) shows electric field intensity of plane HMM, which is weak and only distributed at the center. This is due to the lack of outcoupling efficiency as discussed in the previous sections. Much stronger intensity was observed for the HMMs with sphere arrays, with 750 nm PS microbeads being the maximum. The sphere arrays serve as the graded refractive materials to reduce the refractive index contrast and provide additional momentum for outcoupling these high-k waves[162]. The light coupled to the PS microbeads undergoes an internal reflection at the PS-air interface, and based on the phase difference between the reflected wave and the original wave, constructive interference occurs leading to the higher light intensity, and eventually results in higher out-coupling factors[163-165]. The comparison of far-field radiation patterns for the plane

HMM and HMMs with PS microbeads is presented in Figure 5.5(b). The far-field intensity of plane HMM is weaker in all the directions compared to those of the LEDs with PS beads due to the small light escape cone and lack of out-coupling. The far-field intensities exhibit hexagonal symmetry due to hexagonally packed microbead arrays. The outcoupling factor for various conditions is simulated using FDTD as shown in Figure 5.5(c).

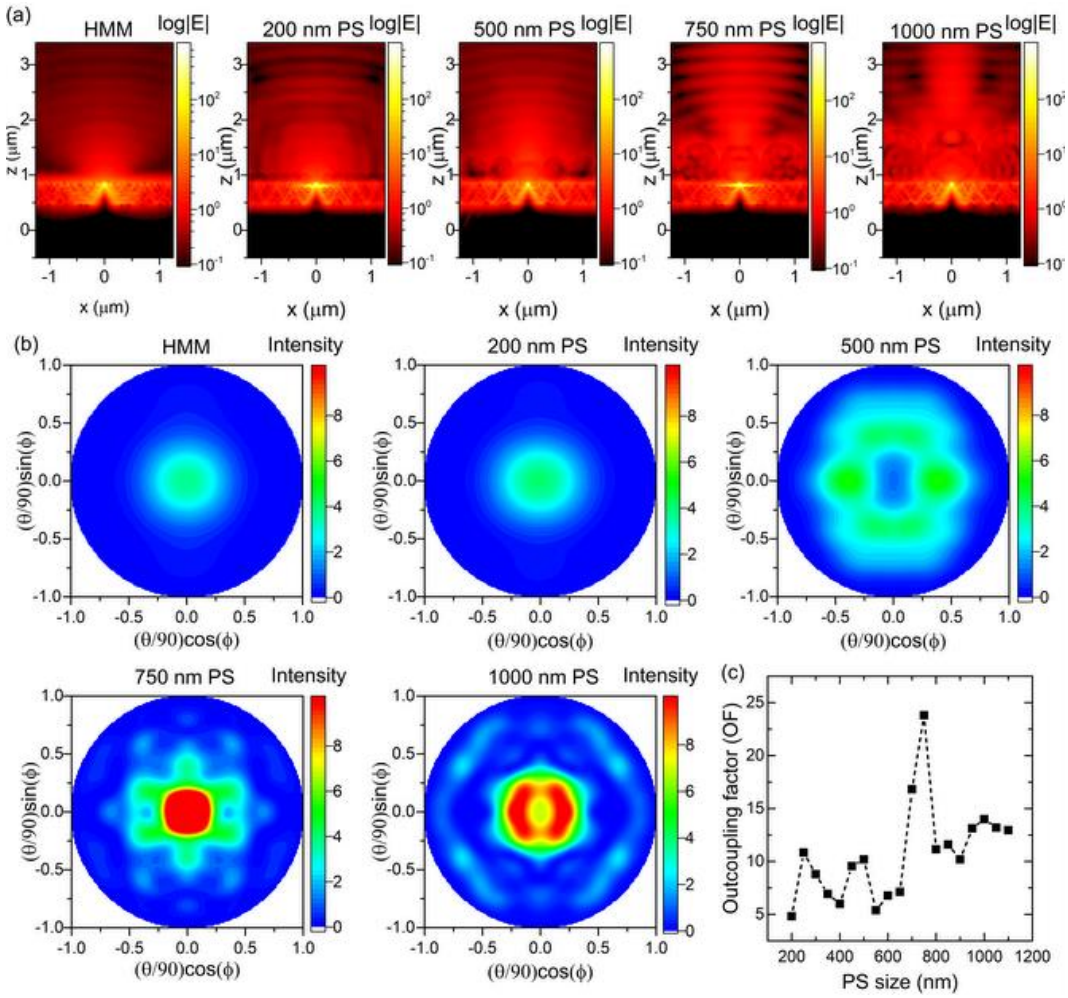

Figure 5.5. (a) Cross-sectional electric field profiles of plane HMM and HMM with 200, 500, 750 and 1000 nm polystyrene microbead assembly along with (b) contour far-field intensity profiles showing a very strong intensity of HMM with 750 nm PS microbead diameter. (c) Out-coupling factor with respect to PS microbead assembly.

Since the light trapped within the HMM acts as a waveguide, it reflects on both the top and bottom surfaces of HMM and the light outcoupling occurs at all the interfaces across the arrays. The far-field electric field distribution at x-y plane depicts such effects in relative to a plane HMM. The tunability in out-coupling factor is possible by varying the diameter of the spheres, which affects the optical length difference of the original light and the reflected light. By tuning the diameter of the PS microbeads, the maximum out-coupling factor of ~25 times was achieved at the sphere diameter of 750 nm which lies within the range of our experiments.

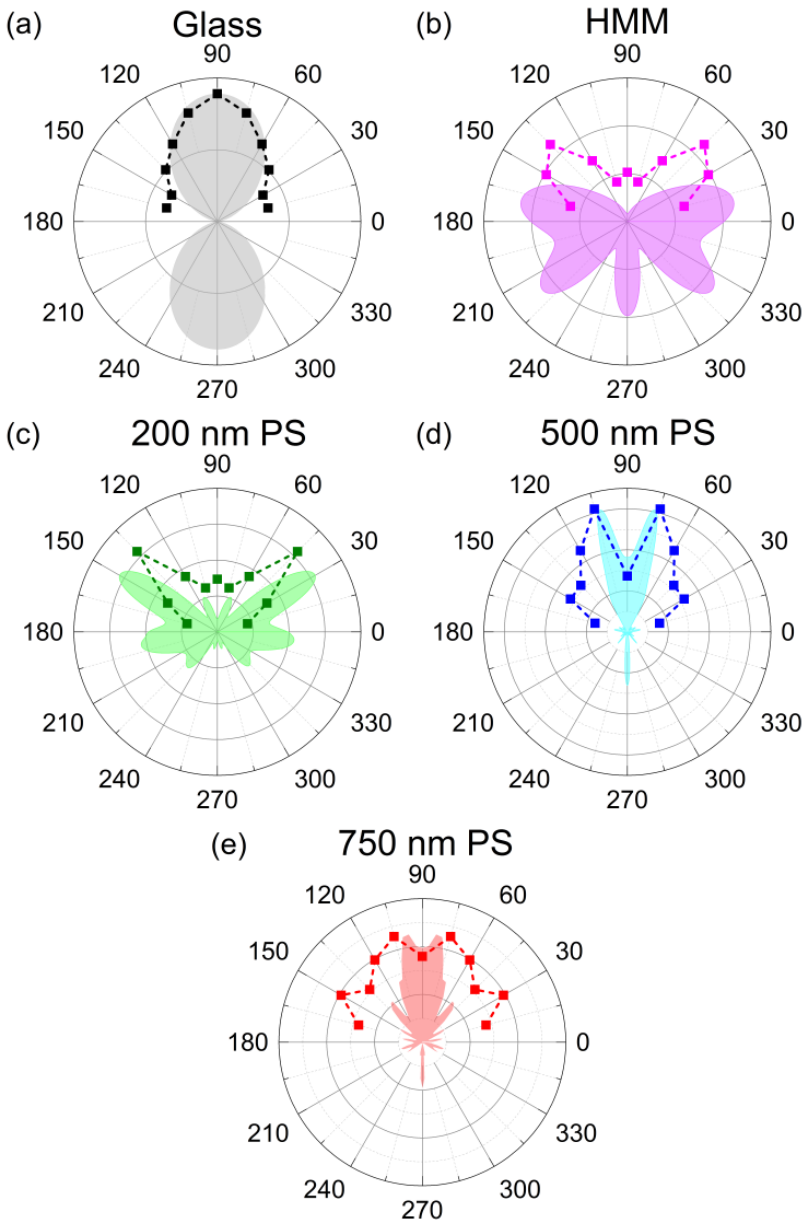

Figure 5.6. Simulated (shaded) and measured (dotted) scattering intensity plots of quantum dots spin-coated over a (a) glass, (b) HMM, HMM with self-assembled polystyrene monolayer of (c) 200 nm, (d) 500 nm, and (e) 750 nm..

Figure 5.6 summarizes the measured and simulated far-field emission profile of a dipole on HMMs. The calculated results average the emission from the dipole emitters of three different polarizations. For PL measurement, the emission within a collection angle of 120° was collected by the lens to contribute to the QD emission enhancement. To evaluate the angle-dependent emission intensity and the light outcoupling efficiency, we measured the scattering profile by exciting the sample with a 405 nm laser and analyzed the emission collected by a variable-angle detector from 0 to 180° with a step size of 15° angle. We detected negligible QD emission intensity within the collection angle from a plane HMM because of the lack of outcoupling as shown in Figure 5.6(b). Figures 5.6(c-e) show that the presence of nanoparticle monolayer improves the emission directionality. The effect becomes more observable as the particle size increases. The experimental measurements agree well with the simulated patterns, and any possible deviation is accounted for random QD orientation.

5.4 Summary

In conclusion, we experimentally and theoretically verified that reducing the unit cell thickness of a multilayer HMM increases the enhancement of QD emission. We successfully demonstrated a simple light outcoupling approach using a large-area self-assembled microbead layer. We found a 40-fold enhancement of QDs over a large area, higher than the ones previously obtained using plasmonic arrays and nanoparticles. Our study will benefit the applications in light-emitting devices and quantum electrodynamics.

CHAPTER 6. CARBON DOT-PLASMON COUPLING FOR MICROLED DISPLAY ENHANCEMENT AND CONTROL OF UV EXCITATION LEAKAGE

6.1 Introduction

Gallium-nitride-based (GaN) light-emitting diodes (LEDs) have attracted much attention because of their low power consumption, long device lifetime, low cost, and high brightness for applications such as backlight units in liquid crystal displays[166-171] and visible light communications[172-179]. Recently, GaN-based backlight LEDs have been extensively used as promising candidates for microLED display technology. MicroLED display carries an advantage of photoluminescence (PL), which is the emission is obtained with an electromagnetic wave input rather than electrical input utilized for OLED and QLED display technologies. This leads to a very large color gamut thus pushing the envelope of display technology.

In the past, CdSe based quantum dots have been applied for micro-LEDs for reduction in optical cross-talk and control of excitation light leakage. However, the techniques implemented needs additional processing of depositing the dielectric multi-layers, thus creating a Bragg reflector which hase a high reflectivity at UV regime and a large transmission at visible wavelengths[180,181]. In addition, there exist no attempts in creating cadmium-free emissive layers due to lack of their efficiency.

In this work, we utilize carbon dot (CD) emissive layers and experimentally demonstrate the use of Ag plasmonic nanoparticles to enhance the PL of CDs while

minimizing the leakage of excitation light. Conventional microLEDs utilize the multi-layered filters to minimize the leakage and may reduce the PL of emissive layers as well, with no technique incorporated for PL enhancement. The fluorescence emission can be improved by incorporating 30 nm Ag nanoparticles which absorbs the excitation light and enhance the PL at the same time.

The PL enhancement follows the excitation enhancement route as indicated in the schematic of Figure 6.1. In short, the 400 nm light excited using GaN backlight LED excites the CDs and also couples with the Ag nanoparticles. The localized surface plasmons created using through the 400 nm excitation acts as an additional source for CDs, leading to an enhanced emission. At same time, due to the formation of surface plasmons, the additional light gets coupled with nanoparticles and minimize its leakage to the far-field. In the absence of plasmonic nanoparticles, the additional excitation from the source may leak out of the CD film leading to leakage and poor image quality. Ag nanoparticles serve as excellent blocking agents and lead to a broadband enhancement of CDs. This technique offers a low-cost and effective approach to improve the performance of microLED displays.

6.2 Experimental Section

6.2.1 Synthesis of Carbon Dots (CDs)

The carbon dots were synthesized based on the method reported by Jinyang et al[182]. In short, 500 mg of citric acid and 1g of urea were dissolved in 10 mL ethanol solution, and then the solution was transferred into a 30 mL Teflon-line stainless steel autoclave.

The sealed autoclave was heated at 180 °C for 8 hours. Then the as obtained CDs were purified by ethanol water solution, and the precipitates were collected and re-dispersed in DI water. The emission of carbon dots is indicated in figure 6.1 (b).

6.2.2 Synthesis of Ag Nanoparticles

Ag nanoparticles were synthesized based on chemical reduction method[183]. Two reductants sodium borohydride ($NaBH_4$) and trisodium citrate (TSC) were used as primary reductant and stabilizing agents, respectively. The procedure is as follows: 48 mL of aqueous solution containing 1mM of NaBH4 and 4 mM of TSC is stirred at 60 °C for 30 min. Then, 2 mL aqueous silver nitrate ($AgNO_3$) solution (4 mM) was added drop-wise while the temperature is raised to 90 °C. Within 3 min the color of solution starts changing from transparent to dark yellow. The reaction was stopped and the beaker is allowed to cool down in the dark at room temperature followed by purification with a centrifuge. The Ag NP suspension is centrifuged three times (9000 rpm, 10 min) and the obtained powder is suspended in DI water and stored at 4 °C in the dark for future use. The obtained Ag NPs show the absorbance spectra peaking at 400 nm as shown in Figure 6.1(b), thus estimating its size to be 30 nm. After they are dispersed in CD polymer solution the resonance spectra red-shifts peaking at 420 nm wavelength.

6.2.3 Fabrication of MicroLED

The commercially available GaN-based UV LED chip with emission wavelength of 400 nm and is encapsulated by a transparent polymer, was utilized as an excitation source for microLED. An optically insulating silicone polymer well was attached over the excitation source followed by drop casting the emission layer for further measurements using Ocean Optics USB4000 spectrometer.

6.3 Results and Discussions

As shown in Figure 6.1(a), 15 ug/mL of CD is dispersed in 300 mg/mL PVP in ethanol for drop casting in the silicon polymer well to form a ~400 μm thick film. However, due to the transparency of the film, there exists a strong transmission through it leading to a heavy leakage and a relatively negligible emission of CDs. Ag nanoparticles are introduced to minimize the leakage and enhance the emission simultaneously as shown in the schematic of Figure 6.1(a). This mechanism of CD enhancement follows the excitation rate enhancement as reported in the past. The inset of Figure 6.1(a) shows the block diagram of the CD enhancement. In short, the UV source from the GaN chip acts as excitation for the CDs as well as the additional source of energy for CD enhancement. Since the absorption of Ag nanoparticles lies in the UV region, it blocks the UV light from leaking through the film.

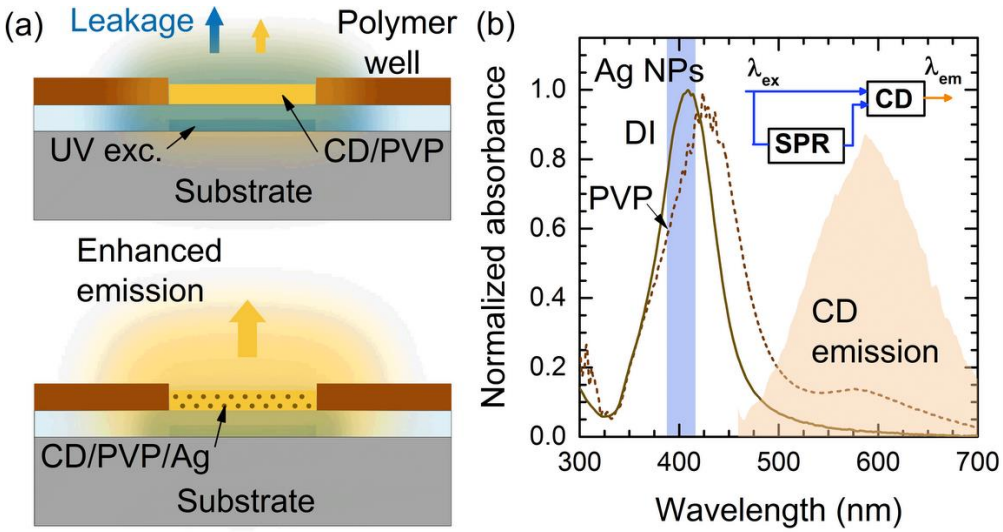

Figure 6.1. (a) Schematics of microLED chip with and without nanoparticles indicating the presence of leakage and an eventual emission enhancement after adding nanoparticles. The GaN-based LED is encapsulated with polymer layer followed by formation of silicon-based polymer well for drop casting of the emissive layer. (b) Measured normalized absorbance spectra of 30 nm silver nanoparticles dispersed in DI water and 300 mg/mL PVP solution leading to a redshift. The blue color faded region indicates the excitation range and the yellow color faded spectra indicates the emission of CDs.

Figure 6.2 shows the working of CD enhancement and UV leakage control. As the concentration of Ag nanoparticles in the film is increased from 0 to 3.125 nM, we found a maximum enhancement of 3.68 times at 1.25 nM of Ag nanoparticles. As the nanoparticle concentration is increased even more, the leakage of UV reduces to zero while the emission enhancement of 2 times is still observed. Although a similar

enhancement was previously reported in OLEDs and QLEDs, the electroluminescence spectrum was found to be different from photoluminescence spectrum. In this microLED, the PL spectrum in the solution and on the UV chip was found to be the same with an additional 2-fold enhancement. As of our knowledge, this research is first to report the use of surface plasmonic nanoparticles for completely reducing the UV leakage to zero and demonstrate an additional enhancement. The measured PL spectra of microLED at various Ag nanoparticle concentrations is shown in Figure 6.2(b). As the concentration is increased, the intensity of UV wavelength keeps reducing while a different behavior exists for CD enhancement. The CD enhancement factor is determined by the ratio of CD emission with and without Ag nanoparticles. At first, the enhancement factor increases because the Ag nanoparticles are too far away for enhancement to occur, and after a certain concentration, the enhancement factor reduces from 3.68 to 2 times due to the blocking of emission light as result of excessive metal nanoparticles in the film. However, the metal nanoparticles hold the capacity of broadband enhancement and reduce the UV leakage, thus avoiding the additional processing of filters/Bragg's reflector deposition.

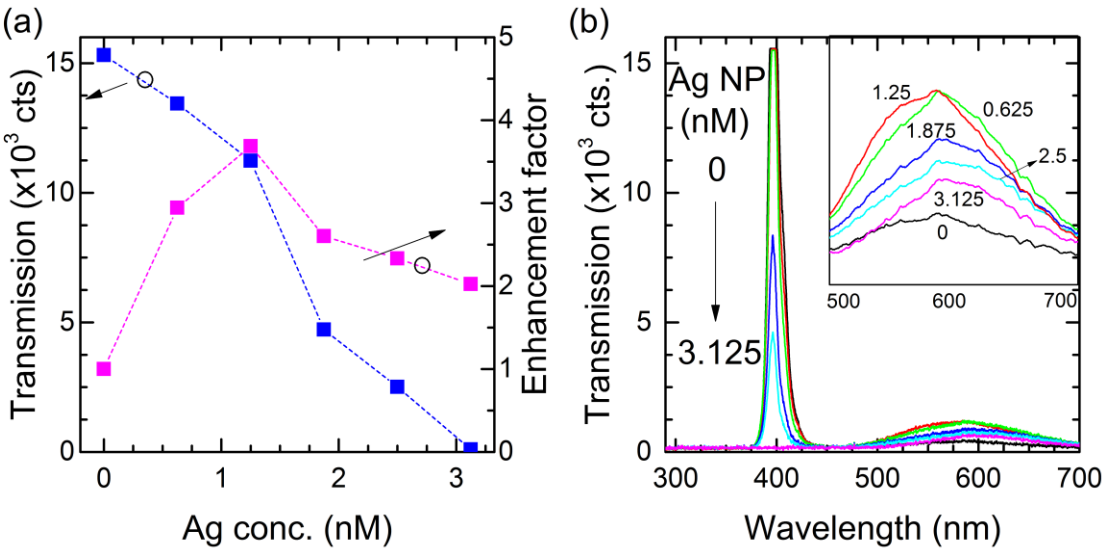

Figure 6.2. (a) Transmission and enhancement factors of CD emissive layer while increasing the Ag nanoparticle concentration. A maximum enhancement of 3.68 times is observed minimizing leakage by ~25%. The concentration at which the leakage becomes zero is found to have 2-fold emission enhancement. (b) Spectra indicating the transmission in UV regime and photoluminescence of CD (inset) at Ag concentrations increasing from 0 to 3.125 nM.

The bird-eye image of GaN-based UV LED chip is shown in the Figure 6.3(a) and Figure 6.3(b) shows the bird-eye image of enhanced CD based microLED with 8.5V and 0.5 A electrical input. The microscopic images of UV excitation and microLED is shown in Figure 6.3(c-d). Such a bright emission by an excitation source of 1mm X 1mm shows the efficiency of cadmium-free emissive material utilized here and its fit for display technology. Finally, the CIE chromaticity diagram of the excitation and

emission light is indicated in Figure 6.4 showing that the device is suitable for CMYK-based microLED display technology.

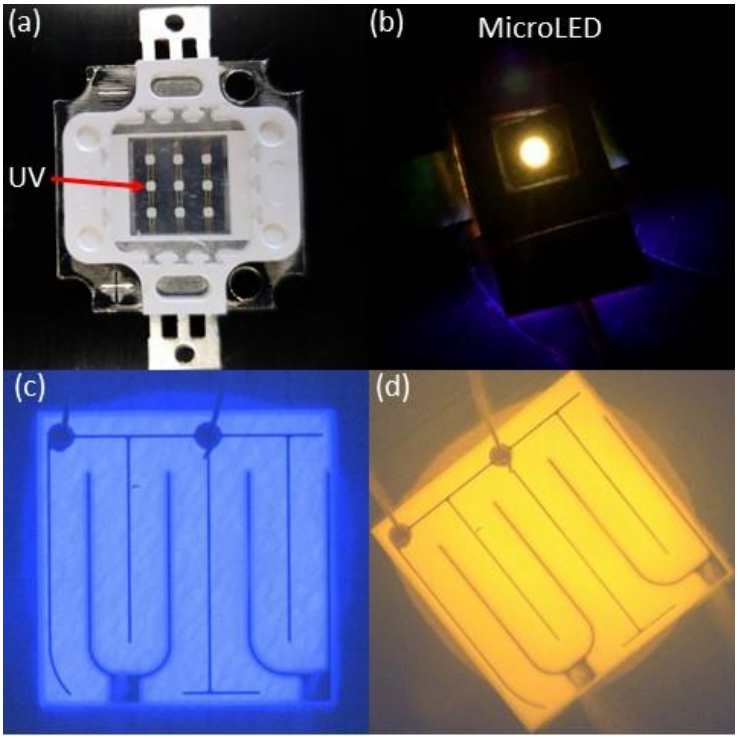

Figure 6.3. (a) Bird-eye image of GaN-based UV LED chip with 9 LEDs of dimensions 1 mm X 1 mm. (b) Enhanced microLED with zero UV leakage, made over the center UV LED. Microscopic view of LEDs (c) with and (d) without the emissive layer. This comparison shows the efficiency of UV leakage minimization with Ag nanoparticles.

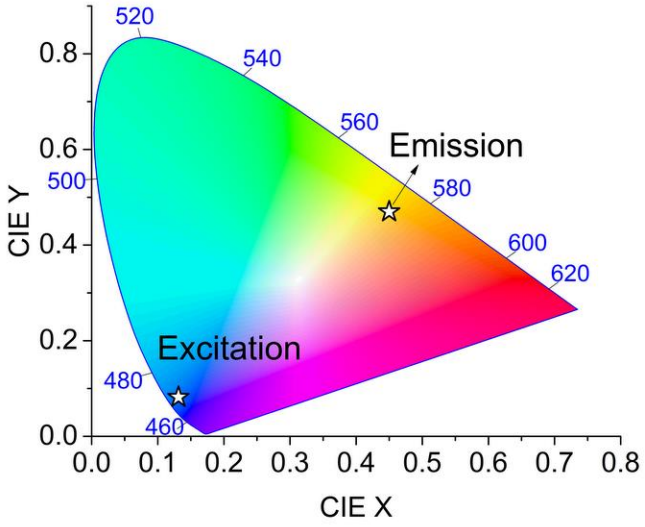

Figure 6.4. CIE chromaticity diagram of the excitation and emission light showing the suitability of CD-based microLED for CMYK based display technology.

6.4 Summary

In conclusion, we demonstrate a novel approach to enhance the performance of microLED by introducing Ag plasmonic nanoparticles to simultaneously enhance the emission of carbon dots (CDs) and suppress the leakage of excitation light. The cadmium free emissive layers have not been demonstrated in the past due to their weak emissive efficiencies. We incorporated metal nanoparticles in the emissive layer to enhance microLED by 2 times. Such an enhancement lies within the range of other QD LED display devices. This multi-featured emissive layer serves as a PL enhancer and an excitation blocker without the need of additional filters. This innovative approach could lead to efficient and cost-effective displays.

CHAPTER 7. CONCLUSIONS

In conclusion, we presented a novel fabrication technique called metal-assisted focused-ion beam nanopatterning for manufacturing of high precision photonic and plasmonic nanostructures. This technique allows the manufacturing of molds for nanoimprint lithography thus making it practical for industrial biosensing applications. We demonstrated its use in making gold and silver plasmonic arrays for achieving a very high quantum dot enhancement and then further implementing these structures for biosensing. The enhancement factors achieved using silver open-ring nanoarrays are found to be more than 100 times with an estimated quantum efficiency exceeding 99%. Further, the broadband enhancement of these nanostructures was utilized for DNA sensing to enhance the limit-of-detection by four orders of magnitude. This design is expected to find a major scope in compact DNA sensing and may serve as a platform for other biosensing technologies.

Further, we introduced aluminum dimple arrays for demonstrating the UV plasmonic systems which were sidelined as the field enhancements using aluminum was typically weak. However, through the designed aluminum dimple arrays, we demonstrate enhancement of multi-colors, in other words, broadband enhancement by using the different route of enhancement. According to this route, we utilize the incident UV light for creating surface plasmon resonance in UV regime which in turn acts as a secondary excitation source for quantum dots leading to enhancement of green and red

colors. Such a design is expected to improve the efficiency is solar cells, and the mechanism was implemented in microLED display in chapter 6.

To demonstrate, the enhancement through hyperbolic metamaterials (HMM), we first studied the effect of unit cell thickness over quantum dot enhancement and found that the Purcell factors increase at smallest unit cell thickness due to an increase in HMM modes which provide additional decay pathways for quantum dots and thus reduce the fluorescence lifetime. In addition, we demonstrate a novel polystyrene microbead based photonic crystal for outcoupling of high-k waves trapped within the HMM, thus eventually leading to a maximum enhancement of 40 times. This study is expected to find several applications in optoelectronic devices and biosensing devices which specifically require an enhancement in large areas.

Finally, our demonstration of microLED display has many features such as: utilizing cadmium free emissive materials, minimizing the UV leakage through the device, and enhancement of emission by 2 times. Such a multi-featured device will be much useful for creating a CMYK based display devices.

In summary, our work of integrating surface plasmonic materials for broadband enhancement, DNA sensing, HMMs, and microLED displays, has successfully extended the scope of plasmonic and photonic technologies. However, some improvements in the future would be necessary for the design of compact sensing, large area microLED display devices with additional colors of emissive materials included and implementing of UV plasmonic devices for solar cells will push the technology envelope to next level.

References

[1] Spanhel, Lubomir, Markus Haase, Horst Weller, and Arnim Henglein. "Photochemistry of colloidal semiconductors. 20. Surface modification and stability of strong luminescing CdS particles." Journal of the American Chemical Society 109, no. 19 (1987): 5649-5655.

[2] Kortan, A. R., R. Hull, Robert L. Opila, Moungi G. Bawendi, Michael L. Steigerwald, P. J. Carroll, and Louis E. Brus. "Nucleation and growth of CdSe on ZnS quantum crystallite seeds, and vice versa, in inverse micelle media." Journal of the American Chemical Society 112, no. 4 (1990): 1327-1332.

[3] Murray, CBea, David J. Norris, and Moungi G. Bawendi. "Synthesis and characterization of nearly monodisperse CdE (E= sulfur, selenium, tellurium) semiconductor nanocrystallites." Journal of the American Chemical Society 115, no. 19 (1993): 8706-8715.

[4] NeiláFurlong, D. "Size-quantised semiconductor cadmium chalcogenide particles in Langmuir–Blodgett films." Journal of the Chemical Society, Faraday Transactions 88, no. 15 (1992): 2207-2214.

[5] Sundaram, Mani, Scott A. Chalmers, Peter F. Hopkins, and Arthur C. Gossard. "New quantum structures." Science 254, no. 5036 (1991): 1326-1335.

[6] Cingolani, Roberto, and Klaus Ploog. "Frequency and density dependent radiative recombination processes in III–V semiconductor quantum wells and superlattices." Advances in Physics 40, no. 5 (1991): 535-623.

[7] Alivisatos, A. Paul. "Semiconductor clusters, nanocrystals, and quantum dots." science 271, no. 5251 (1996): 933-937.

[8] Klimov, V. I., A. A. Mikhailovsky, Su Xu, A. Malko, J. A. Hollingsworth, A. CA Leatherdale, H-J. Eisler, and M. G. Bawendi. "Optical gain and stimulated emission in nanocrystal quantum dots." Science 290, no. 5490 (2000): 314-317.

[9] Artemyev, Mikhail V., Ulrike Woggon, Reinhold Wannemacher, Heiko Jaschinski, and Wolfgang Langbein. "Light trapped in a photonic dot: Microspheres act as a cavity for quantum dot emission." Nano letters 1, no. 6 (2001): 309-314.

[10] Graham-Rowe, Duncan. "From dots to devices." nature photonics 3, no. 6 (2009): 307.

[11] Coe-Sullivan, Seth. "Optoelectronics: Quantum dot developments." Nature Photonics 3, no. 6 (2009): 315-316.

[12] Han, Lili, Donghuan Qin, Xi Jiang, Yanshan Liu, Li Wang, Junwu Chen, and Yong Cao. "Synthesis of high quality zinc-blende CdSe nanocrystals and their application in hybrid solar cells." Nanotechnology 17, no. 18 (2006): 4736.

[13] Michler, P., A. Imamoğlu, M. D. Mason, P. J. Carson, G. F. Strouse, and S. K. Buratto. "Quantum correlation among photons from a single quantum dot at room temperature." Nature 406, no. 6799 (2000): 968.

[14] Cui, Dehu, Jian Xu, Ting Zhu, Gary Paradee, S. Ashok, and Michael Gerhold. "Harvest of near infrared light in PbSe nanocrystal-polymer hybrid photovoltaic cells." Applied Physics Letters 88, no. 18 (2006): 183111.

[15] O'Regan, Brian, Daniel T. Schwartz, S. Mohammed Zakeeruddin, and Michael Grätzel. "Electrodeposited Nanocomposite n–p Heterojunctions for Solid-State Dye-Sensitized Photovoltaics." Advanced Materials 12, no. 17 (2000): 1263-1267.

[16] Bereznev, S., I. Konovalov, A. Öpik, and J. Kois. "Hybrid CuInS2/polypyrrole and CuInS2/poly (3, 4-ethylenedioxythiophene) photovoltaic structures." Synthetic metals 152, no. 1-3 (2005): 81-84.

[17] Nozik, A. J. "Exciton multiplication and relaxation dynamics in quantum dots: applications to ultrahigh-efficiency solar photon conversion." Inorganic chemistry 44, no. 20 (2005): 6893-6899.

[18] Nozik, A. J. "Quantum dot solar cells." Physica E: Low-dimensional Systems and Nanostructures 14, no. 1-2 (2002): 115-120.

[19] Plass, Robert, Serge Pelet, Jessica Krueger, Michael Grätzel, and Udo Bach. "Quantum dot sensitization of organic− inorganic hybrid solar cells." The Journal of Physical Chemistry B 106, no. 31 (2002): 7578-7580.

[20] Lin, Sheng-Chih, Yuh-Lang Lee, Chi-Hsiu Chang, Yu-Jen Shen, and Yu-Min Yang. "Quantum-dot-sensitized solar cells: Assembly of CdS-quantum-dots coupling techniques of self-assembled monolayer and chemical bath deposition." Applied physics letters 90, no. 14 (2007): 143517.

21 Robel, István, Vaidyanathan Subramanian, Masaru Kuno, and Prashant V. Kamat. "Quantum dot solar cells. Harvesting light energy with CdSe nanocrystals molecularly linked to mesoscopic TiO2 films." Journal of the American Chemical Society 128, no. 7 (2006): 2385-2393.

[22] Diguna, Lina J., Qing Shen, Junya Kobayashi, and Taro Toyoda. "High efficiency of CdSe quantum-dot-sensitized Ti O 2 inverse opal solar cells." Applied Physics Letters 91, no. 2 (2007): 023116.

[23] Coe, Seth, Wing-Keung Woo, Moungi Bawendi, and Vladimir Bulović. "Electroluminescence from single monolayers of nanocrystals in molecular organic devices." Nature 420, no. 6917 (2002): 800.

[24] Cho, Kyung-Sang, Eun Kyung Lee, Won-Jae Joo, Eunjoo Jang, Tae-Ho Kim, Sang Jin Lee, Soon-Jae Kwon et al. "High-performance crosslinked colloidal quantum-dot light-emitting diodes." Nature Photonics 3, no. 6 (2009): 341.

[25] Sun, Qingjiang, Y. Andrew Wang, Lin Song Li, Daoyuan Wang, Ting Zhu, Jian Xu, Chunhe Yang, and Yongfang Li. "Bright, multicoloured light-emitting diodes based on quantum dots." Nature photonics 1, no. 12 (2007): 717.

[26] Colvin, V. L., M. C. Schlamp, and A. Paul Alivisatos. "Light-emitting diodes made from cadmium selenide nanocrystals and a semiconducting polymer." Nature 370, no. 6488 (1994): 354.

[27] Caruge, J. M., J. Eugene Halpert, V. Wood, V. Bulović, and M. G. Bawendi. "Colloidal quantum-dot light-emitting diodes with metal-oxide charge transport layers." Nature photonics 2, no. 4 (2008): 247.

[28] Zhu, T., K. Shanmugasundaram, S. C. Price, J. Ruzyllo, F. Zhang, J. Xu, S. E. Mohney, Q. Zhang, and A. Y. Wang. "Mist fabrication of light emitting diodes with colloidal nanocrystal quantum dots." Applied Physics Letters 92, no. 2 (2008): 023111.

[29] Kobayashi, Satoshi, Yuki Tani, and Hiroshi Kawazoe. "Quantum dot activated all-inorganic electroluminescent device fabricated using solution-synthesized CdSe/ZnS nanocrystals." Japanese Journal of Applied Physics 46, no. 10L (2007): L966.

[30] Taylor, R. M., K. H. Church, and M. I. Sluch. "Red light emission from hybrid organic/inorganic quantum dot AC light emitting displays." Displays 28, no. 2 (2007): 92-96.

[31] Dabbousi, B. O., M. G. Bawendi, O. Onitsuka, and M. F. Rubner. "Electroluminescence from CdSe quantum-dot/polymer composites." Applied Physics Letters 66, no. 11 (1995): 1316-1318.

[32] Yang, Heesun, and Paul H. Holloway. "Electroluminescence from hybrid conjugated polymer− CdS: Mn/ZnS core/shell nanocrystals devices." The Journal of Physical Chemistry B 107, no. 36 (2003): 9705-9710.

[33] Medintz, Igor L., Aaron R. Clapp, Hedi Mattoussi, Ellen R. Goldman, Brent Fisher, and J. Matthew Mauro. "Self-assembled nanoscale biosensors based on quantum dot FRET donors." Nature materials 2, no. 9 (2003): 630.

[34] Sapsford, Kim E., Thomas Pons, Igor L. Medintz, and Hedi Mattoussi. "Biosensing with luminescent semiconductor quantum dots." Sensors 6, no. 8 (2006): 925-953.

[35] Gao, Xiaohu, and Shivang R. Dave. "Quantum dots for cancer molecular imaging." In Bio-applications of Nanoparticles, pp. 57-73. Springer, New York, NY, 2007.

[36] Smith, Andrew M., Hongwei Duan, Aaron M. Mohs, and Shuming Nie. "Bioconjugated quantum dots for in vivo molecular and cellular imaging." Advanced drug delivery reviews 60, no. 11 (2008): 1226-1240.

[37] Jaiswal, Jyoti K., Ellen R. Goldman, Hedi Mattoussi, and Sanford M. Simon. "Use of quantum dots for live cell imaging." Nature methods 1, no. 1 (2004): 73.

[38] Gao, Xiaohu, Lily Yang, John A. Petros, Fray F. Marshall, Jonathan W. Simons, and Shuming Nie. "In vivo molecular and cellular imaging with quantum dots." Current opinion in biotechnology 16, no. 1 (2005): 63-72.

[39] Smith, Andrew M., Shivang Dave, Shuming Nie, Lawrence True, and Xiaohu Gao. "Multicolor quantum dots for molecular diagnostics of cancer." Expert review of molecular diagnostics 6, no. 2 (2006): 231-244.

[40] Kumar, Sonia, and Rebecca Richards-Kortum. "Optical molecular imaging agents for cancer diagnostics and therapeutics." (2006): 23-30.

[41] Li, Zi-Bo, Weibo Cai, and Xiaoyuan Chen. "Semiconductor quantum dots for in vivo imaging." Journal of nanoscience and nanotechnology 7, no. 8 (2007): 2567-2581.

[42] Parak, Wolfgang J., Teresa Pellegrino, and Christian Plank. "Labelling of cells with quantum dots." Nanotechnology 16, no. 2 (2005): R9.

[43] WANG, Yang, Yu-Lin DENG, Hong QING, and Hai-Yan XIE. "Advance in Real-time and Dynamic Biotracking and Bioimaging Based on Quantum Dots [J]." Chemical Journal of Chinese Universities 4 (2008): 001.

[44] Sharma, Parvesh, Scott Brown, Glenn Walter, Swadeshmukul Santra, and Brij Moudgil. "Nanoparticles for bioimaging." Advances in colloid and interface science 123 (2006): 471-485.

[45] Wang, Congjun, Brian L. Wehrenberg, Chui Y. Woo, and Philippe Guyot-Sionnest. "Light emission and amplification in charged CdSe quantum dots." The Journal of Physical Chemistry B 108, no. 26 (2004): 9027-9031.

[46] Klimov, Victor I., Sergei A. Ivanov, Jagjit Nanda, Marc Achermann, Ilya Bezel, John A. McGuire, and Andrei Piryatinski. "Single-exciton optical gain in semiconductor nanocrystals." Nature 447, no. 7143 (2007): 441.

[47] Roy Choudhury, K., Yudhisthira Sahoo, and Paras N. Prasad. "Hybrid Quantum-Dot–Polymer Nanocomposites for Infrared Photorefractivity at an Optical Communication Wavelength." Advanced materials 17, no. 23 (2005): 2877-2881.

[48] Kim, Sungjee, Brent Fisher, Hans-Jürgen Eisler, and Moungi Bawendi. "Type-II quantum dots: CdTe/CdSe (core/shell) and CdSe/ZnTe (core/shell) heterostructures." Journal of the American Chemical Society 125, no. 38 (2003): 11466-11467.

[49] Barnes, William L. "Surface plasmon–polariton length scales: a route to sub-wavelength optics." Journal of optics A: pure and applied optics 8, no. 4 (2006): S87.

[50] Matsubara, Koji, Satoshi Kawata, and Shigeo Minami. "Optical chemical sensor based on surface plasmon measurement." Applied Optics 27, no. 6 (1988): 1160-1163.

[51] Otto, Andreas. "Excitation of nonradiative surface plasma waves in silver by the method of frustrated total reflection." Zeitschrift für Physik A Hadrons and nuclei 216, no. 4 (1968): 398-410.

[52] Harris, R. D., and James S. Wilkinson. "Waveguide surface plasmon resonance sensors." Sensors and Actuators B: Chemical 29, no. 1-3 (1995): 261-267.

[53] Ritchie, R. H., E. T. Arakawa, J. J. Cowan, and R. N. Hamm. "Surface-plasmon resonance effect in grating diffraction." Physical Review Letters 21, no. 22 (1968): 1530.

[54] Renger, Jan, Romain Quidant, Niek van Hulst, Stefano Palomba, and Lukas Novotny. "Free-space excitation of propagating surface plasmon polaritons by nonlinear four-wave mixing." Physical review letters 103, no. 26 (2009): 266802.

[55] Maier, Stefan Alexander. Plasmonics: fundamentals and applications. Springer Science & Business Media, 2007.

[56] Liang, Zhiqiang, Jun Sun, Yueyue Jiang, Lin Jiang, and Xiaodong Chen. "Plasmonic enhanced optoelectronic devices." Plasmonics 9, no. 4 (2014): 859-866.

[57] Rifat, Ahmmed A., G. A. Mahdiraji, Yong Meng Sua, Rajib Ahmed, Y. G. Shee, and FR Mahamd Adikan. "Highly sensitive multi-core flat fiber surface plasmon resonance refractive index sensor." Optics express 24, no. 3 (2016): 2485-2495.

[58] Geddes, Chris D. "Metal-enhanced fluorescence nanoparticles." U.S. Patent 9,023,372, issued May 5, 2015.

[59] Ayala-Orozco, Ciceron, Jun G. Liu, Mark W. Knight, Yumin Wang, Jared K. Day, Peter Nordlander, and Naomi J. Halas. "Fluorescence enhancement of molecules inside a gold nanomatryoshka." Nano letters 14, no. 5 (2014): 2926-2933.

[60] Masango, Sicelo S., Ryan A. Hackler, Nicolas Large, Anne-Isabelle Henry, Michael O. McAnally, George C. Schatz, Peter C. Stair, and Richard P. Van Duyne. "High-resolution distance dependence study of surface-enhanced Raman scattering enabled by atomic layer deposition." Nano letters 16, no. 7 (2016): 4251-4259.

[61] Nguyen, Hoang Hiep, Jeho Park, Sebyung Kang, and Moonil Kim. "Surface plasmon resonance: a versatile technique for biosensor applications." Sensors 15, no. 5 (2015): 10481-10510.

[62] Bauch, Martin, Koji Toma, Mana Toma, Qingwen Zhang, and Jakub Dostalek. "Plasmon-enhanced fluorescence biosensors: a review." Plasmonics 9, no. 4 (2014): 781-799.

[63] Huang, Chun Jen, Jakub Dostalek, and Wolfgang Knoll. "Optimization of layer structure supporting long range surface plasmons for surface plasmon-enhanced fluorescence spectroscopy biosensors." Journal of Vacuum Science & Technology B, Nanotechnology and Microelectronics: Materials, Processing, Measurement, and Phenomena 28, no. 1 (2010): 66-72.

[64] Tawa, Keiko, Yoshiki Yokota, Kenji Kintaka, Junji Nishii, and Takahiko Nakaoki. "An application of a plasmonic chip with enhanced fluorescence to a simple biosensor with extended dynamic range." Sensors and Actuators B: Chemical 157, no. 2 (2011): 703-709.

[65] Yuk, Jong Seol, Brian D. MacCraith, and Colette McDonagh. "Signal enhancement of surface plasmon-coupled emission (SPCE) with the evanescent field of surface plasmons on a bimetallic paraboloid biochip." Biosensors and Bioelectronics 26, no. 7 (2011): 3213-3218.

[66] Nooney, Robert, Andrew Clifford, Xavier LeGuevel, Ondrej Stranik, Colette McDonagh, and Brian D. MacCraith. "Enhancing the analytical performance of immunoassays that employ metal-enhanced fluorescence." Analytical and bioanalytical chemistry 396, no. 3 (2010): 1127-1134.

[67] Zhou, Liangcheng, Fei Ding, Hao Chen, Wei Ding, Weihua Zhang, and Stephen Y. Chou. "Enhancement of immunoassay's fluorescence and detection sensitivity using three-dimensional plasmonic nano-antenna-dots array." Analytical chemistry 84, no. 10 (2012): 4489-4495.

[68] Luan, Jingyi, Jeremiah J. Morrissey, Zheyu Wang, Hamed Gholami Derami, Keng-Ku Liu, Sisi Cao, Qisheng Jiang et al. "Add-on Plasmonic Patch as a Universal Fluorescence Enhancer." (2018).

[69] Li, Sijin, Tong Si, Meng Wang, and Huimin Zhao. "Development of a synthetic malonyl-CoA sensor in Saccharomyces cerevisiae for intracellular metabolite monitoring and genetic screening." ACS synthetic biology 4, no. 12 (2015): 1308-1315.

[70] Ramírez, Juan Carlos, Carolina Inés Cura, Otacilio da Cruz Moreira, Eliane Lages-Silva, Natalia Juiz, Elsa Velázquez, Juan David Ramírez et al. "Analytical validation of quantitative real-time PCR methods for quantification of Trypanosoma cruzi DNA in blood samples from Chagas disease patients." The Journal of Molecular Diagnostics 17, no. 5 (2015): 605-615.

[71] Holt, Allison, Sharon Chao Wootton, Julio J. Mulero, Pius M. Brzoska, Emanuel Langit, and Robert L. Green. "Developmental validation of the Quantifiler® HP and Trio Kits for human DNA quantification in forensic samples." Forensic Science International: Genetics 21 (2016): 145-157.

[72] Patolsky, Fernando, Amir Lichtenstein, and Itamar Willner. "Detection of single-base DNA mutations by enzyme-amplified electronic transduction." Nature biotechnology 19, no. 3 (2001): 253.

[73] Su, Qiang, Daniel Wesner, Holger Schönherr, and Gilbert Nöll. "Molecular beacon modified sensor chips for oligonucleotide detection with optical readout." Langmuir 30, no. 47 (2014): 14360-14367.

[74] Molesky, Sean, Christopher J. Dewalt, and Zubin Jacob. "High temperature epsilon-near-zero and epsilon-near-pole metamaterial emitters for thermophotovoltaics." Optics express 21, no. 101 (2013): A96-A110.

[75] Molesky, Sean, Christopher J. Dewalt, and Zubin Jacob. "High temperature epsilon-near-zero and epsilon-near-pole metamaterial emitters for thermophotovoltaics." Optics express 21, no. 101 (2013): A96-A110.

[76] Galfsky, T., H. N. S. Krishnamoorthy, W. Newman, E. E. Narimanov, Z. Jacob, and V. M. Menon. "Active hyperbolic metamaterials: enhanced spontaneous emission and light extraction." Optica 2, no. 1 (2015): 62-65.

[77] Le-Van, Quynh, Xavier Le Roux, Abdelhanin Aassime, and Aloyse Degiron. "Electrically driven optical metamaterials." Nature communications 7 (2016): 12017.

[78] Kim, Na-Yeong, Sang-Hyun Hong, Jang-Won Kang, NoSoung Myoung, Sang-Youp Yim, Suhyun Jung, Kwanghee Lee, Charles W. Tu, and Seong-Ju Park. "Localized surface plasmon-enhanced green quantum dot light-emitting diodes using gold nanoparticles." RSC Advances 5, no. 25 (2015): 19624-19629.

[79] Huh, Chul, Chel-Jong Choi, Wanjoong Kim, Bong Kyu Kim, Byoung-Jun Park, Eun-Hye Jang, Sang-Hyeob Kim, and Gun Yong Sung. "Enhancement in light emission

efficiency of Si nanocrystal light-emitting diodes by a surface plasmon coupling." Applied Physics Letters 100, no. 18 (2012): 181108.

[80] Chen, Jing, Qianqian Huang, Qing Guo Du, Dewei Zhao, Feng Xu, Jiangyong Pan, Wei Lei, and Arokia Nathan. "Localized surface plasmon resonance enhanced quantum dot light-emitting diodes via quantum dot-capped gold nanoparticles." RSC Advances 4, no. 101 (2014): 57574-57579.

[81] Yang, Xuyong, Pedro Ludwig Hernandez-Martinez, Cuong Dang, Evren Mutlugun, Kang Zhang, Hilmi Volkan Demir, and Xiao Wei Sun. "Electroluminescence efficiency enhancement in quantum dot light-emitting diodes by embedding a silver nanoisland layer." Advanced Optical Materials 3, no. 10 (2015): 1439-1445.

[82] Kim, Beak-Hyun, Chang-Hee Cho, Jin-Soo Mun, Min-Ki Kwon, Tae-Young Park, Jong Su Kim, Clare Chisu Byeon, Jongmin Lee, and Seong-Ju Park. "Enhancement of the external quantum efficiency of a silicon quantum dot light-emitting diode by localized surface plasmons." Advanced Materials 20, no. 16 (2008): 3100-3104.

[83] Leck, Kheng Swee, Yoga Divayana, Dewei Zhao, Xuyong Yang, Agus Putu Abiyasa, Evren Mutlugun, Yuan Gao et al. "Quantum dot light-emitting diode with quantum dots inside the hole transporting layers." ACS applied materials & interfaces 5, no. 14 (2013): 6535-6540.

[84] Pan, Jiangyong, Jing Chen, Dewei Zhao, Qianqian Huang, Qasim Khan, Xiang Liu, Zhi Tao, Zichen Zhang, and Wei Lei. "Surface plasmon-enhanced quantum dot light-emitting diodes by incorporating gold nanoparticles." Optics express 24, no. 2 (2016): A33-A43.

[85] Kannegulla, Akash, Ye Liu, and Li-Jing Cheng. "Surface-plasmon-enhanced photoluminescence of quantum dots based on open-ring nanostructure array." In Quantum Dots and Nanostructures: Growth, Characterization, and Modeling XIII, vol. 9758, p. 97580B. International Society for Optics and Photonics, 2016.

[86] Tian, Jie, Wei Yan, Yazhao Liu, Jun Luo, Daozhong Zhang, Zhiyuan Li, and Min Qiu. "Optical quality improvement of Si photonic devices fabricated by focused-ion-beam milling." Journal of Lightwave Technology 27, no. 19 (2009): 4306-4310.

[87] Schrauwen, Jonathan, Frederik Van Laere, Dries Van Thourhout, and Roel Baets. "Focused-ion-beam fabrication of slanted grating couplers in silicon-on-insulator waveguides." IEEE Photonics Technology Letters 19, no. 11 (2007): 816-818.

[88] Smith, Cameron LC, Anil H. Thilsted, Cesar E. Garcia-Ortiz, Ilya P. Radko, Rodolphe Marie, Claus Jeppesen, Christoph Vannahme, Sergey I. Bozhevolnyi, and Anders Kristensen. "Efficient excitation of channel plasmons in tailored, UV-lithography-defined V-grooves." Nano letters 14, no. 3 (2014): 1659-1664.

[89] Bermúdez-Ureña, Esteban, Carlos Gonzalez-Ballestero, Michael Geiselmann, Renaud Marty, Ilya P. Radko, Tobias Holmgaard, Yury Alaverdyan et al. "Coupling of individual quantum emitters to channel plasmons." Nature communications 6 (2015): 7883.

[90] Chen, Zhao-xian, Zi-jian Wu, Yang Ming, Xue-jin Zhang, and Yan-qing Lu. "Hybrid plasmonic waveguide in a metal V-groove." AIP Advances 4, no. 1 (2014): 017103.

[91] Smith, Cameron LC, Boris Desiatov, Ilya Goykmann, Irene Fernandez-Cuesta, Uriel Levy, and Anders Kristensen. "Plasmonic V-groove waveguides with Bragg grating filters via nanoimprint lithography." Optics express 20, no. 5 (2012): 5696-5706.

[92] Blake, Adam, and Maxim Sukharev. "Surface plasmon polaritons in periodic arrays of V-shaped grooves strongly coupled to quantum emitters." Physical Review B 92, no. 3 (2015): 035433.

[93] Liu, Penghong, Xinzheng Zhang, Zenghong Ma, Wei Cai, Lei Wang, and Jingjun Xu. "Surface plasmon modes in graphene wedge and groove waveguides." Optics express 21, no. 26 (2013): 32432-32440.

[94] Gui, Chengcheng, and Jian Wang. "Wedge hybrid plasmonic THz waveguide with long propagation length and ultra-small deep-subwavelength mode area." Scientific reports 5 (2015): 11457.

[95] Aslan, Kadir, Ignacy Gryczynski, Joanna Malicka, Evgenia Matveeva, Joseph R. Lakowicz, and Chris D. Geddes. "Metal-enhanced fluorescence: an emerging tool in biotechnology." Current Opinion in Biotechnology 16, no. 1 (2005): 55-62.

[96] Deng, Wei, and Ewa M. Goldys. "Plasmonic approach to enhanced fluorescence for applications in biotechnology and the life sciences." Langmuir 28, no. 27 (2012): 10152-10163.

[97] Dulkeith, E., M. Ringler, T. A. Klar, J. Feldmann, A. Munoz Javier, and W. J. Parak. "Gold nanoparticles quench fluorescence by phase induced radiative rate suppression." Nano letters 5, no. 4 (2005): 585-589.

[98] Xu, Jing-Juan, Wei-Wei Zhao, Shiping Song, Chunhai Fan, and Hong-Yuan Chen. "Functional nanoprobes for ultrasensitive detection of biomolecules: an update." Chemical Society Reviews 43, no. 5 (2014): 1601-1611.

[99] Wilson, Robert. "The use of gold nanoparticles in diagnostics and detection." Chemical Society Reviews 37, no. 9 (2008): 2028-2045.

[100] Swierczewska, Magdalena, Seulki Lee, and Xiaoyuan Chen. "The design and application of fluorophore–gold nanoparticle activatable probes." Physical Chemistry Chemical Physics 13, no. 21 (2011): 9929-9941.

[101] Mei, Zhong, and Liang Tang. "Surface-plasmon-coupled fluorescence enhancement based on ordered gold nanorod array biochip for ultrasensitive DNA analysis." Analytical chemistry 89, no. 1 (2016): 633-639.

[102] Anger, Pascal, Palash Bharadwaj, and Lukas Novotny. "Enhancement and quenching of single-molecule fluorescence." Physical review letters 96, no. 11 (2006): 113002.

[103] Pompa, P. P., L. Martiradonna, A. Della Torre, F. Della Sala, L. Manna, M. De Vittorio, F. Calabi, R. Cingolani, and R. Rinaldi. "Metal-enhanced fluorescence of colloidal nanocrystals with nanoscale control." Nature nanotechnology 1, no. 2 (2006): 126.

[104] Belacel, Cherif, Benjamin Habert, Florian Bigourdan, François Marquier, J-P. Hugonin, S. Michaelis de Vasconcellos, Xavier Lafosse et al. "Controlling spontaneous emission with plasmonic optical patch antennas." Nano letters 13, no. 4 (2013): 1516-1521.

[105] Hwang, Ehren, Igor I. Smolyaninov, and Christopher C. Davis. "Surface plasmon polariton enhanced fluorescence from quantum dots on nanostructured metal surfaces." Nano letters 10, no. 3 (2010): 813-820.

[106] Lakowicz, Joseph R. "Radiative decay engineering 5: metal-enhanced fluorescence and plasmon emission." Analytical biochemistry 337, no. 2 (2005): 171-194.

[107] Sun, Greg, Jacob B. Khurgin, and C. C. Yang. "Impact of high-order surface plasmon modes of metal nanoparticles on enhancement of optical emission." Applied Physics Letters 95, no. 17 (2009): 171103.

[108] Xie, Fang, Jing S. Pang, Anthony Centeno, Mary P. Ryan, D. Jason Riley, and Neil M. Alford. "Nanoscale control of Ag nanostructures for plasmonic fluorescence enhancement of near-infrared dyes." Nano Research 6, no. 7 (2013): 496-510.

[109] Kannegulla, A., Y. Liu, Bo Wu, and L-J. Cheng. "Aluminum ultraviolet–visible plasmonic arrays for broadband and wavelength-selective enhancements of quantum dot emission." Applied Physics Letters 111, no. 8 (2017): 081106.

[110] Li, Ming, Scott K. Cushing, and Nianqiang Wu. "Plasmon-enhanced optical sensors: a review." Analyst 140, no. 2 (2015): 386-406.

[111] Kannegulla, Akash, and Li-Jing Cheng. "Metal assisted focused-ion beam nanopatterning." Nanotechnology 27, no. 36 (2016): 36LT01.

[112] Shahbazyan, Tigran V., and Vitaliy N. Pustovit. "Plasmonic dicke effect." Applied Physics A 103, no. 3 (2011): 755-758.

[113] Pustovit, Vitaliy N., and Tigran V. Shahbazyan. "Plasmon-mediated superradiance near metal nanostructures." Physical Review B 82, no. 7 (2010): 075429.

[114] Li, Jianwei Jeffery, Yizhuo Chu, Benjamin Yi-Hung Lee, and Xiaoliang Sunney Xie. "Enzymatic signal amplification of molecular beacons for sensitive DNA detection." Nucleic acids research 36, no. 6 (2008): e36.

[115] Yang, Zhenyu, Alyf Janmohamed, Xinzheng Lan, F. Pelayo García de Arquer, Oleksandr Voznyy, Emre Yassitepe, Gi-Hwan Kim et al. "Colloidal quantum dot photovoltaics enhanced by perovskite shelling." Nano letters 15, no. 11 (2015): 7539-7543.

[116] Yuan, Mingjian, Mengxia Liu, and Edward H. Sargent. "Colloidal quantum dot solids for solution-processed solar cells." Nature Energy 1, no. 3 (2016): 16016.

[117] Hildebrandt, Niko. "Biofunctional quantum dots: controlled conjugation for multiplexed biosensors." Acs Nano 5, no. 7 (2011): 5286-5290.

[118] Wang, Yucheng, Rui Hu, Guimiao Lin, Indrajit Roy, and Ken-Tye Yong. "Functionalized quantum dots for biosensing and bioimaging and concerns on toxicity." ACS applied materials & interfaces 5, no. 8 (2013): 2786-2799.

[119] Loo, Adeline Huiling, Zdenek Sofer, Daniel Bouša, Pavel Ulbrich, Alessandra Bonanni, and Martin Pumera. "Carboxylic carbon quantum dots as a fluorescent sensing platform for DNA detection." ACS applied materials & interfaces 8, no. 3 (2016): 1951-1957.

[120] Yang, Yixing, Ying Zheng, Weiran Cao, Alexandre Titov, Jake Hyvonen, Jesse R. Manders, Jiangeng Xue, Paul H. Holloway, and Lei Qian. "High-efficiency light-emitting devices based on quantum dots with tailored nanostructures." Nature Photonics 9, no. 4 (2015): nphoton-2015.

[121] Choi, Moon Kee, Jiwoong Yang, Kwanghun Kang, Dong Chan Kim, Changsoon Choi, Chaneui Park, Seok Joo Kim et al. "Wearable red–green–blue quantum dot light-emitting diode array using high-resolution intaglio transfer printing." Nature communications 6 (2015): 7149.

[122] Gu, Xuefeng, Teng Qiu, Wenjun Zhang, and Paul K. Chu. "Light-emitting diodes enhanced by localized surface plasmon resonance." Nanoscale research letters 6, no. 1 (2011): 199.

[123] Shen, Huaibin, Weiran Cao, Nathan T. Shewmon, Chenchen Yang, Lin Song Li, and Jiangeng Xue. "High-efficiency, low turn-on voltage blue-violet quantum-dot-based light-emitting diodes." Nano letters 15, no. 2 (2015): 1211-1216.

[124] Knight, Mark W., Nicholas S. King, Lifei Liu, Henry O. Everitt, Peter Nordlander, and Naomi J. Halas. "Aluminum for plasmonics." ACS nano 8, no. 1 (2013): 834-840.

[125] Larsson, Elin M., Christoph Langhammer, Igor Zorić, and Bengt Kasemo. "Nanoplasmonic probes of catalytic reactions." Science 326, no. 5956 (2009): 1091-1094.

[126] Chan, George H., Jing Zhao, George C. Schatz, and Richard P. Van Duyne. "Localized surface plasmon resonance spectroscopy of triangular aluminum nanoparticles." The Journal of Physical Chemistry C 112, no. 36 (2008): 13958-13963.

[127] Anger, Pascal, Palash Bharadwaj, and Lukas Novotny. "Enhancement and quenching of single-molecule fluorescence." Physical review letters 96, no. 11 (2006): 113002.

[128] Pompa, P. P., L. Martiradonna, A. Della Torre, F. Della Sala, L. Manna, M. De Vittorio, F. Calabi, R. Cingolani, and R. Rinaldi. "Metal-enhanced fluorescence of colloidal nanocrystals with nanoscale control." Nature nanotechnology 1, no. 2 (2006): 126.

[129] Belacel, Cherif, Benjamin Habert, Florian Bigourdan, François Marquier, J-P. Hugonin, S. Michaelis de Vasconcellos, Xavier Lafosse et al. "Controlling spontaneous emission with plasmonic optical patch antennas." Nano letters 13, no. 4 (2013): 1516-1521.

[130] Hwang, Ehren, Igor I. Smolyaninov, and Christopher C. Davis. "Surface plasmon polariton enhanced fluorescence from quantum dots on nanostructured metal surfaces." Nano letters 10, no. 3 (2010): 813-820.

[131] Wang, Zhijiang, Lina Wu, Jigang Zhou, Baozhong Shen, and Zhaohua Jiang. "Enhanced microwave absorption of Fe 3 O 4 nanocrystals after heterogeneously growing with ZnO nanoshell." RSC Advances 3, no. 10 (2013): 3309-3315.

[132] Shin, Jaeyoung, Klaus-R. Müller, and Han-Jeong Hwang. "Near-infrared spectroscopy (NIRS)-based eyes-closed brain-computer interface (BCI) using prefrontal cortex activation due to mental arithmetic." Scientific reports 6 (2016): 36203.

[133] Hoang, Thang B., Gleb M. Akselrod, Christos Argyropoulos, Jiani Huang, David R. Smith, and Maiken H. Mikkelsen. "Ultrafast spontaneous emission source using plasmonic nanoantennas." Nature communications 6 (2015): 7788.

[134] Hoang, Thang B., Gleb M. Akselrod, and Maiken H. Mikkelsen. "Ultrafast room-temperature single photon emission from quantum dots coupled to plasmonic nanocavities." Nano letters 16, no. 1 (2015): 270-275.

[135] Demory, Brandon, Adam Katcher, Tyler Hill, Chu-Hsiang Teng, Cheng Zhang, L. Jay Guo, Hui Deng, and P. C. Ku. "Improving the radiative efficiency of InGaN quantum dots via an open top cavity." ACS Photonics 4, no. 4 (2017): 795-799.

[136] Hofmann, Carrie E., F. Javier García de Abajo, and Harry A. Atwater. "Enhancing the radiative rate in III− V semiconductor plasmonic core− shell nanowire resonators." Nano letters 11, no. 2 (2011): 372-376.

[137] Pustovit, Vitaliy N., and Tigran V. Shahbazyan. "Plasmon-mediated superradiance near metal nanostructures." Physical Review B 82, no. 7 (2010): 075429.

[138] Pustovit, Vitaliy N., and Tigran V. Shahbazyan. "Resonance energy transfer near metal nanostructures mediated by surface plasmons." Physical Review B 83, no. 8 (2011): 085427.

[139] Drachev, Vladimir P., Viktor A. Podolskiy, and Alexander V. Kildishev. "Hyperbolic metamaterials: new physics behind a classical problem." Optics express 21, no. 12 (2013): 15048-15064.

[140] Shekhar, Prashant, Jonathan Atkinson, and Zubin Jacob. "Hyperbolic metamaterials: fundamentals and applications." Nano convergence 1, no. 1 (2014): 14.

[141] Poddubny, Alexander, Ivan Iorsh, Pavel Belov, and Yuri Kivshar. "Hyperbolic metamaterials." Nature Photonics 7, no. 12 (2013): 948.

[142] Wood, B., J. B. Pendry, and D. P. Tsai. "Directed subwavelength imaging using a layered metal-dielectric system." Physical Review B 74, no. 11 (2006): 115116.

[143] Iorsh, Ivan, Alexander Poddubny, Alexey Orlov, Pavel Belov, and Yuri S. Kivshar. "Spontaneous emission enhancement in metal–dielectric metamaterials." Physics Letters A 376, no. 3 (2012): 185-187.

[144] Jacob, Zubin, Igor I. Smolyaninov, and Evgenii E. Narimanov. "Broadband Purcell effect: Radiative decay engineering with metamaterials." Applied Physics Letters 100, no. 18 (2012): 181105.

[145] Kim, J., Vladimir P. Drachev, Z. Jacob, Gururaj V. Naik, Alexandra Boltasseva, Evgenii E. Narimanov, and Vladimir M. Shalaev. "Improving the radiative decay rate for dye molecules with hyperbolic metamaterials." Optics express 20, no. 7 (2012): 8100-8116.

[146] Krishnamoorthy, Harish NS, Zubin Jacob, Evgenii Narimanov, Ilona Kretzschmar, and Vinod M. Menon. "Topological transitions in metamaterials." Science 336, no. 6078 (2012): 205-209.

[147] Newman, Ward D., Cristian L. Cortes, and Zubin Jacob. "Enhanced and directional single-photon emission in hyperbolic metamaterials." JOSA B 30, no. 4 (2013): 766-775.

[148] Sreekanth, K. V., T. Biaglow, and G. Strangi. "Directional spontaneous emission enhancement in hyperbolic metamaterials." Journal of Applied Physics 114, no. 13 (2013): 134306.

[149] Ferrari, Lorenzo, Dylan Lu, Dominic Lepage, and Zhaowei Liu. "Enhanced spontaneous emission inside hyperbolic metamaterials." Optics Express 22, no. 4 (2014): 4301-4306.

[150] Shalaginov, Mikhail Y., Satoshi Ishii, Jingjing Liu, J. Liu, J. Irudayaraj, A. Lagutchev, A. V. Kildishev, and V. M. Shalaev. "Broadband enhancement of spontaneous emission from nitrogen-vacancy centers in nanodiamonds by hyperbolic metamaterials." Applied Physics Letters 102, no. 17 (2013): 173114.

[151] Lu, Dylan, Jimmy J. Kan, Eric E. Fullerton, and Zhaowei Liu. "Enhancing spontaneous emission rates of molecules using nanopatterned multilayer hyperbolic metamaterials." Nature nanotechnology 9, no. 1 (2014): 48.

[152] Zhukovsky, Sergei V., Omar Kidwai, and J. E. Sipe. "Physical nature of volume plasmon polaritons in hyperbolic metamaterials." Optics express 21, no. 12 (2013): 14982-14987.

[153] Li, Ling, Wei Wang, Ting S. Luk, Xiaodong Yang, and Jie Gao. "Enhanced quantum dot spontaneous emission with multilayer metamaterial nanostructures." ACS Photonics 4, no. 3 (2017): 501-508.

[154] Lu, Dylan, Haoliang Qian, Kangwei Wang, Hao Shen, Feifei Wei, Yunfeng Jiang, Eric E. Fullerton, Paul KL Yu, and Zhaowei Liu. "Nanostructuring Multilayer Hyperbolic Metamaterials for Ultrafast and Bright Green InGaN Quantum Wells." Advanced Materials 30, no. 15 (2018): 1706411.

[155] Galfsky, T., H. N. S. Krishnamoorthy, W. Newman, E. E. Narimanov, Z. Jacob, and V. M. Menon. "Active hyperbolic metamaterials: enhanced spontaneous emission and light extraction." Optica 2, no. 1 (2015): 62-65.

[156] Galfsky, Tal, Jie Gu, Evgenii E. Narimanov, and Vinod M. Menon. "Photonic hypercrystals for control of light–matter interactions." Proceedings of the National Academy of Sciences (2017): 201702683.

[157] Kannegulla, A., Y. Liu, Bo Wu, and L-J. Cheng. "Aluminum ultraviolet–visible plasmonic arrays for broadband and wavelength-selective enhancements of quantum dot emission." Applied Physics Letters 111, no. 8 (2017): 081106.

[158] Kannegulla, Akash, Ye Liu, Bo Wu, and Li-Jing Cheng. "Plasmonic Open-Ring Nanoarrays for Broadband Fluorescence Enhancement and Ultrasensitive DNA Detection." The Journal of Physical Chemistry C 122, no. 1 (2017): 770-776.

[159] Roy-Choudhury, Kaushik, and Stephen Hughes. "Spontaneous emission from a quantum dot in a structured photonic reservoir: phonon-mediated breakdown of Fermi's golden rule." Optica 2, no. 5 (2015): 434-437.

[160] Newman, Ward D., Cristian L. Cortes, and Zubin Jacob. "Enhanced and directional single-photon emission in hyperbolic metamaterials." JOSA B 30, no. 4 (2013): 766-775.

[161] Zhukovsky, Sergei V., Omar Kidwai, and J. E. Sipe. "Physical nature of volume plasmon polaritons in hyperbolic metamaterials." Optics express 21, no. 12 (2013): 14982-14987.

[162] Ferrari, Lorenzo, Joseph Stephen Thomas Smalley, Yeshaiahu Fainman, and Zhaowei Liu. "Hyperbolic metamaterials for dispersion-assisted directional light emission." Nanoscale 9, no. 26 (2017): 9034-9048.

[163] Zhu, Peifen. "Light extraction efficiency enhancement of top-emitting organic light-emitting diodes employing low-Q whispering gallery modes in spheres." Materials Research Express 2, no. 9 (2015): 096202.

[164] Zhu, Peifen, and Nelson Tansu. "Effect of packing density and packing geometry on light extraction of III-nitride light-emitting diodes with microsphere arrays." Photonics Research 3, no. 4 (2015): 184-191.

[165]Li, Xiao-Hang, Peifen Zhu, Guangyu Liu, Jing Zhang, Renbo Song, Yik-Khoon Ee, Pisist Kumnorkaew, James F. Gilchrist, and Nelson Tansu. "Light Extraction Efficiency Enhancement of III-Nitride Light-Emitting Diodes by Using 2-D Close-Packed TiO2 Microsphere Arrays." Journal of Display Technology 9, no. 5 (2013): 324-332.

[166] Wu, Chang-Yu, Tsai-Fu Wu, Jiun-Ren Tsai, Yaow-Ming Chen, and Chien-Chih Chen. "Multistring LED backlight driving system for LCD panels with color sequential display and area control." IEEE Transactions on industrial electronics 55, no. 10 (2008): 3791-3800.

[167] Yang, Zong-Zhen, Yi-Hua Liu, Po-Yen Chen, and Jia-Wei Huang. "Sequential-color voltage-adaptable RGB-LED backlight driving system with local dimming control for LCD panels." In Power Electronics and Drive Systems, 2009. PEDS 2009. International Conference on, pp. 1542-1546. IEEE, 2009.

[168] Cho, Daeyoun, Won-Sik Oh, and Gun Woo Moon. "A novel adaptive dimming LED backlight system with current compensated XY channel drivers for LCD TVs." Journal of Display Technology 7, no. 1 (2011): 29-35.

[169] Lo, Yu-Kang, Kuan-Hung Wu, Kai-Jun Pai, and Huang-Jen Chiu. "Design and implementation of RGB LED drivers for LCD backlight modules." IEEE Transactions on Industrial Electronics 56, no. 12 (2009): 4862-4871.

[170] Cho, Hyunsuk, and Oh-Kyong Kwon. "A local dimming algorithm for low power LCD TVs using edge-type LED backlight." IEEE Transactions on Consumer Electronics 56, no. 4 (2010).

[171] Chiu, Huang-Jen, Yu-Kang Lo, Ting-Peng Lee, Shann-Chyi Mou, and Hsiu-Ming Huang. "Design of an RGB LED backlight circuit for liquid crystal display panels." IEEE Transactions on Industrial electronics 56, no. 7 (2009): 2793-2795.

[172] Komine, Toshihiko, and Masao Nakagawa. "Fundamental analysis for visible-light communication system using LED lights." IEEE transactions on Consumer Electronics 50, no. 1 (2004): 100-107.

[173] Wang, Yuanquan, Yiguang Wang, Nan Chi, Jianjun Yu, and Huiliang Shang. "Demonstration of 575-Mb/s downlink and 225-Mb/s uplink bi-directional SCM-WDM visible light communication using RGB LED and phosphor-based LED." Optics express 21, no. 1 (2013): 1203-1208.

[174] Wang, Yiguang, Nan Chi, Yuanquan Wang, Li Tao, and Jianyang Shi. "Network architecture of a high-speed visible light communication local area network." IEEE Photonics Technology Letters 27, no. 2 (2015): 197-200.

[175] Vučić, Jelena, Christoph Kottke, Stefan Nerreter, Kai Habel, Andreas Büttner, Klaus-Dieter Langer, and Joachim W. Walewski. "230 Mbit/s via a wireless visible-light link based on OOK modulation of phosphorescent white LEDs." In Optical Fiber Communication (OFC), collocated National Fiber Optic Engineers Conference, 2010 Conference on (OFC/NFOEC), pp. 1-3. IEEE, 2010.

[176] Chow, C. W., C. H. Yeh, Y. F. Liu, and Y. Liu. "Improved modulation speed of LED visible light communication system integrated to main electricity network." Electronics letters 47, no. 15 (2011): 867-868.

[177] Yeh, C. H., Y. F. Liu, C. W. Chow, Y. Liu, P. Y. Huang, and H. K. Tsang. "Investigation of 4-ASK modulation with digital filtering to increase 20 times of direct modulation speed of white-light LED visible light communication system." Optics Express 20, no. 15 (2012): 16218-16223.

[178] Wu, Fang-Ming, Chun-Ting Lin, Chia-Chien Wei, Cheng-Wei Chen, Zhen-Yu Chen, and Kurt Huang. "3.22-Gb/s WDM visible light communication of a single RGB

LED employing carrier-less amplitude and phase modulation." In Optical Fiber Communication Conference, pp. OTh1G-4. Optical Society of America, 2013.

[179] Le Minh, Hoa, Dominic O'Brien, Grahame Faulkner, Lubin Zeng, Kyungwoo Lee, Daekwang Jung, YunJe Oh, and Eun Tae Won. "100-Mb/s NRZ visible light communications using a postequalized white LED." IEEE Photonics Technology Letters 21, no. 15 (2009): 1063-1065.

[180] Lin, Huang-Yu, Chin-Wei Sher, Dan-Hua Hsieh, Xin-Yin Chen, Huang-Ming Philip Chen, Teng-Ming Chen, Kei-May Lau, Chyong-Hua Chen, Chien-Chung Lin, and Hao-Chung Kuo. "Optical cross-talk reduction in a quantum-dot-based full-color micro-light-emitting-diode display by a lithographic-fabricated photoresist mold." Photonics Research 5, no. 5 (2017): 411-416.

[181] Chen, Guan-Syun, Bo-Yu Wei, Ching-Ting Lee, and Hsin-Ying Lee. "Monolithic Red/Green/Blue Micro-LEDs With HBR and DBR Structures." IEEE Photonics Technology Letters 30, no. 3 (2018): 262-265.

[182] Zhu, Jinyang, Xue Bai, Jialin Bai, Gencai Pan, Yongsheng Zhu, Yue Zhai, He Shao et al. "Emitting color tunable carbon dots by adjusting solvent towards light-emitting devices." Nanotechnology 29, no. 8 (2018): 085705.

[183] Agnihotri, Shekhar, Soumyo Mukherji, and Suparna Mukherji. "Size-controlled silver nanoparticles synthesized over the range 5–100 nm using the same protocol and their antibacterial efficacy." Rsc Advances 4, no. 8 (2014): 3974-3983.